TUDelft

Delft University of Technology

Electrochemically induced precipitation for contaminant removal from wastewaters streams
Electrocoagulation and electrochemical phosphate recovery

Yasadi, K.

Citation (APA)
Yasadi, K. (2024). *Electrochemically induced precipitation for contaminant removal from wastewaters streams: Electrocoagulation and electrochemical phosphate recovery*. [D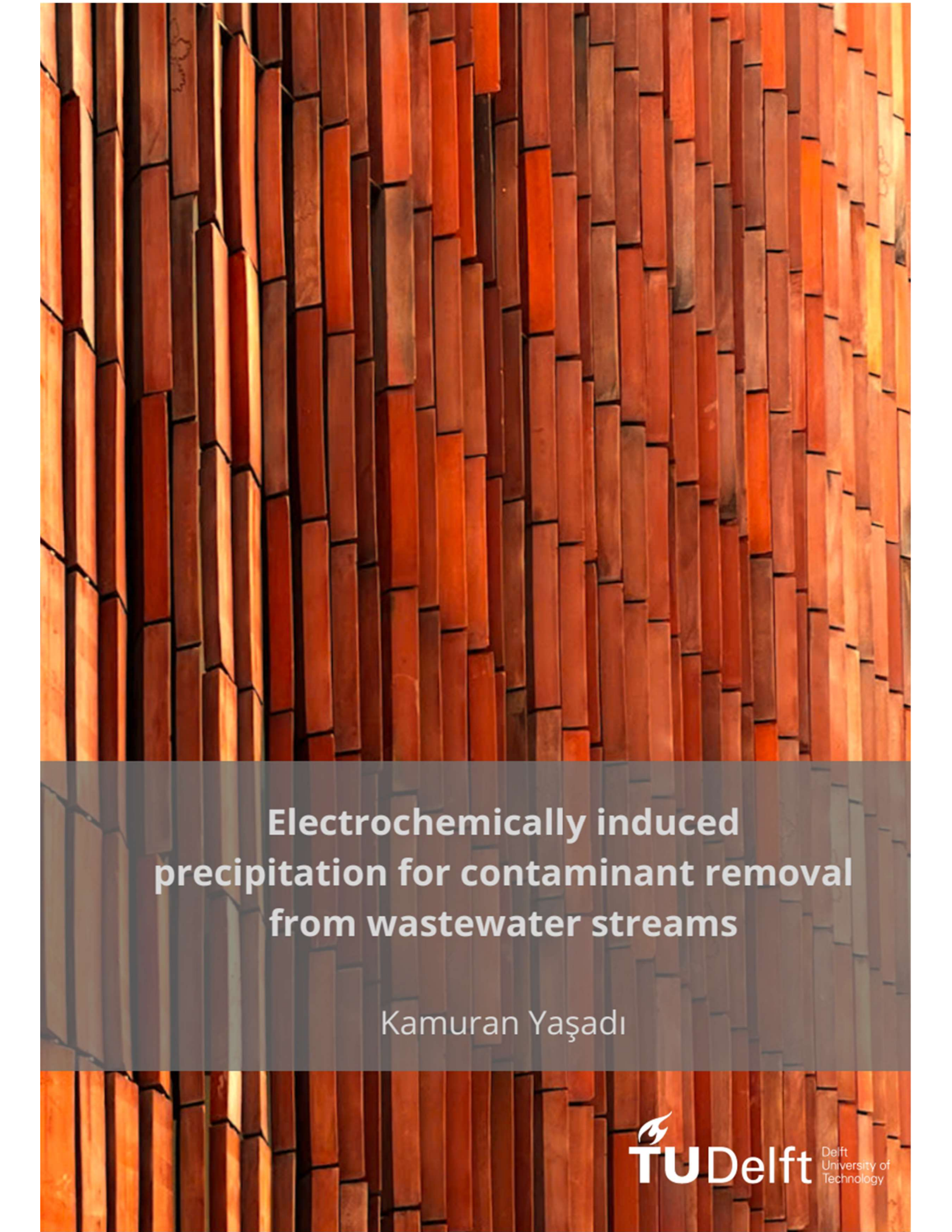issertation (TU Delft), Delft University of Technology]. https://doi.org/10.4233/uuid:f1449bc8-dceb-4240-a7c8-6382f11910c1

Important note
To cite this publication, please use the final published version (if applicable).
Please check the document version above.

Electrochemically induced precipitation for contaminant removal from wastewater streams

Kamuran Yaşadı

TUDelft
Delft University of Technology

Electrochemically induced precipitation for contaminant removal from wastewater streams

Proefschrift

ter verkrijging van de graad van doctor

aan de Technische Universiteit Delft

op gezag van de Rector Magnificus, Prof. dr. ir. T.H.J.J. van der Hagen,

voorzitter van het College van Promoties,

in het openbaar te verdedigen op

maandag 18 november 2024 om 12:30

door

Kamuran YAŞADI

Master of Science in Earth Sciences, Universiteit Utrecht, Nederland

geboren te Eindhoven, Nederland

Dit proefschrift is goedgekeurd door promotor(en)

Samenstelling promotiecommissie bestaat uit

Rector Magnificus	Voorzitter
Prof. dr. G.J. Witkamp	Technische Universiteit Delft, Promotor
Prof. dr. E.H. Brück	Technische Universiteit Delft, Promotor

Onafhankelijke leden:

Dr. ir. S.G.J. Heijman	Technische Universiteit Delft
Prof. dr. F.M. Mulder	Technische Universiteit Delft
Prof. dr. ir. H.V.M Hamelers	Wageningen University and Research
Dr. P. Suresh Kumar	Plaksha Universiteit, India
Prof. dr. P. Wilfert	Technische Universiteit van Lübeck, Duitsland
Prof. dr. P. Dorenbos	Technische Universiteit Delft, reservelid

To my family, daughter Mira, wife Małgorzata, parents Ilyas and Mürselin and brother Yasin

List of abbreviations

ATR-FTIR	Attenuated Total Reflectance Fourier Transform InfraRed
A_s (m^2/g)	Specific surface area, square meters of surface area per gram
ACC	Amorphous calcium carbonate
ACP	Amorphous calcium phosphate
CO_3	Carbonate
$E_{h,elec}$	Electrolyte potential
$E_{h,surf}$	Electric surface potential
EPR	Electrochemical PO_4 recovery
EXAFS	Extended X-ray Absorption Fine Structure
Fe-EC	Iron (Fe) Electrocoagulation
$\equiv$Fe-OH	Surface active hydroxyl groups
Fe(II)	Aqueous ferrous iron forms: Fe^{2+}, $FeOH^+$, $Fe(OH)_2$, $Fe(OH)_3^-$
Fe(III)	Aqueous ferric iron forms: Fe^{3+}, $FeOH^{2+}$, $Fe(OH)_2^+$, $Fe(OH)_4^-$
Fe(III)$_{Labile}$	Labile Fe(III) fraction that forms through electron transfer between Fe(II)-ions and ferrihydrite
Fh	Ferrihydrite
G	Goethite
J	Current density, A/m^2
L	Lepidocrocite
Magn	Magnetite
Magh	Maghemite
MBR	Membrane Bioreactor
NF	Nano-filtration
PO_4	Phosphate
WWTP	Waste water treatment plants
XPS	X-Ray Photoelectron Spectroscopy
XRD	X-ray diffraction

Table of contents

1

Introduction

1.1. Water scarcity, climate change and energy transition

In an era of ongoing energy transition, the conversion of wind and solar power into electric power will play a larger role in generating renewable energy. As a result, conventional industrial and domestic water treatments will need to undergo an electrification process, where existing technologies are expected to be replaced by water treatment technologies that are operated and governed by electric sources. The use of electrochemical water treatments has attracted significant attention as potential technologies for removing contaminants or reclaiming valuable components from wastewater. Special focus is placed on technologies that have a minimal impact on the composition of wastewater, making it easier to reclaim and reuse these bodies of water for other purposes, such as irrigation in the face of climate change, where water scarcity has become a serious problem. Additionally, the slight alterations to the composition of wastewater allow for the release of wastewater with lower levels of contaminants and salt, thus having a reduced impact on the surrounding environment, such as minimizing salt stress and eutrophication (e.g., phosphate being a major accelerator of eutrophication). This thesis investigates two different electrochemical water treatment technologies for their application in waste and process water treatment, aligning with the "electrification of water treatment" framework and aiming to treat wastewater without increasing its salinity. The two water treatment technologies under investigation are *iron electrocoagulation (Fe-EC)* and *electrochemical* phosphate *recovery*.

1.2. Iron electrocoagulation for the removal of heavy metals and toxic anions

Iron oxyhydroxides are widely used materials for removing trace organic and inorganic contaminants from wastewater streams. Their amphoteric nature and nearly pH-neutral surface charge allow them to effectively bind heavy metal cations such as Cu(II), Cd(II), Pb(II), Zn(II), hazardous anions like As(III,V) and Se(IV,VI), and certain organic pollutants like chloramine. *Iron electrocoagulation* (Fe-EC) is a process that produces iron oxyhydroxides by oxidizing electrolytic steel (>99% Fe(0)) using applied currents (direct or alternating). This process controls the dosage of Fe(II) and Fe(III) by using oxygenated electrolytes to enable the oxidation of Fe(II) (rather than Fe(III) which precipitates instantly). Fe-EC is considered an alternative to conventional chemical coagulants such as $FeCl_2$ and $FeSO_4$. Table 1.1 provides

an overview of the main advantages and disadvantages of Fe-EC compared to chemical coagulation methods.

Table 1.1. *The (dis)advantages of chemical coagulation vs. electro-coagulation (Moussa et al.(2016), Hakizimana et al. (2017), Boinpaly et al. (2023)*

	CHEMICAL COAGULATION	ELECTRO-COAGULATION
ADVANTAGES	- Ease of operation - Mature technology - Easily accessible chemicals - Low costs	- Compact cell design - No salinity increase - Small storage facilities - No pumping doses required - Low costs operations - Allows flotation and phase separation of sludge (by H_2-gas formation) - Operational by coupling to renewable energy sources (Solar and Wind)
DISADVANTAGE	- Rise of salinity by salt dissolution - Co-dosing of bases - Large storage facilities for chemicals - Additional pumping control systems required. - - Leads to higher Fe/pollutant removal than Fe-EC. - Leads to higher Fe/pollutant removal than Fe-EC (reasons not fully understood)	- Electric energy input, especially high electric energy requirement for less conductive electrolytes. - Passivation and scaling, followed by deterioration of the Fe-EC process during continuous operations. - Electric energy input for aeration techniques increasing the overall efficiency

The main advantages of Fe-EC are that it greatly minimizes the increase in salinity during water treatment, thereby eliminating the need for additional technologies like ion exchange and reverse osmosis to treat the treated wastewaters. This means that Fe-EC treatment allows for the reclamation of wastewater bodies and opens up new possibilities for reusing the water in secondary applications such as irrigation or other processes. Additionally, the Fe-EC technology has distinct properties such as: 1) compact cells that are small and have

a low volume, 2) the additional benefit of flotation effects that separate the sludge phase using H_2-gas bubbles (sometimes referred to as electro-flotation), 3) significant reduction in pumping losses due to Fe-salts solution/slurry being pumped into the wastewater bodies, and 4) easy construction and operation of Fe-EC cell stacks.

1.3. Understanding the Fe-EC process in relation to rust composition.

In Fe-EC process operations, the Fe(0) first oxidizes to Fe(II) ions (Fe^{2+}, $Fe(OH)^+$, $Fe(OH)_2$, $Fe(OH)_3^-$), which dissolve in the adjacent electrolyte (Lakshmanan et al. (2009)). These ions are then further oxidized to Fe(III) (composed of Fe^{3+}, $Fe(OH)^{2+}$, and $Fe(OH)_4^-$). However, Fe(III) is barely soluble and tends to precipitate within the pH range of 4 – 10. On the other hand, Fe(II) is more soluble and precipitates as $Fe(OH)_2$ or a mixture of Fe(II)-Fe(III) oxyhydroxide beyond a pH of 7. For example, at pH 8, 1 mM $[Fe(II)]_T$ will precipitate (Morgan and Lahav (2007)).

To prevent the loss of Fe due to the accumulation of Fe(II), and since the removal of contaminants in most wastewaters with a pH between 4-10 is typically achieved using ferric oxyhydroxides or a mixture of ferrous-ferric oxyhydroxides, the dissolved Fe(II) is partially or fully oxidized in the electrolyte during the electrolytic dissolution of Fe(0) corrosion. The most readily available and easily-supplied oxidant in wastewater treatment is unquestionably $O_{2(aq)}$, as it readily dissolves in the wastewater electrolyte when the water is exposed to air. If the dissolution of $O_{2(aq)}$ is insufficient to cope with the Fe(II) generation rates, additional $O_{2(aq)}$ can be supplied to the electrolyte by aeration or electrolyte mixing (Mao et al. (2023), Gil et al. (2022), Nidheesh and Gökkuş (2023)).

In aerated Fe-EC cells, the following electrolyte and electrode reactions take place:

Anode reaction:

$$Fe(0) \rightarrow Fe(II) + 2e^- \qquad E^0_{SHE}(Fe^0/Fe^{2+}) = -0.44V \qquad \text{eq. 1.1}$$

The electron released from eq. 1.1 leads to the production of H_2 at the cathode surface:

$$2H^+ + 2e^- \rightarrow H_2 \qquad E^0_{SHE}(H^+/H_2) = 0.00V \qquad \text{eq. 1.2}$$
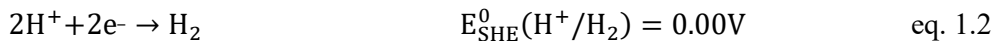
Electrolyte reaction:
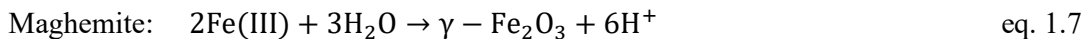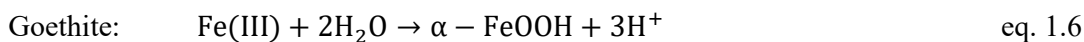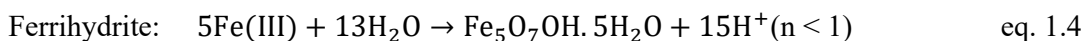
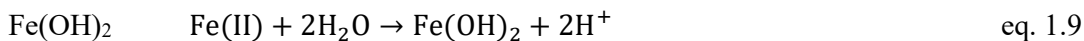$$4Fe(II) + O_2 + 4H^+ \rightarrow 4Fe(III) \qquad\qquad \text{eq. 1.3}$$

Iron oxyhydroxides (ferric and ferrous) are found in various forms with varying adsorption capacities for contaminants such as Pb(II), Se(IV, VI), and As(III, V). They also have the ability to incorporate heavy metals like Zn(II), Pb(II), and Cu(II) into their structure. Iron oxyhydroxides can be utilized for the reductive removal of hazardous anions such as As(V) and Se(VI) (Van Genuchten et al. (2012), Bae et al. (2022)).
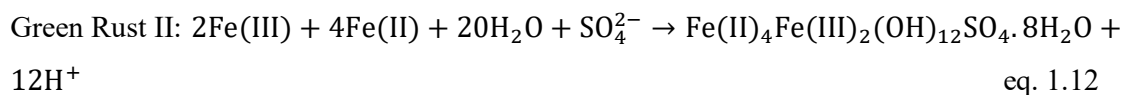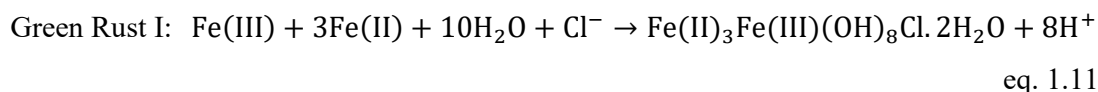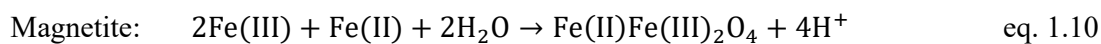
In applications of Fe-EC for wastewater treatment, it is preferable to remove contaminants using the least amount of Fe(0)-electrode, in order to minimize electric energy consumption and sludge production (thereby reducing the amount of sludge sent to landfill areas). However, there have been few studies characterizing the rust phases that form during the corrosion of Fe(0) (either electrically or atmospherically) using techniques such as XRD, XRF, EXAFS, Raman, ATR-FTIR, and Mössbauer spectroscopy (Misawa et al. (1974), Music et al. (1993), Mukesh and Panday (2001), Van Genuchten (2014, 2018)). Generally, the characterization of the formed phases shows the presence of ferrihydrite (2-line: $Fe_{10}O_{14}(OH)_2.nH_2O$ (n < 1) and 6-line: $Fe_{1.55}O_{1.66}OH_{1.34}$), lepidocrocite ($\gamma$-FeOOH), magnetite ($Fe_3O_4$), maghemite ($\gamma$-$Fe_2O_3$), hematite ($\alpha$-$Fe_2O_3$), goethite ($\alpha$-FeOOH), as well as green rusts (GRI (Cl-GR)) and GRII ((SO_4-GR) type) (Refait et al. (1998, 2006)).

The formation of these phases is facilitated by the following reactions, expressed per generated Fe(III):

Ferrihydrite: $\quad 5Fe(III) + 13H_2O \rightarrow Fe_5O_7OH.\,5H_2O + 15H^+ (n < 1)$ eq. 1.4

Lepidocrocite: $Fe(III) + 2H_2O \rightarrow \gamma - FeOOH + 3H^+$ eq. 1.5

Goethite: $\qquad Fe(III) + 2H_2O \rightarrow \alpha - FeOOH + 3H^+$ eq. 1.6

Maghemite: $\quad 2Fe(III) + 3H_2O \rightarrow \gamma - Fe_2O_3 + 6H^+$ eq. 1.7

Hematite: $\qquad 2Fe(III) + 3H_2O \rightarrow \alpha - Fe_2O_3 + 6H^+$ eq. 1.8
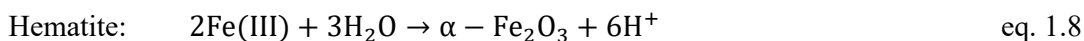
Fe(II) can solely precipitate in the form of $Fe(OH)_2$. If Fe(II) is partially oxidized, mixed Fe(II)-Fe(III) phases such as magnetite and green rust can evolve through co-precipitation of Fe(II) and Fe(III). Magnetite and green rust (types I and II) are formed according to the following reactions:

$Fe(OH)_2 \qquad Fe(II) + 2H_2O \rightarrow Fe(OH)_2 + 2H^+$ eq. 1.9

Magnetite: $\quad 2Fe(III) + Fe(II) + 2H_2O \rightarrow Fe(II)Fe(III)_2O_4 + 4H^+$ $\qquad$ eq. 1.10

Green Rust I: $\quad Fe(III) + 3Fe(II) + 10H_2O + Cl^- \rightarrow Fe(II)_3Fe(III)(OH)_8Cl.\,2H_2O + 8H^+$

$\qquad\qquad\qquad\qquad\qquad\qquad\qquad\qquad\qquad\qquad\qquad\qquad\qquad\qquad$ eq. 1.11

Green Rust II: $2Fe(III) + 4Fe(II) + 20H_2O + SO_4^{2-} \rightarrow Fe(II)_4Fe(III)_2(OH)_{12}SO_4.\,8H_2O +$

$12H^+$ $\qquad\qquad\qquad\qquad\qquad\qquad\qquad\qquad\qquad\qquad\qquad\qquad\qquad\qquad\qquad$ eq. 1.12

A major advantage of Fe-EC treatment is the neutral nature of the overall reaction. Compared to the production of $+3H^+$ by Fe(III)-oxyhydroxides and the consumption of $-3H^+$ through the reaction with $O_{2(aq)}$ and H_2 evolution, which greatly reduces the need for adding bases. This is in contrast to the treatment with ferrous and ferric salts, where co-dosing of $Ca(OH)_2$ or NaOH is required to maintain the pH and prevent the formation of iron oxyhydroxide precipitates.

Of the iron oxyhydroxides that have been identified and characterized, the 2-line ferrihydrite undoubtedly exhibits a high concentration of active $\equiv$Fe-OH on its surface and interstructural domains. It also has the largest specific surface area, ranging from 250 m^2/g (aged) to 1100 m^2/g (freshly generated) (Hiemstra et al., 2019). For example, ferrihydrite has a scavenging capacity for PO_4 that is 6-18 times higher than the lepidocrocite phase, with a ratio of 0.16 P/Fe(III) per produced Fe(III), compared to 0.009-0.027 P/Fe(III) for lepidocrocite (Kraal et al. (2019)). Ferrihydrite is also known to include certain heavy metals, such as Zn(II), with a molar ratio of Zn(II)/(Zn(II)+Fe(III)) up to 20%, and the conditions necessary for the formation of these mixed phases are demonstrated in Waychunas et al. (2003).

Goethite and lepidocrocite are crystalline phases with much lower adsorption capacity and ability to include Zn(II) and PO_4 in their structures compared to ferrihydrite. Therefore, the production of ferrihydrite at the expense of crystalline lepidocrocite and goethite requires relatively lower consumption of Fe(0)-electrode and lower electric energy consumption. Magnetite is commonly observed under low oxygen levels and possesses a spinel structure that can incorporate foreign cations like Zn(II), Cu(II), and Cr(III). Green rusts are a class of layered double hydroxides that can accommodate cations and anions between their Fe(II,III)-sheets, including Zn(II), Mg(II), Cu(II), as well as anions such as Cl^-, SO_4, CO_3, SeO_4, SeO_3, and CrO_4.

1.4. Fe-EC cell build-up designs and its impact on iron oxyhydroxide formation

The passivation of the electrode surfaces due to the inhibiting effect of Fe(0) corrosion by iron oxyhydroxide precipitation is one of the main challenges in maintaining the continuous

operation of the Fe-EC process. The anode is particularly susceptible to passivation, as the local increase in [Fe(III)] during Fe-EC process operations, or the re-precipitation of Fe(III) on the electrode surface after being formed in the electrolyte, can cause surface precipitation of poorly soluble Fe(III) ions (Amaral and Muller, (1999)). At the cathode, the local high pH created by the production of OH^- ions may increase the surface precipitates of iron oxyhydroxides (eq. 1.2). There are a few examples of removing the precipitate during the intermediate start-stop process and enabling the continuous operation of Fe-EC, such as occasionally reversing the electrodes (Timmes et al., (2010)), alternating the current to reduce and dissolve Fe(III) as Fe(II) (Yang et al., (2015)), or using sonication (Maha Lakshmi and Sivashanmugam, (2013)). However, the application of these surface cleaning methods is limited by the frequency of the passivation event. Therefore, it is preferred to strongly minimize passivation during the period of total dissolution and consumption of the Fe(0) anode. One potential way to achieve this is to operate the Fe-EC cells at low current density (< 1 A/m^2) to maintain low anodic cell potentials ($E_{Anode} < +0.77$ V) and only form Fe^{2+} at the anode (Lakshmaman et al., (2009); Martin-Dominquez et al., (2008); Muller et al., (2019)). In this case, a large electrode surface area can be applied to compensate for the required Fe(II) dosage in the wastewater stream. For instance, two long-term feasibility studies (> 1 year) of Fe-EC application at low current densities (< 1 A/m^2) have demonstrated the continuous removal of PO_4 (Mishima et al., 2018) and the simultaneous removal of Zn(II), Mn(II), and Cd(II) from smelting wastewater (Xu et al., (2018)). It's important to consider that these Fe-EC applications are carried out in wastewaters that contain significant amounts of salts, which provide good conductivity and help reduce energy losses in the Fe-EC cells (ion mass transport, polarization, and ohmic loss). When operating Fe-EC in low-conductivity wastewaters, such as domestic wastewaters, cell voltages as high as 20-30 V can be reached (Bae et al. (2022); Martinez-Villafane et al. (2022)), which can lead to simultaneous formation of Fe(II), Fe(III), and O_2 at irregular amounts, resulting in faster passivation of the electrode surface. Additionally, the co-formation of O_2 and H_2 in Fe-EC can create unsafe explosive conditions. High cell losses generally lead to higher power consumption for treating a certain volume of wastewater (Martinez-Villafane et al. (2022)). Although simple salts like NaCl or Na_2SO_4 can be added to these effluents to increase ion conductivity, this is usually not desired as it necessitates a post-desalination step in wastewater treatment to avoid environmental stress from discharging salty water streams. Therefore, special attention is given to designing Fe-EC cells to minimize electrochemical losses in cells for low-conductivity electrolytes. A common design used in Fe-EC applications is to stack several large surface electrodes parallel to each other at the closest

7

possible distance (< 1 cm) to reduce ohmic losses (Mollah et al. (2004); Rodriguez-Rosales (2022); Martinez-Villafane et al. (2022)). The product formed in these adjusted cell designs greatly minimizes passivation and the simultaneous co-formation of Fe(III) and O_2 alongside the already forming Fe(II). However, a disadvantage of such designs is that they can interfere with the electrochemical and chemical reactions depicted in eq. 1.1-1.12 due to additional reactions occurring at the electrode surface (Moreno et al. (2007)). These potential reactions include 1) direct reduction of Fe(III), 2) deposition of iron oxyhydroxide on the surface and subsequent passivation, and 3) local increase in pH due to excessive production of OH- ions at higher current densities. In particular, the combination of local high pH with Fe(II) has a strong influence on the transformation of ferrihydrite and lepidocrocite to goethite. Apart from studying the formation of ferrihydrite by the Fe-EC process under varying process conditions, this thesis also focuses on understanding the role of local high pH in relation to the presence of Fe(II) in the production of lepidocrocite.

The study first examines the formation of ferrihydrite under a constantly operating low current-density Fe-EC process, studying the effect of the main operating oxygenation parameter. It then investigates the role of common anions, CO_3 and PO_4, in the formation of ferrihydrite. Finally, it explores the impact of local high pH in combination with the presence of Fe(II) on the transformation of lepidocrocite. The study uncovers a unique, previously unknown transformation mechanism in this regard.

1.5. Electrochemical PO_4 recovery; application to membrane bioreactors

1.5.1. The urge of PO_4 recovery from waste.

PO_4 is an essential substance for life and is involved in numerous metabolic processes in living organisms, such as bone formation and energy transfer. However, the excessive use of PO_4 fertilizers in activities like food production has led to a significant decline in the availability of phosphorus rock. There is still a basic discussion on whether PO_4 reserves are depleting and if they can be recovered through currently economically viable technologies (Scholtz and Steiner (2022)).

Furthermore, years of improper management of P-flows, particularly from agricultural soils, have caused devastating ecological issues like eutrophication in various ecosystems worldwide. This phenomenon has been observed in many lakes, rivers, and estuaries across the

globe (Suresh et al., 2023). As a result, there have been widespread water crises, severely impacting economies and societies (WWAP, UNESCO (2017)).

These events can be largely prevented by improving the management of P-flows throughout ecosystems. One critical approach to achieving this is by increasing the recycling of PO_4.
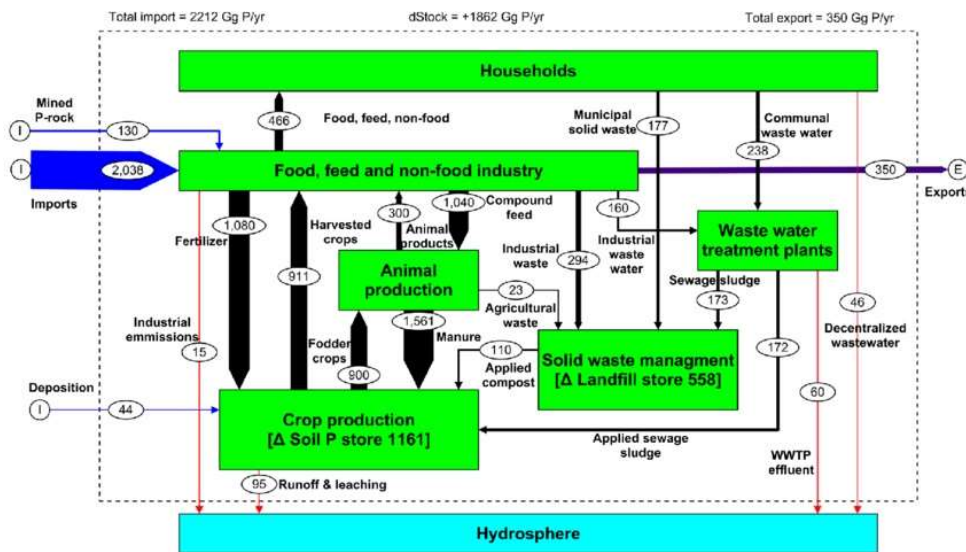

Fig. 1.1. *Phosphorus-flow and balance in EU-countries (Van Dijk et al. (2016)).*

When considering the most recent phosphorus balance for EU countries as illustrated in Figure 1.1, the major source of PO_4, accounting for around 80%, comes from waste produced by households, the food and feed industry, and animals (mostly livestock). This waste is treated at wastewater treatment plants (WWTPs), which are therefore the most potential sites for PO_4 recovery. Specifically focusing on Dutch WWTPs, PO_4 is treated at different stages of the anaerobic and aerobic sewage water treatment. It is common practice to use specially cultivated microorganisms to convert ortho-PO_4 into poly-PO_4 compounds and store them in their cells. After filtration and sedimentation, most P-components end up in sludge, which can be digested to produce biogas like methane. During this digestion, ammonium is produced and part of the poly-PO_4 is converted back to PO_4, which is then released in concentrated form in the so-called slipstream (STOWA, (2017)).

Membrane bioreactors (MBR) have received significant attention in the secondary treatment of nitrogen and phosphorus removal from wastewater treatment plants (Al-Ahseh et

al. (2021)). The membrane allows water and salts to permeate while rejecting particular (granular) organic matter. By retaining this particular organic matter in the MBR, high oxidation rates of the activated granular sludge are achieved, including a high conversion rate of organic nitrogen to N_2. MBRs are therefore suitable for compact and space-saving reactors, which also reduce the retention times of the sedimentation process compared to the large clarifiers used in conventional WWTPs. The permeate of municipal wastewater treated with MBR systems (MBR-permeate) is typically rich in calcium, magnesium, sodium, chloride, PO_4, sulfate, and humic acid and cannot be simply discharged into the environment due to potential eutrophication effects on the surrounding ecosystems. By implementing nanofiltration (NF) on the MBR-permeate to reject these salts and produce a salt-enriched concentrated effluent, a high-quality permeate water can be obtained for potential use in irrigation (with low salt levels) or in cooling towers (Kappel et al. (2014); Arola et al. (2021)).

One potential way to eliminate the concentrated effluent is to recirculate it in the preceding MBR at a certain ratio (e.g., 1:10) with the incoming wastewater influent. The resulting increase in salt concentration and supersaturation with respect to calcium phosphate/carbonate (PO_4/CO_3) enables the precipitation of these phases in the MBR tank, which then undergo sedimentation after large agglomerates are formed. These phases are then collected with the unreacted portion of the activated sludge. This concept was tested in Kappel et al. (2014) and was proven to be feasible in a 1-year trial of continuous recirculation, without any decline in biological activity of the MBR and maintaining consistent N-removal rates throughout the year. However, there was the issue of increased fouling of membranes due to surface precipitation of calcium phosphate/carbonate (CO_3/PO_4). This effect is largely caused by the higher prevailing supersaturation resulting from the recirculation of the NF-permeate and the enrichment of Ca^{2+}, PO_4, and CO_3 concentrations. The fouling results in increased feed pressures for the permeation of the MBR medium, leading to higher energy pumping costs, and requiring occasional cleaning of the membrane surfaces.

In this study, we propose an electrochemical method based on water electrolysis to recover calcium phosphate from the concentrated stream that is rejected from the combined treatment of MBR and NF. The electrochemical design includes a cation exchange membrane (CEM) electrolysis cell to control the pH in the anode and cathode compartments through water electrolysis. The pH of the concentrated NF solution is increased in the cathode compartment to induce the precipitation of calcium phosphate/carbonate (CO_3/PO_4). The functionality and future potential of this concept have been described in Chapter 5.

1.6. Objectives and outline of this thesis

The aim of this research is dedicated to bringing electro-coagulation (Fe-EC) and electrochemical PO_4 recovery (EPR) to a more practical situation, bridging the fundamental work of these processes and the sustainable application of both technologies to waste and process water treatment. In this thesis, particular emphasis is placed on first exploring the formation of ferrihydrite under controlled and continuous Fe-EC operating conditions.

Chapter 2 describes the relationship between ferrihydrite production and levels of Fe(II) during the Fe-EC process. Higher oxidation rates of Fe(II) were studied through aeration and hydrogen peroxide, as well as the addition of seeds to increase the productivity of ferrihydrite by preventing its transformation.

Chapter 3 illustrates the primary functions of CO_3- and PO_4- ions in the formation of ferrihydrite, specifically in the context of the Fe(II)-catalyzed transformation of ferrihydrite. The influence of these anions on ferrihydrite formation was investigated with regard to the following topics.

1) Competitive surface adsorption of these anions onto forming ferrihydrite by Fe(II),
2) The competitive precipitation of Fe(II)- and Fe(III)- as separate $FeCO_3.xH_2O$ and $Fe_2(PO_4).xH_2O$,
3) The surface potential effects on the competitive formation of lepidocrocite versus goethite from the Fe(II)-catalyzed recrystallization of ferrihydrite.
4) The formation and the aqueous complexation of these anions with Fe(II)- and Fe(III), and their impact on the Fe(II)-catalyzed recrystallization of forming ferrihydrite.

Chapter 4 demonstrates the potential impact of high alkaline conditions (1M NaOH) near the cathode surface and the presence of Fe(II) near this cathode surface on the stability and productivity of the lepidocrocite phase. This chapter aimed to study the catalyzed recrystallization of lepidocrocite in the presence of Fe(II) combined with high alkaline conditions (1M NaOH).

Chapter 5 presents the initial feasibility study on the application of water membrane electrolysis systems for the recovery of calcium PO$_4$ from the NF concentrate of MBR. (published under DOI 10.1016/j.seppur.2013.10.022)

References.

Al-Asheh S., Bagheri M., Aidan A., *Case Studies in Chemical and Environmental Engineering*, **2021**, 4 100109

Amaral S.T.; I. L. Muller, *Corrosion Science* **1999,** 41, (4), 747-758.

Arola K., Mänttäri M., Kallioinen M. *Sep. and Purif. Tech*., **2021**, 256, 117255

Bae Y. Nyssa M. Crompton N.M., Neha Sharma N., Yuan Y. *Water Research*, **2022**, 213:118159

Boinpally S, Kolla A, Kainthola J, Kodali R., Vemuri J. *Water Cycle*, **2023**, 4, 26–36

Gil J.L.; Van den Brink P.; De Moel P., Van der Steen P., Crossmark R, *Water Sci Technol,* **2022**, 86 (10), 2555–2569.

Deslouis C., Frateur I.; Maurin G., Tribollet B., *J. App. Electrochemistry*, **1997**, 27, 482-492.

Deligianni H., Romankiw L.T., IBM. J*. Res. Developt*, **1993**, 37 (2), 85-95

Hakizimana J.N., Gourich B., Chafi M., Stiriba Y., Vial C., Drogui P., Naja J. *Desalination*, **2017**, 404, 1-21

Hiemstra T., Mendez J.C., Li J., *Environ. Sci. Nano*, **2019**, 3, 820-833.

Kappel C, Kemperman A.J.B., Temmink H., Zwijnenburg A., Rijnaarts H.H.M., Nijmeijer K., *J. Mem. Sc.*, **2014**, 453, 359-368

Kraal P., Dijkstra N., Behrends T. and Slomp C. P., *Geochim. Cosmochim*. Acta, **2017**, 204, 140–158.

Mao Y. Zhao Y. Cotterill S. *Water* **2023**, 15(8), 1455

Maha Lakshmi P., Sivashanmugam *P. Separation and Purification Technology*, **2013**, 116, 378-384

Martin-Domínguez A, García-Espinosa J.E., Panamá-Tirado L.A. Martín-Domínguez I.R., Alarcón-Herrera M.T., *Proceedings of the IWA World Water Congress and Exhibition*. **2008**. Vienna, Austria. 662572.

Martínez-Villafañe J.F., Ortiz-Cuellar J.C., Galindo-Valdés J.S., Cepeda-Rodríguez F, Gómez-Casas J, Rodríguez-Rosales N.A., Gómez-Casas O, Muñiz-Valdez C.R., *Sustainability,* **2022**, 14(19), 12096

Misawa T. ; Hashimoto K.; Shimodai.S, *Corrosion Science* **1974,** 14, (2), 131-149.

Moreno H.A., Cocke D.L, Gomes J.A.G., Morkovsky P., Parga J.R., Peterson J. and Garcia C.. ECS Transactions, **2007**, 6 (9) 1-15

Moussa D.T., El-Naas M.H., Nasser M., Al-Marri M.J. *J. Env. Management*, **2016**, 1-18

Müller S., Behrends T, van Genuchten G.M., *Water Research*, **2019**, 155, 455-464

Nidheesh P.V. and Gökkuş Ö. *Separation and Sci. Tech*., **2023**, 1, 1-50.

Refait P.H., Abdelmoula M., Genin J.M.R, *Corrosion Science* **1998,** 40, (9), 1547-1560.

Refait P.; Abdelmoula M, Genin G.M.R, Sabot R., *Comptes Rendus Geoscience* **2006,** 338, (6-7), 476-487.

Scholz R.W., Steiner G., *Mineral Economics,* **2022**, 35:745–763

Suresh K. Tang T. Van Vliet M.T.H., Bierkens M.F.P., Strokal M., Sorger-Domenigg F. Wada Y., *Environ. Res. Lett.,* **2023**,18, 063004

Timmes TC, Kim HC, Dempsey BA, *Desalination*, **2010**, 250, 6–13

STOWA (Stichting toegepast water onderzoek), *Handbook for N- and P-removal from communal wastewaters at wastewater treatment plants*, **2017,** 46.

Van Dijk K.C., Lesschen J.P., Oenema O., *Sc. Total Environment, Volume*, **2016**, 542, Part B, 1078-1093

Van Genuchten C.M., Addy SEA, Pena J., Gadgil A.J., *Environ. Science Tech.,* **2012**, 46, 986-994.

Vicente C, João R. Silva J.R., Santos A.D., Silva J.F., Mano J.T., Castro L.M., *Chemosphere*, **2023**, 328, 138500

Waychunas G.A., Fuller C.C., Davis, J.A., *Geochimica et Cosmochimica Acta*, **2003**, 7, 66, 1119-1137

WWAP, UNESCO, *The United Nations World water development report* **2017**. Wastewater: the untapped resource

Xu L, Xu X, Cao G, Liu G, Duan Z, Song S, Song M, Zhang M. *J. Env. Management* **2018**, 218, 129-138

Yang Z-H, Xua H-Y, Zenga G-M, Luo Y-L, Yang X, Huang J., Wanga L-K, Songa P-P., *Electrochimica Acta* **2015**, 153, 149–158

2

The formation of ferrihydrite during iron electro-coagulation.

Abstract. Iron Electrocoagulation (Fe-EC) is a widely used water treatment technology for removing heavy metals and hazardous anions, among other substances, from wastewater. The removal process involves generating iron oxyhydroxides through the in-situ corrosion of steel using direct current (DC), and utilizing these iron oxyhydroxides as adsorbents. The preferred iron oxyhydroxide for scavenging and removal is ferrihydrite (2-line type), which offers a large specific surface area (250-1100 m^2/g) and numerous sorption sites ($\equiv$Fe-OH) per unit of generated Fe(III). However, analysis of rust product composition often reveals the presence of crystalline lepidocrocite and goethite, which have lower sorption capacities than ferrihydrite (Karapinar (2016)). This study reveals that ferrihydrite is formed during the operation of an aerated DC Fe-EC cell at current densities ranging from 6.25 to 25 A/m^2. However, the ferrihydrite quickly transforms into lepidocrocite and/or goethite. This rapid transformation is directly related to the inadequate oxidation of Fe(II) by dissolved oxygen (O_{2aq}), as well as the reductively catalyzed transformation of ferrihydrite through electron transfer between ferrihydrite and Fe(II). To enhance the production of ferrihydrite, several approaches can be taken to inhibit the reductive transformation mediated by Fe(II): 1) Adding pre-synthesized ferrihydrite seeds at the beginning of the Fe-EC process, 2) Increasing the supply rate of $O_{2(aq)}$ through vigorous aeration (resulting in 30% ferrihydrite formation), 3) Adding 1.0 V% H_2O_2 to enhance the oxidation rate of Fe(II). This method resulted in the production of over 90% ferrihydrite. The strong adsorption capacity of rust phases mainly composed of ferrihydrite (produced with 1.0 V H_2O_2) is confirmed by achieving over 99% removal of PO_4, compared to only 40% removal with rust dominated by lepidocrocite and goethite.

2.1. Introduction.

The widespread amphoteric nature of iron oxides, hydroxides, and oxyhydroxides (hereafter referred to as "iron oxyhydroxides") allows for the removal of hazardous and toxic pollutants like Cu(II), Zn(II), Cd(II), Pb(II), Cr(III,VI), Se(IV,VI), As(III,V) from wastewater (Schwertmann and Fischer (1973), Smith et al. (1996), Trivedi and Axe (2000), Richmond et al. (2004), Holt et al. (2005), Moreno et al. (2007), Qian et al. (2009), Von der Heyden (2015), Karapinar (2016), Hiemstra et al. (2019)). Among all the known iron oxyhydroxides, the 2-line form of ferrihydrite has the highest adsorption capacities due to its large BET specific surface area (250-1100 m^2/g) and numerous sorption sites ($\equiv$Fe-OH) per nm^2 of surface area (Hiemstra et al. (2019)). The nano-crystalline structure of ferrihydrite allows for surface precipitation, such as the incorporation of trace contaminants like Zn(II) into its crystal lattice (Waychunas et al. (2003)). Ferrihydrite exists in the forms of 2-line and 6-line modifications, with the 2-line form having a higher adsorption capacity than the 6-line form (Cornell and Schwertmann (2003)). When freshly formed by rapid Fe(III)-hydrolysis, the specific surface area of 2-line ferrihydrite can reach up to ~1000 m^2/g (Hiemstra et al. (2019)). Various chemical formulas have been suggested for ferrihydrite in the literature, including $Fe(OH)_3$ (unconfirmed), $Fe_5O_7OH.5H_2O$, $Fe_{1.55}O_{1.66}OH_{1.34}$ (6-line, Stanjek and Weidler (2002)), with $Fe_5O_7OH.5H_2O$ being the most commonly used. However, most studies on the oxidation of ferrous (Fe(II)) and metallic iron (Fe(0)) report the presence of more stable phases such as lepidocrocite (γ-FeOOH), goethite (α-FeOOH), maghemite (γ-Fe_2O_3), and magnetite (Fe_3O_4) (Kiyama et al. (1972), Misawa et al. (1974), Music et al. (1993), Oh et al. (2002), Mukesh and Panday (2001), Zhang and Huang et al. (2006), Van Genuchten et al. (2014), Chen and Thompson (2018)), as determined by techniques like XRD, XPS, ATR-FTIR, EXAFS, etc. The commonly suggested mechanism for their formation is the direct precipitation of small polymeric entities (dimers, tetramers) into lepidocrocite or long chains of Fe(III)-polymers into goethite (Blesa and Matijevic (1989), Scheck et al. (2016)). However, there is also an alternative explanation that involves catalytic processes, as described by Tronc et al. (1992), Liu et al. (2007), Hansel et al. (2005), Pedersen et al. (2005), Yee et al. (2006), Boland et al. (2013, 2014)' Gomez (2020), and the recent works of Sheng et al. (2020, 2021) and Liu et al. (2023). These studies have demonstrated that Fe(II) ions catalyze the transformation of ferrihydrite into lepidocrocite and goethite at rates 100 to 1000 times higher than those without Fe(II) ions (Cudennec and Lecerf

(2006)). This catalytic process involves the reductive dissolution of ferrihydrite through electron transfer between adsorbed Fe(II) and ferrihydrite. New insights from isotopic tracking with Fe^{57} have shown that the electron transfer oxidizes the adsorbed Fe(II) to Fe(III) (Notini et al. (2022)), which then detaches and periodically accumulates in the solution, leading to the precipitation of secondary phases like lepidocrocite and goethite. This intermediate Fe(III) is referred to as "labile Fe(III)" and can be detected using Xylenol orange. Although its composition is still unclear, the aqueous complexation of labile Fe(III) with Xylenol orange, forming (Fe^{3+}-XO complexes), suggests that a large fraction of this labile Fe(III) consists of Fe(III)-ions along with small quantities of oligomers. The rate of electron transfer between Fe(II) and ferrihydrite is generally faster than the consumption rate of labile Fe(III), resulting in the periodic labile [Fe(III)] of 0.1-0.4 mM. This high concentration exceeds the apparent solubility of ferrihydrite, lepidocrocite, and goethite (Sheng et al. (2020) and Liu et al. (2023)). According to Ostwald's rules of stages, this sustains the formation of ferrihydrite under such high supersaturation. However, recent fast XRD tracking of the ferrihydrite surface suggests that the electron transfer between Fe(II) and ferrihydrite forms magnetically ordered proto-lepidocrocite lamellae (Latta et al. (2023)). Sheng et al. developed a kinetic model that describes the precipitation of intermediate labile Fe(III) on the surface and initiates the nucleation of lepidocrocite and/or goethite. The crystal growth of these nuclei is then sustained by the large fraction of dissolved labile Fe(III) in the adjacent aqueous medium. However, the mechanisms that differentiate the formation of lepidocrocite and/or goethite initial nuclei remain poorly understood, particularly the surface polymerization reactions, such as olation and oxolation (Cudennec and Lecerf (2006)), that determine whether lepidocrocite or goethite evolves on the ferrihydrite surface. Many parameters, such as pH, Fe(II) speciation, and anion binding, can affect the surface charge, the speciation of formed Fe(III), and the type of nuclei formed. One important parameter is the surface charge, which strongly depends on the adsorption of Fe(II) onto the ferrihydrite surface. While the reduction potential of pure ferrihydrite is around +0.05 V (Thampdrup (2000)), cycling voltammetry studies in Fe(II)-ferrihydrite systems have shown that Fe(II) adsorption generates a surface potential ranging from 0.10 to -0.20 V depending on the surface occupation of Fe(II) (Xie et al. (2019)). Due to the higher thermodynamic stability and more ordered structure of lepidocrocite and goethite, their reduction potentials are generally reflected in lower values, ranging from -0.05 to -0.1 V and -0.2 V at pH 7.0, compared to ferrihydrite (Aeppli et al. (2019)). The adsorption of Fe(II) and the resulting surface potentials have not been directly linked to the formation of secondary phases through Fe(II)-catalyzed reductive transformation. However, the adsorption of Fe(II)

and the formation of surface complexes may determine the surface potential and provide the initial nuclei for the formation of goethite and lepidocrocite. Given the significant enhancement of ferrihydrite transformation by Fe(II), any rapid transformation of ferrihydrite is of great relevance for wastewater treatment, as it can decrease the required amount of Fe(III) for efficient contaminant removal (Fei et al. (2018), Lu et al. (2023)).

The technique used to study the formation of ferrihydrite is called iron electro-coagulation (Fe-EC). In this technology, steel or Fe(0) (C-steel, cast iron, or mild steel) is oxidized at controlled rates of direct current corrosion, resulting in the production of stoichiometric amounts of iron oxyhydroxides according to equations 1.1-1.12 (Mollah et al. (2001); Mollah et al. (2004); Liu et al. (2010); Moussa et al. (2017); Shahedi et al. (2020); Boinpaly et al. (2023)). The electrolyte (or the wastewater being treated) is oxygenated through processes such as aeration or mixing, which causes the electrochemically generated Fe(II) (Fe(0) = Fe(II) + 2 e-) to be oxidized by dissolved $O_{2(aq)}$ from the air, resulting in the formation of Fe(III) ions and the precipitation of iron oxyhydroxides. Ferrihydrite has been identified as one of the components of the rust phase, along with lepidocrocite, goethite, and magnetite (Van Genuchten et al. (2014, 2018)). Despite characterizing ferrihydrite, there is limited knowledge about the optimal conditions for its formation through the Fe-EC process. Since ferrihydrite is produced by the oxidation of Fe(II), there may be situations where not all Fe(II) ions are fully oxidized (as indicated by equations 1.1-1.12), such as during high current operations (> 1000 A/m^2) or when there is insufficient supply of $O_{2(aq)}$ to the electrolyte. These situations could potentially lead to a reductive transformation of ferrihydrite, which could explain why the formation of ferrihydrite is scarce in Fe-EC systems. It has been observed that the Fe(II)-mediated transformations occur over periods longer than 10 hours (Boland et al., (2013, 2014), Sheng et al. (2021), Liu et al. (2023)), while the formation and removal of the rust phase, along with the removal of contaminants, generally take a total period of 1-5 hours. It is uncertain whether ferrihydrite actually forms and transforms within this short period of time (< 5 hours), or if other stable phases like lepidocrocite and goethite dominate from the beginning of the Fe-EC process. Therefore, it is crucial for the application of Fe-EC to investigate the formation and potential transformation of ferrihydrite, as well as to explore ways to minimize its transformation into crystalline forms.

This work was dedicated, in the first place, to studying the formation of ferrihydrite during the Fe-EC process at relatively low current densities (6.25-25 A/m^2) in order to achieve controlled Fe(0) corrosion rate and oxygenated conditions. Secondly, the aim was to enhance the production of ferrihydrite by minimizing its transformation through various methods: 1)

adding synthetic ferrihydrite seed, 2) increasing the oxygen content in the electrolyte, or 3) incorporating highly oxidative H_2O_2 (1 V%) into the electrolyte.

2.2. Experimental

2.2.1. Experimental equipment (sampling, analysis)

The experiments were conducted in an electrochemical cell consisting of a temperature-controlled reaction vessel (V = 200 ml) with two Fe(0) electrodes made of mild carbon steel (R235) composed of 99.5% Fe and 0.5% C. O_2 was measured using an HQ40d Multi-meter, and pH was measured using a SenTix 41 pH-electrode from WTW, Germany. The Fe(0) electrodes were placed 4 cm apart from each other. A portion of the electrode surface was covered with Teflon to create an active surface area of 20 cm^2 (4 x 5 cm). The two Fe(0) electrodes were connected to a potentiostat (Model ES 030-5 Delta Elektronika) and corroded by setting the current density using a 2-digit setting. The current was also measured using a multimeter. The temperature was set to 25 °C for all the experiments. The set-up was further equipped with an acid-base titration system, which was coupled to the pH-electrode to control the pH within a range of 0.1 pH units.
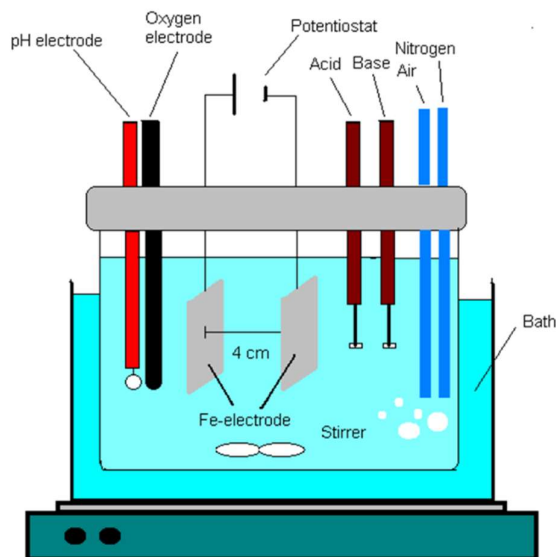

Fig. 2.1. *Experimental temperature-controlled set-up of the Fe-EC cell, equipped with acid-base dosage system for pH control*

2.2.2. Experimental procedure for transformation of synthetic ferrihydrite during Fe-EC under deoxygenated conditions

Fe-EC experiments were conducted at current densities of 3.13 and 6.25 A/m^2, using two-line ferrihydrite under deoxygenated conditions and 0.25M Na_2SO_4 as the background electrolyte (Tab. exp. 1 and 2). The Fe(0)-electrodes were immersed in this electrolyte and placed in the setup described above (Fig. 2.2). Ferrihydrite exists as two-line and as six-line compounds. For this study, two-line ferrihydrite was selected due to its higher specific surface area, making it the preferred form for water treatment purposes. Ferrihydrite was synthesized according to the procedure described in Cornell and Schwertmann (2003) with a final [Fe(III)] (as a suspension of two-line ferrihydrite) of 2 g (35.8 mM) [Fe(III)]/L. 20 ml of this suspension was added to a solution containing 180 ml of deionized Milli-Q water with a background electrolyte of 0.25M Na_2SO_4, resulting in a final concentration of 200 mg Fe(III) (3.58 mmol)/L in the form of ferrihydrite. Any traces of $O_{2(aq)}$ were eliminated by purging $N_{2(g)}$ through the electrolyte, and the intrusion of $CO_{2(g)}$ was prevented by continuously purging $N_{2(g)}$ through an alkaline solution. The solution was purged with N_2-gas for 2 hours prior to the start of the experiment to remove any dissolved $O_{2(aq)}$. Volume and mass changes due to evaporation were corrected by adding deionized water. The reactor was sealed with PTFE caps throughout the experiment to prevent any entry of $O_{2(g)}$ into the reactor suspension. During the electrolysis, the solution's pH was maintained at a constant value of 7.0 by making minor additions of 0.1 M H_2SO_4 and 0.1M NaOH using the acid-base titration systems described in section 2.2.1. The stirring rate was consistently maintained at 750 rpm for all experiments. The $[O_{2(aq)}]$ in the reactor was continuously monitored using an electrode.

2.2.3. Experimental procedure for Fe-EC at oxygenated conditions

Using the same Fe-EC setup as described in section 2.2.1 and the operational setup outlined in section 2.2.2, we conducted an additional series of Fe-EC experiments at current densities of 6.25, 12.5, and 25.0 A/m^2 without the presence of ferrihydrite seeds. The objective was to investigate the formation of ferrihydrite solely by the Fe-EC process itself and its production as a function of current density (exp. #3-5). To oxidize the Fe(II) ions generated electrochemically, the electrolyte was exposed to the atmosphere to allow continuous intrusion of O2(g) which subsequently reacted with the Fe(II) to form Fe(III) (eq. 1.2). This facilitated the precipitation of Fe(III) ions as ferrihydrite, lepidocrocite, and/or goethite. Throughout the experiments, the reactive solution was consistently homogenized by stirring using a floating 1-

inch magnetic stir bar (Nalgene). A stirrer speed of 750 rpm was employed, which provided moderate aeration of the electrolyte, ensuring that only a small amount of the electrochemically generated Fe(II) remained unoxidized. This allowed us to study the influence of Fe(II) on the formation of ferrihydrite at elevated concentrations.

Table 2.1. *Overview of the parameters of the performed experiments. All experiments were carried out in an electrolyte with background electrolyte containing 0.25M Na_2SO_4.*

Exp.#	J (A/m^2)	Stirring rate (rpm)	Atmospheric Conditions	Ferrihydrite[1] seeds (mg/L)
1	3.12	750	Closed (N$_2$-atm)	200 (3.58 mM)
2	6.25	750	Closed (N$_2$-atm)	200 (3.58 mM)
3	6.25	750	Open	-
4	12.5	750	Open	-
5	25.0	750	Open	-
6	12.5	750	Open	200 (3.58 mM)
7	12.5	750	Open	400 (7.16 mM)
8	12.5	750	Open	800 (14.32 mM)
9	12.5	250	Open	-
10	12.5	500	Open	-
11	12.5	1000	Open	-
12	12.5	1000+(1%H$_2$O$_2$)	Open	-

[1] Ferrihydrite seeds were produced according to a procedure adopted from Schwertmann and Cornell (2000)

A second set of experiments (exp. #6 - 8) was conducted to investigate the impact of adding ferrihydrite seeds at the beginning of the Fe-EC run on ferrihydrite productivity under aerated conditions. These experiments involved running Fe-EC with a current density of 12.50 A/m^2 using an electrolyte suspension containing synthetic 2-line ferrihydrite with total $c(Fe(III))_s$ of 200 (3.58 mM), 400 (7.16 mM), and 800 (14.32 mM) mg Fe(III)/L (exp. #6 - #8).

In addition to the Fe-EC test conducted at 750 rpm (moderately high, exp. #4), a third set of experiments (exp. #9 - 12) were performed to study the effect of varying the O_2 supply or oxygenation of the electrolyte on ferrihydrite formation. These experiments involved running Fe-EC at different stirring rates and aerated conditions. The solution was mixed at 250 (slow), 500 (moderate), and 1000 (vigorous) rpm (exp. #9 - 11). Furthermore, additional experiments were conducted at 1000 rpm with 1% H_2O_2 added to the electrolyte (exp. #12). In these experiments, the current density was kept constant at 12.5 A/m^2.

2.2.4. Sampling, analysis and overview of the experiments

In each experiment, 2 mL samples were taken using a syringe and filtered directly through a 0.2 μm filter under N_2-blanketing (deoxygenated for 10 minutes with N_2-purging). The supernatant was quickly acidified (pH~3.0) to minimize the oxidation of Fe(II). The concentration of Fe(II), denoted as $[Fe(II)]_T$, was then determined using the 1,10-orthophenanthroline method with a XION 500 Spectrophotometer (APHA 2005). The precipitate on the filter was thoroughly washed with N_2-purged deionized water to remove any dissolved Fe(II), and then dried under N_2-gas atmosphere. For experiments conducted under oxygenated conditions (i.e., experiments 3-12), the concentration of Fe(III) in the precipitate was calculated by subtracting the determined aqueous $[Fe(II)]_T$ from the total amount of Fe(II) formed during electrolysis. The theoretical total amount of Fe(II) formed was calculated using Faraday's Law [28]:

$$n(Fe^{2+})_T = \frac{J.A_{elec}.60.t}{z.F} \qquad [moles] \qquad\qquad \text{eq. 2.1}$$

Where J is the current density (A/m^2), t is the duration (min.), A_{elec} is the active corrosion area of the anode (0.0020 m^2), z is the number of electrons transferred per molecule (z = 2 for reaction Fe^0 to Fe^2+), and F is the Faraday constant (96485 C/mol).
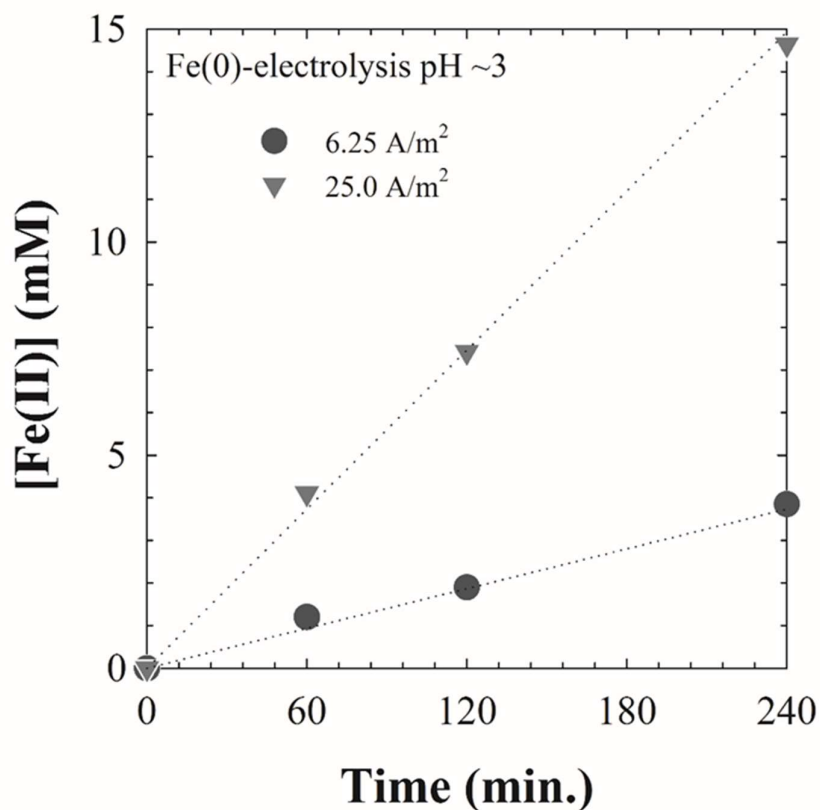
Fig. 2.2. *Fe-EC was carried out at two current densities of 6.25 and 25.0 A/m², while maintaining a stirrer speed of 750 rpm. The pH was maintained at pH 3.0 to prevent oxidation of the electrochemically generated product. The [Fe(II)]$_T$ was measured following the procedure described in Section 2.2.1 (n = 2). The dotted line on the graph represents the theoretical value, assuming a 100% current efficiency in the conversion of Fe(0) to Fe(II), as described in equation 2.1. The actual current efficiency for both current densities was measured to be 98%.*

Fig. 2.2 shows the results of Fe-EC experiments conducted at current densities of 6.25 and 25.0 A/m² under pH 3 conditions. The graph illustrates a linear relationship between the theoretical values calculated using Equation 2.1 and the measured [Fe(II)]$_T$, following Equation 1.1. This indicates a high current efficiency of 99% ± 2% (n = 2) for the electrochemically produced Fe(II) by Fe-EC, consistent with the findings of Lakshmanan et al. (2009) that Fe(II) is primarily formed through the oxidation of Fe(0), with no significant occurrence of other reactions such as direct Fe(III) and $O_{2(aq)}$ evolution at the anode under the tested conditions.

The experimental results demonstrate that the self-corrosion of Fe(0) plates is negligible (refer to Fig. 2.1 for the experimental setup) and that Fe(0) continuously generates Fe(II) ions. The Fe(II) ions in the electrolyte are simply oxidized by dissolved $O_{2(aq)}$, and this process can

be effectively controlled by adjusting the current density and the supply of $O_{2(aq)}$ to the electrolyte, as depicted in the Fe-EC cell setup shown in Fig. 2.1.

To ensure that there is no interference from other reactions during the oxidation of Fe(II) and the formation of the desired phase, the aforementioned current densities and O2(aq) supply conditions were used for the electrochemical tests described above (see test parameters in Tab. 2.1).

To characterize the iron oxyhydroxides formed during Fe-EC tests, we applied ATR-FTIR-spectra techniques to obtain FTIR data at wave numbers ranging from 500 to 1300 cm^{-1} using a Shimadzu 4800-sn spectrometer. Ferrihydrite was characterized by the broad vibration OH-bands of Fe-OH at 600 and 690-700 cm^{-1} (Schwertmann, 1973; Jia et al., 2007; Villacís-García et al., 2015; Russell et al., 2018). For lepidocrocite and goethite, the bending vibration bands of OH for Fe-(OH) were observed at 745, 1020, and 1155 cm^{-1}, and 789 and 880 cm^{-1}, respectively (Tejedor-Tejedor, 1986; Weckler and Lutz, 1998; Villacís-García, 2015; Dutrizac et al., 1987). Sulfate, on the other hand, exhibited a broad band between 900-1200 cm^{-1} (Persson and Lövgren, 1996).

Table 2.2. *Wavenumbers of iron oxyhydroxides seen in the ATR-FTIR spectra..*

Iron oxyhydroxide type	Wavenumbers (cm^{-1})
Ferrihydrite (2- or 6-line)	~600 (v(Fe-O)$_{sym}$) ~690 (Fe-OH)$_{sym}$
Lepidocrocite	749 (v(Fe-O)$_{sym}$), 1020 (Fe-OH)$_{sym}$ and 1115 (Fe-OH)$_{asym}$
Goethite	800 (Fe-OH)$_{sym}$, 890 (Fe-OH)$_{asym}$

References: Dutrizac et al. (1987) Music et al. (1993), Weckler and Lutz (1998), Ruan et al. (2002) and Wijnja and Schultless (2002) and Villacís-García (2015)

2.2.5. Surface complexation model for the assessment of Fe(II) adsorption to ferrihydrite.

To evaluate the influence of Fe(II) surface adsorption on the reductive transformation of ferrihydrite (i.e., dissolution), we utilized the Visual Minteq program to determine the Fe(II) surface complexation onto active sites of ferrihydrite, specifically the ≡Fe-OH. Since ferrihydrite comprises both "weak" and "strong" binding sites (identified through Zn(II) adsorption to 2-line ferrihydrite), we adopted the 2-site binding model developed by Dzombak and Morel (1990) from the PHREEQC code for this analysis of surface complexation. This model assumes a standard surface area (A_s) of 250 m^2/g and a pK_a value of 7.29 for the ≡Fe-OH, which typically corresponds to synthetic ferrihydrite that has undergone a significant aging

period to promote structural aggregation (used in exp. #1 and #2). However, the ferrihydrite formed in-situ through the Fe-EC process (exp. #3-5) likely resembles freshly formed ferrihydrite and possesses higher values of A_s (~600 m^2/g, according to Hiemstra et al. (2019) wherein ferrihydrite was evolved for 30 minutes) and a higher pK_a value (7.9) compared to aged ferrihydrite. Consequently, higher pK_a values for the $\equiv$Fe-OH surface complexation with Fe(II) are employed. A more detailed discussion on this topic is provided in section 2.5. Table 2.3 consolidates the employed surface complexation model for Fe(II) adsorption onto aged and freshly generated ferrihydrite (2-line form).

Table 2.3. *Visual Minteq modelling parameters and corresponding surface complexation reaction for adsorption of Fe(II) on 2-line ferrihydrite.*

Reaction	Log K[b]	pH$_{pzc}$	OH/nm^2 [(b)]	A_s (m^2/g) [b]
Synthetic aged ferrihydrite (> 1 year aging)				
$\equiv$Fe-OH$^{+0.5}$ $\leftrightarrow$ $\equiv$Fe-O$^{-0.5}$ + H$^+$	8.1[b]	8.1[b]	4.5	250
$\equiv$Fe-OH + Fe(II) + H$_2$O $\leftrightarrow$ $\equiv$Fe-O-FeOH + 2H$^+$	-11.55			
$\equiv$Fe-OH + Fe(II) $\leftrightarrow$ $\equiv$Fe-O-Fe$^+$ + H$^+$	-2.98			
In-situ formed ferrihydrite (evolution time ~30-60 min)				
$\equiv$Fe-OH$^{+0.5}$ $\leftrightarrow$ $\equiv$Fe-O$^{-0.5}$ + H$^+$	8.7[a]	8.7[a]	6.0	600
$\equiv$Fe-OH + Fe(II) + H$_2$O $\leftrightarrow$ $\equiv$Fe-O-FeOH + 2H$^+$	-11.55			
$\equiv$Fe-OH + Fe(II) $\leftrightarrow$ $\equiv$Fe-O-Fe$^+$ + H$^+$	-2.98			

[a] Jain et al. (1999),

[b] Hiemstra and Zhao (2016)

[c] Dzombak and Morel (1990)

2.3. Results and discussion.

2.3.1. The transformation of synthetic ferrihydrite by accumulating Fe(II)-ions in deoxygenated EC process conditions.

The transformation of ferrihydrite (2-line) to lepidocrocite (γ-FeOOH) and goethite (α-FeOOH) follows a recrystallization process in which ferrihydrite dissolves into Fe(III) ions and simultaneously re-precipitates as goethite and/or lepidocrocite (Schwertmann et al. (1999), Jolivet et al. (2006), Yee et al. 2006). In the absence of Fe(II)$_{(aq)}$, the very low solubility of metastable ferrihydrite (expressed as K_{SP}(ferrihydrite) = [Fe^{3+}][OH$^-$]^3= 10$^{-37.5}$ according to

Schwertmann (1991)) at a pH of 7.0 and room temperature conditions, as well as that of the more stable oxyhydroxides like goethite ($K_{SP}(\alpha\text{-FeOOH, goethite}) = 10^{-42.4}$) and lepidocrocite ($K_{SP}(\gamma\text{-FeOOH, lepidocrocite}) = 10^{-41.5}$), leads to a very slow transformation process that can take months to years to complete (Schwertmann et al. (1999) observed an 80% transformation rate). However, with the presence of $Fe(II)_{(aq)}$ (covering a range of ($FeCl_2$ or $FeSO_4$)/$Fe(III)_{Fh}$ from 0.01 to 1.0), the transformation rates to lepidocrocite or goethite are significantly increased, with 90-100% transformation achieved within a much shorter period of 5-10 hours (Tronc et al. 1992, Pedersen et al. (2005), Hansel et al. (2005), Boland et al. (2013, 2014), Notini et al. (2022), Sheng et al. (2020,2021)). Even less crystalline forms of ferrihydrite (formed through rapid hydrolysis) can transform within a shorter period of less than 2 hours. Considering that the time required to remove cations (such as Cd(II), Pb(II), Cu(II), or Zn(II)) from wastewater streams ranges from a few hours (for instance, Pb(II)) to hours (when treated with Fe-EC at a standard current density of 0.1-5 A/m^2), a reductively driven transformation of ferrihydrite to more stable lepidocrocite and goethite, which have lower sorption capacity, can significantly affect the removal of metal cations from wastewater. Moreover, the local pH near the cathode and the anode surface reactions (passivation) may further enhance the transformation rates by increasing the adsorption of Fe(II) on ferrihydrite. In this study, we aim to investigate the Fe(II)-induced transformation of ferrihydrite to lepidocrocite and/or goethite within typical time periods used for treating wastewater streams with Fe-EC technology.

To evaluate the effects of Fe(II) and the operating parameters of the Fe-EC cell on the transformation of ferrihydrite, we conducted a Fe-EC experiment. The experiments were carried out using a continuously deoxygenated suspension containing synthetic ferrihydrite (aged for 1 week prior to the test), with an initial [Fe(III)] of 3.58 mM (200 mg Fe(III)/L). The purpose was to accumulate Fe(II) electrochemically at a constant rate.

Two experiments were conducted, one with a current density of 3.13 A/m^2 (experiment #1) and the other with a current density of 6.25 A/m^2 (experiment #2). The ATR-FTIR spectra of the resulting phases are shown in Figure 2.3.

In the experiment with a current density of 3.13 A/m^2, the initial ferrihydrite (denoted as Fh in Figure 2.3) transformed into goethite within the first 10-60 minutes of Fe(II) accumulation in the electrolyte. The transformation occurred at a faster rate when the current density was doubled to 6.25 A/m^2. This transformation was observed qualitatively through the gradual appearance of the bending modes of $\equiv$Fe-OH at 800 and 880 cm^{-1}, characteristic of goethite (denoted as G), compared to the bending vibration of ferrihydrite at 690 and 580 cm⁻

[1]. Additionally, a small fraction of the adsorbed SO_4^{2-} on these phases, originating from the electrolyte, was represented by a prominent peak at 980 cm^{-1}.
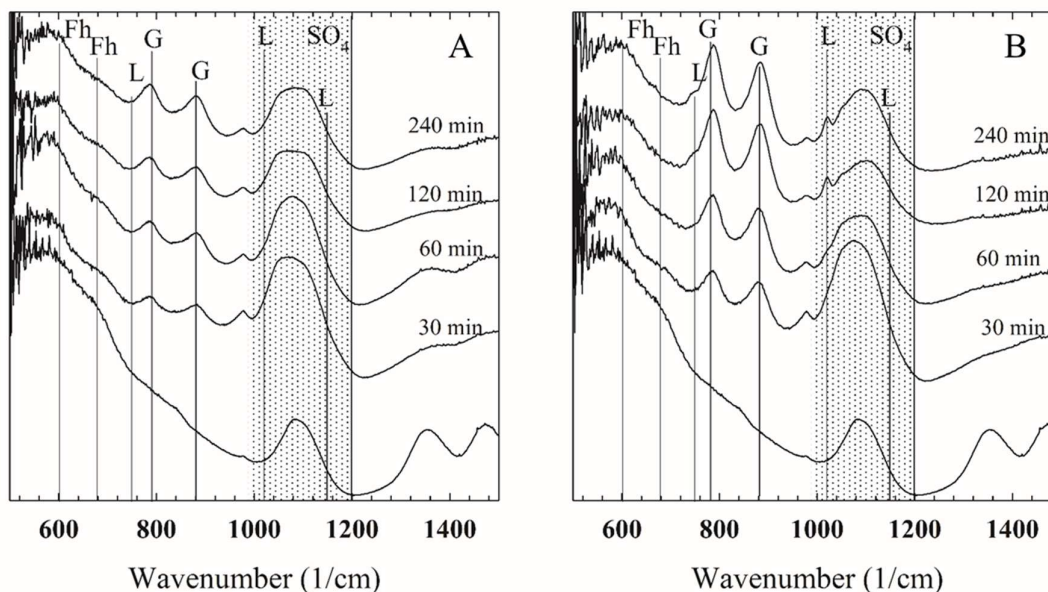

Fig. 2.3. *The ATR-FTIR spectra of iron oxyhydroxides obtained during the deoxygenated Fe-EC run in the presence of synthetic ferrihydrite seeds, with a $c(Fe(III))_s$ = 200 mg/L or 3.58 mM (exp. #6 and #7), were analyzed. The experiments were conducted under deoxygenated conditions with current densities of (A) 3.13 A/m^2 and (B) 6.25 A/m^2 (Tab.2.1), resulting in the production of Fe(II) exclusively. The symbols G, L, and Fh represent the vibrational modes of goethite, lepidocrocite, and ferrihydrite, respectively (refer to Tab. 2.1 for the corresponding wavenumbers). The lower spectrum corresponds to pure ferrihydrite synthesized according to Cornell and Schwertmann (2003).*

In Fig. 2.4, the values for the formed $[Fe(II)]_T$ divided by the amount of added ferrihydrite seeds ($[Fe(III)]_T$ = 200 mg/L, 3.58 mM), are represented as $[Fe(II)]_T/c(Fe(III))_{(s)}$ ratios. This ratio has been chosen as a parameter in order to comprehend the resulting products, as it provides a direct and reliable indication of mass balance, unlike active surface areas which are challenging to evaluate *in-situ*.

These values are compared with the corresponding theoretical ratios assuming 100% current efficiency in Fe(II) production (Fig. 2.2 for Fe-EC run at pH 3 shows a current efficiency of over 99%). The theoretical ratio was calculated using equation 2.1. Basically, the uptake of Fe(II) by ferrihydrite would result in the formation of coprecipitates such as

magnetite ($Fe^{2+}Fe^{3+}_2O_4$), causing the experimental $[Fe(II)]_T/c(Fe(III))_{(s)}$ ratios to be lower than the theoretical value. Firstly, based on the reasonable match between the experimental and theoretically determined ratios in Fig. 2.4, we can conclude that there is no significant net uptake of $Fe(II)_{(aq)}$ ions by the ferrihydrite phases, except for some temporary adsorption at the beginning of the experiment (30-60 min), followed by the release of Fe(II) into the electrolyte as the transformation progresses. The slight deviation in the $[Fe(II)]_T$ vs. the theoretical ratio can be explained by the association of Fe(II) with ferrihydrite (Sheng et al., 2020). Secondly, even at a low $[Fe(II)]_{(aq)}/c(Fe(III))_{(s)}$ ratio (<0.1) after 30 minutes, the transformation was already noticeable (Fig. 2.3), resulting in the formation of goethite that remains stable and does not transform into magnetite even at higher $[Fe(II)]_{(aq)}/c(Fe(III))_{(s)}$ ratios (>0.33). This finding is consistent with previous studies by Tronc et al. (1992), Hansel et al. (2005), Yee et al. (2006), Liu et al. (2007), Boland et al. (2014), Notini et al. (2022), and Sheng et al. (2022), all of whom proposed the idea that Fe(II) acts as a catalyst for the dissolution of ferrihydrite.
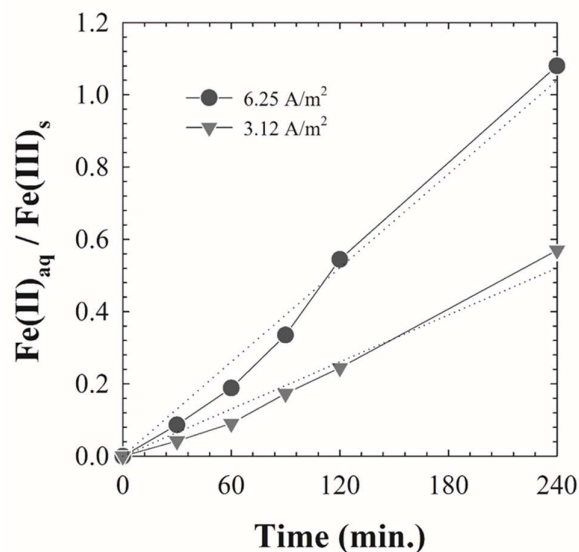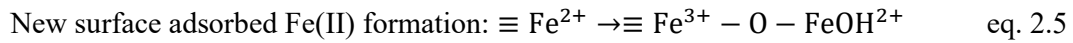

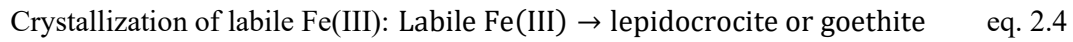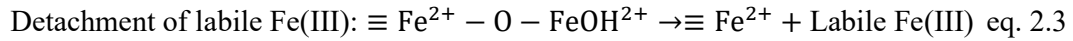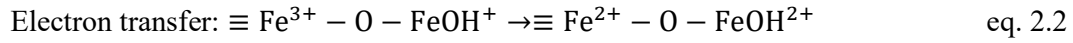**Fig. 2.4.** *Experimental (solid curves) and theoretical (dashed lines) curves of $[Fe(II)]_T$ vs. time and $Fe(II)_{aq}$ vs. $Fe(III)_s$ time were obtained from the deoxygenated Fe-EC in the presence of synthetic ferrihydrite phases with $c(Fe(III))_s = 200$ mg/L or 3.58 mM (experiments #6 and #7). The ferrihydrite seeds were synthesized according to Cornell and Schwertmann (2003).*

The most recent research on the reductively catalyzed transformation of ferrihydrite indicates that the process involves an electron transfer reaction between surface-associated Fe(II) and ferrihydrite (Sheng et al., 2020, 2021). Through this electron transfer, a reactive and labile Fe(III) intermediate is formed (Sheng et al., 2020), which temporarily accumulates in the electrolyte phase before reprecipitating to form either stable goethite or lepidocrocite. The three consecutive reactions that characterize the reductive transformation of ferrihydrite to goethite (or lepidocrocite) are described as follows:

Electron transfer: $\equiv Fe^{3+} - O - FeOH^+ \rightarrow \equiv Fe^{2+} - O - FeOH^{2+}$ eq. 2.2

Detachment of labile Fe(III): $\equiv Fe^{2+} - O - FeOH^{2+} \rightarrow \equiv Fe^{2+} +$ Labile Fe(III)   eq. 2.3

Crystallization of labile Fe(III): Labile Fe(III) $\rightarrow$ lepidocrocite or goethite   eq. 2.4

New surface adsorbed Fe(II) formation: $\equiv Fe^{2+} \rightarrow \equiv Fe^{3+} - O - FeOH^{2+}$ eq. 2.5

The first approach to understanding the driving force behind this electron transfer process was described by Yang et al. (2010) and Boland et al. (2014). They concluded that the electron transfer is driven by the difference in electrochemical potential between ferrihydrite and the electrolyte. In the electrolyte, the Fe(II)- and Fe(III)-ions form a redox couple. Due to the initially very low solubility of ferrihydrite, with [Fe(III)] = -17.5 M, even a slight presence of [Fe(II)] creates more reduced conditions than the oxic conditions of ferrihydrite (Fe(III)). This disequilibrium in redox conditions is believed to drive the electrons towards ferrihydrite, leading to reductive dissolution of the mineral. The electrolyte potential, $E_{h,elec}$, can be determined using the following Nernst equation, as stated by Boland et al. (2014) and Yang et al. (2010):

$$E_{h,elec} = E^0_{Fe^{2+}/Fe^{3+}} + 0.059 \log\left(\frac{\alpha(Fe^{2+})}{\alpha(Fe^{3+})}\right)$$ eq. 2.6

$E^0_{Fe2+/Fe3+}$ is the standard redox potential (+0.77 V), while α(Fe(II)) and α(Fe(III)) represent the activity of aqueous Fe(II) and Fe(III) ions, respectively. In the works of Boland et al. (2014) and Yang et al. (2010), α(Fe(III)) was determined for measuring the $E_{h,elec}$ by considering the solubility of ferrihydrite at RT and pH 7.0 ([Fe(III)] = α(Fe(III)) = 3×10^{-17} M), resulting in very low electrolyte potentials. However, it is important to note that this approach disregards the findings of Sheng et al. (2019), which revealed that labile Fe(III) forms rapidly upon interaction with Fe(II) and attains a significantly higher [Fe(III)]$_{labile}$ than what was

predicted based on ferrihydrite's original solubility. In fact, during the Fe(II)-induced recrystallization of ferrihydrite, a $[Fe(III)]_{Labile}$ of 0.10-0.40 mM (as reported by Sheng et al., 2020, 2021 and Liu et al., 2022) is frequently observed. Consequently, the solubility predictions in Boland et al. (2014) and Yang et al. (2010) are only applicable at the beginning of the catalytic process when Fe(II) is introduced to the ferrihydrite suspension, and the [Fe(III)] is still determined by the original solubility of ferrihydrite ([Fe(III)] = 3 x 10^{-17} M). However, as the transformation progresses and the labile [Fe(III)] rapidly increases to approximately 0.1-0.4 mM (within less than 30 minutes), a more oxidized $E_{h,elec}$ is established. This alteration in potential difference between ferrihydrite and the electrolyte hinders electron transfer. Despite the relatively constant labile [Fe(III)] increase to 0.1-0.4 mM throughout the transformation period, Eq. 2.6 indicates that $E_{h,elec}$ primarily remains in the oxidizing range of +0.45V, which is more oxidizing than the reduction potential required to convert ferrihydrite to goethite. Consequently, one would expect the transformation of ferrihydrite to cease quickly under such oxidizing conditions. However, the results clearly demonstrate that the transformation proceeds rapidly, even in the presence of this oxidizing state of the electrolyte. Therefore, it can be concluded that the use of $E_{h,elec}$ is insufficient to explain the observed catalytic transformation of ferrihydrite.

In a different approach, Li et al. (2019) indicated, through cyclic voltammetry (CV) techniques applied to Pt-electrodes covered with ferrihydrite, that the adsorption of Fe(II) onto ferrihydrite generates electron transfer with the underlying Fe(III), resulting in the formation of the $\equiv Fe^{3+}$-O-Fe^{2+} / $\equiv Fe^{2+}$-O-Fe^{3+} redox couple (as shown in eq. 2.2). The oxidation and reduction potentials of this redox couple were measured to be approximately +0.05V and -0.2V, respectively, with a half-wave potential ($E^{1/2}$) of -0.08V. This indicates that the adsorption of Fe(II) creates highly reduced surface redox conditions on ferrihydrite. For example, AQDS, which has an E^0 of -0.184V, was reduced to AH_2QDS in Fe(II)-ferrihydrite systems, but this reduction did not occur when only Fe(II) was reacting with AQDS, confirming the presence of a strong surface reduction potential upon Fe(II) adsorption. In the absence of Fe(II), the reduction potential of ferrihydrite, as measured by Li et al. (2019), was much lower at -0.031 V.

Although Li et al. (2019) observed the transformation of ferrihydrite to goethite during the CV tests, they did not correlate this finding with the work of Sheng et al. (2019), which suggests that the formation of the $\equiv Fe^{2+}$-O-Fe^{3+} complex leads to the detachment of Fe^{3+} from the surface more easily compared to the adsorption of Fe(II) to the $\equiv Fe^{2+}$-OH sites. In the absence of Fe(II), the reduction potential of ferrihydrite, as measured by Li et al. (2019), was

much lower at -0.031 V. Hence, the reduction of structural Fe(III) in ferrihydrite can occur when the surface reduction potential ($E_{h,surf}$) becomes more negative than the reduction potential of the ferrihydrite structure. This continuous electron transfer to the bulk phase can drive the reductively catalyzed transformation of ferrihydrite to lepidocrocite or goethite.

In this study, the $E_{h,surf}$ was used as a measure to indicate the occurrence of the reductively catalyzed transformation of ferrihydrite to lepidocrocite and/or goethite in the presence of Fe(II). The following active surface species on ferrihydrite were assessed to estimate the $E_{h,surf}$ (Li et al., 2019): [$\equiv Fe^{3+}$-O-Fe^{2+}], [$\equiv Fe^{3+}$-OH], and [$\equiv Fe^{2+}$-O-Fe^{3+}] (eq. 2.3 and 2.4). The [$\equiv Fe^{3+}$-O-Fe^{2+}] is an intermediate phase that is difficult to determine *in-situ* due to unknown equilibrium constants. However, the formation rates of labile Fe(III), resulting from the detachment of Fe^{3+} from the $\equiv Fe^{3+}$-O-Fe^{2+}-complex, are very fast reactions. Therefore, it can be assumed that $\equiv Fe^{3+}$-O-$Fe^{2+}$is largely in the form of $\equiv Fe^{3+}$-OH. Hence, we can approximate [$\equiv Fe^{2+}$-O-Fe^{3+}] $\approx$ [$\equiv Fe^{3+}$-O-Fe^{2+}]. The [$\equiv Fe^{3+}$-O-Fe^{2+}] (the sum of [$\equiv Fe$-O-Fe^{2+}] + [$\equiv Fe$-O-$FeOH^+$]) and [$\equiv Fe^{3+}$-OH] were estimated using surface complexation modeling (Visual Minteq). The $E_{h,surf}$ is calculated using the following Nernstian equation provided by Silvestre et al. (2005) and Li et al. (2019): [Insert Nernstian equation here].

$$E_{H,surface}\left(Fe^{II} - ferrihydrite\right) = 0.706 + 0.0592\log\frac{[\equiv Fe^{3+}-O-Fe(II)]}{[\equiv Fe^{3+}-OH]} - 0.118pH \qquad \text{eq. 2.7}$$

Using the given equation 2.7, we calculated the surface potential ($E_{h,surf}$) for the deoxygenated Fe-EC at 3.13 and 6.25 A/m^2, specifically for test #3 and #4. The calculation was performed only for the first 15 minutes, during which ferrihydrite is still present and not fully transformed. The adsorption of Fe(II) was determined using the observed concentration of Fe(II) at 15 minutes, as shown in Figure 2.4. We utilized the two-site complexation model of Dzombak and Morel from the Visual Minteq program simulation. The calculated values for $E_{h,surf}$ were -0.15 V and -0.18 V for the experiments conducted at 3.13 and 6.25 A/m^2, respectively. These values are more negative than the reduction potential of bulk ferrihydrite (-0.031 V) determined by Li et al. (2019). Thus, the $E_{h,surf}$ is sufficient to facilitate electron transfer to the underlying structural Fe(III) of ferrihydrite. This approach, which uses $E_{h,surf}$ as an indicator of the reduction potential of ferrihydrite, aligns with the results presented in Figure 2.3, confirming that the electrochemically generated Fe(II) drives the reductive transformation of ferrihydrite into goethite.

2.3.2. The formation and transformation of ferrihydrite during aerated Fe-EC

The ATR-FTIR spectra shown in Fig. 2.5A-C depict the phases of iron oxyhydroxides that are formed during the aerated Fe-EC experiments, which were not seeded and lasted for a duration of 120 minutes. These experiments were conducted at three different direct current densities: 6.25, 12.5, and 25.0 A/m^2 (exp. #3-5). The broad peaks observed at 580 and 690 cm^{-1}, corresponding to the bending vibration modes of ν(Fe-OH), indicate the formation of ferrihydrite as the initial phase within the first 30 minutes. The ATR-FTIR technique is not capable of distinguishing between the two known types of ferrihydrite, namely 2-line and 6-line, and therefore, the phase formed under these conditions is referred to simply as ferrihydrite. No traces of lepidocrocite, goethite, or magnetite were found in the FTIR spectra of the Fe-EC experiments conducted at 6.25 or 12.5 A/m^2. However, in the experiments conducted at 25 A/m^2, some lepidocrocite is already visible at 30 minutes, along with a smaller hump at 690 cm^{-1} indicating less ferrihydrite. Interestingly, when $FeSO_4$ was dosed at the same rate as in the Fe-EC experiments at 12.5 A/m^2 (see results in appendix 2B), the same ferrihydrite phase was formed as the initial phase. This demonstrates that ferrihydrite is the first phase to form during the oxidation of Fe(II) (eq. 1.3).

The broad vibrational bands at 900-1100 cm^{-1} (also visible in FTIR spectra of synthetic ferrihydrite in Fig. 2.3) are attributed to the vibration modes of adsorbed sulfate (SO_4^{2-}) ions on the ferrihydrite phases (Persson and Lovgren, 1996). No sulfate-containing schwertmannite ($Fe_8(OH)_6(SO_4) \cdot nH_2O$) shows sharp peaks at 840, 980, and a larger band at 700 cm^{-1} compared to 600 cm^{-1} (Wang et al., 2015). Instead, the presence of $Fe_2(SO_4)_3$ is observed (Whang et al., 2015; Zhang et al. (2021)). One noticeable observation is that these sulfate bands relative to ferrihydrite are approximately three times larger than the sulfate bands representing the adsorbed sulfate ions on preliminarily synthesized ferrihydrite. It should be noted that freshly formed ferrihydrite can have a higher specific surface area of 1000 m^2/g (Hiemstra et al., 2019) compared to a aged or preliminarily synthesized sample, and these large sulfate bands may well indicate the significant quantities of adsorbed sulfate ions on freshly formed ferrihydrite.
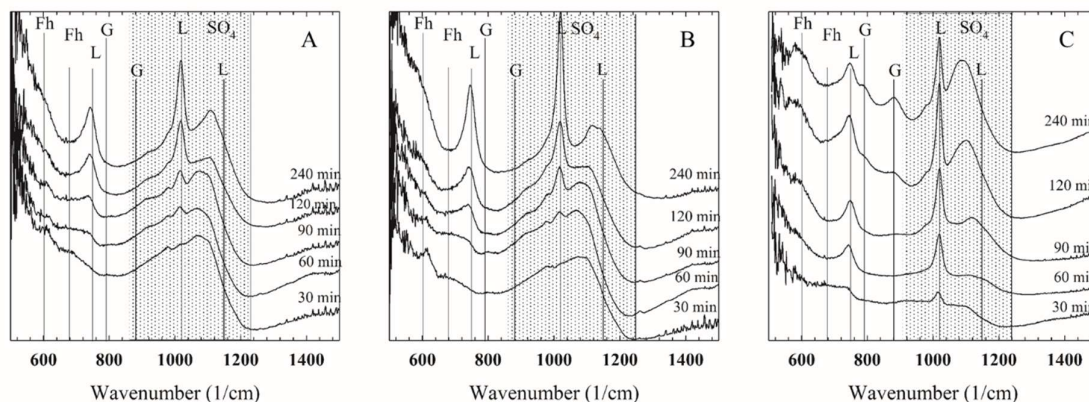
Fig. 2.5. *ATR-FTIR spectra ranging from 500-1500 cm^{-1} were obtained for the iron oxyhydroxides generated during the aerated Fe-EC experiment conducted at pH 7.0 and current densities (J) of 6.25, 12.5, and 25.0 A/m^2. A stirrer speed of 750 rpm was utilized, resulting in a highly oxygenated electrolyte. The vibration bands in the spectra were attributed to Fh (ferrihydrite), L (lepidocrocite), G (goethite), and SO$_4$ (sulfate), as detailed in Table 2.2 for reference.*

Initially, the ferrihydrite formed, observed up to 30 minutes, remains observable for up to 60 minutes at current densities of 6.25 and 12.5 A/m^2. Eventually, this ferrihydrite transforms into (1) lepidocrocite at current densities of 6.25 and 12.50 A/m^2 and (2) both lepidocrocite and goethite at a current density of 25.00 A/m^2 (Fig. 2.5). This transformation can be qualitatively traced in the ATR-FTIR spectra by the gradual emergence of peaks at 745, 1020, and 1115 cm^{-1} for lepidocrocite and 800 and 880 cm^{-1} for goethite, while the ferrihydrite bands at 690-710 cm^{-1} diminish (see Tab. 2.1). The newly formed stable phases likely dominate the rust phase, and crystal growth continues with the ongoing production of Fe(III) (according to equations 1.1 and 1.3). The same transformation to lepidocrocite and/or goethite has also been confirmed in studies involving FeSO$_4$ dosing and oxidation (Appendix 2A). It should be noted that the transformation rate was slower in the case of FeSO$_4$ dosing compared to the Fe-EC process. It is possible that the increase in local pH near the cathode accelerates the binding of Fe(II) to the forming ferrihydrite, as the local pH is higher than the pH$_{pzc}$ of ferrihydrite. Additionally, the change from a positively charged surface to a neutral one allows for more Fe(II) adsorption onto the ferrihydrite surface. This may contribute to increased transformation rates. However, this effect cannot be fully elucidated in the conducted Fe-EC experiments.

2.3.3. The [Fe(II)] levels and the relation to reductive transformation of ferrihydrite

The cell voltage, [Fe(II)], [O_2]$_{aq}$, and the [Fe(II)]$_{aq}$/[c(Fe(III))]$_{(s)}$ ratio are presented in Fig. 2.6 (A-D) for the 240-minute Fe-EC run at current densities of 6.25, 12.5, and 25.0 A/m^2. These data were used to assess whether ferrihydrite formation and its further transformation are caused by the catalytic role of Fe(II).

The cell voltage (Fig. 2.6A) remains constant throughout the entire 240 minutes of the Fe-EC run, with average cell voltages of 1.0, 1.1, and 1.3 V, respectively. Any increase in the cell voltage would indicate an increase in cell resistance due to passivation of the electrode by surface precipitates of non-conductive iron oxyhydroxide.

In the same setup carried out at pH 3.0 (to inhibit Fe(II) oxidation) and at a current density of 25.0 A/m^2, a slope of 1.95 was found between the charge loading and the [Fe(II)] (Fig. 2.2). This suggests that Fe(II) forms mainly through Fe(0) corrosion, with Fe(III) formation accounting for less than 2% of the current load.

All measured cell voltages are less than 1.48 V for O_2 evolution, indicating that O_2 evolution can largely be disregarded. These results demonstrate that stable and continuous Fe-EC operation is achieved when Fe(II) ions are predominantly formed through Fe(0) oxidation (in accordance with Lakshmanan et al. (2009)). This is likely because the electrochemically formed Fe(II) ions dissolve well in the electrolyte and do not precipitate on the anode surface, unlike the Fe(III)-ions.

The results in Fig. 2.6C show that [$O_{2(aq)}$] decreased from initially saturated conditions (8.2 mg/L; 0.26 mM) to almost complete depletion within 60 to 90 minutes at 12.5 and 25.0 A/m^2, and to 0.03 mM [O_2]$_{(aq)}$ at 6.25 A/m^2. The increase in [Fe(II)]$_T$ shown in Fig. 2.6B indicates that not all Fe(II) was oxidized, which is due to insufficient mixing at the applied stirrer speed of the electrolyte body, resulting in inadequate transfer of $O_{2(g)}$ →$O_{2(aq)}$. It was more challenging to sustain Fe(II) generation and oxidation at higher current densities (from 6.25 to 12.5 and 25.0 A/m^2), leading to a more pronounced increase in [Fe(II)]. At a transfer rate of 0.8 and 1.0 mg O_2 /min/L, 99%, 97%, and 83% of the total Fe(II) formed during the 240-minute electrolysis at 6.25, 12.5, and 25.0 A/m^2, respectively, was oxidized to Fe(III). The oxidation rates of Fe(II) for these Fe-EC tests are 40 times higher than the measured aqueous oxidation rate of Fe(II) in Morgan and Lahav (2007) and Chen and Thompson (2018). The difference here is that the Fe(II) oxidation leads to the formation of ferric oxyhydroxide, and these formed ferric oxyhydroxides (ferrihydrite, lepidocrocite, and goethite) act as catalysts for the oxidation of adsorbed Fe(II) (Barnes et al., (2009); Park and Dempsey, (2005)). This mechanism of the catalytic process may be related to the effect that drives the reductively catalyzed transformation of ferrihydrite: when Fe(II) is adsorbed to the surface of ferric

34

oxyhydroxides, it becomes a stronger reducer than aqueous Fe(II), as indicated by Silvestre et al. (2015) and Li et al. (2019), and oxidizes faster with $O_{2(aq)}$. With the continuous formation of ferrihydrite, lepidocrocite, or goethite throughout the Fe-EC run, the much faster heterogeneous oxidation of adsorbed Fe(II) dominates the overall oxidation of Fe(II) by $O_{2(aq)}$ (Tamura et al., (1976); Jeon and Dempsey, (2003); Barnes et al., (2009); Larese-Casanova, (2012)). The peak in $[Fe(II)_{(aq)}]/c(Fe(III))_{(s)}$ in Fig. 2.6D (at 30-60 min.) can be attributed to a shift from the slow oxidation of aqueous Fe(II) at the beginning of the Fe-EC to the gradually faster oxidation of Fe(II) through the heterogeneous oxidation pathway.
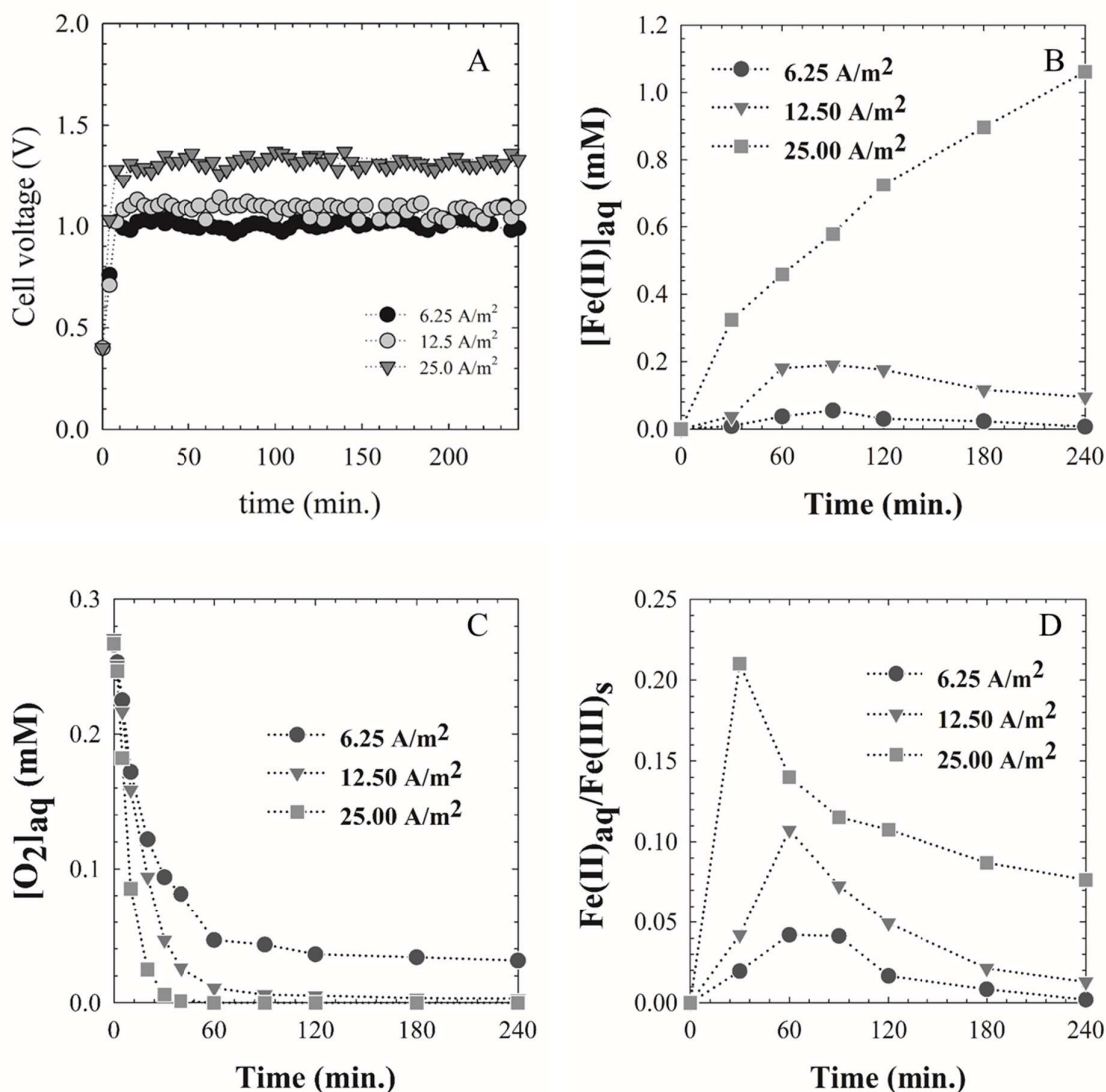
Fig. 2.6. *The A) cell voltage, B) [Fe(II)] C) [O$_{2(aq)}$], and D) molar Fe(II)$_{aq}$ to Fe(III)$_s$ ratio vs. time curves for the Fe-EC run at current densities of 6.25, 12.5, and 25.0 A/m^2 (experiments #3-#5 in Table 2.1) were analyzed. The experiments were conducted under open atmospheric conditions with a stirrer speed of 750 rpm, resulting in a highly oxygenated electrolyte. The pH was maintained at 7.0 throughout all three experiments.*

From the [Fe(II)], [O$_{2(aq)}$] (Figure 2.6 B and C), and ATR-FTIR data (Figure 2.5 A-C), it was assessed whether a catalytic process occurred and caused the rapid transformation of ferrihydrite during the Fe-EC reaction. A simplified way to express the potential for this electron transfer is to compare the electrolyte potential with the reduction potential of ferrihydrite, as studied by Yang et al. (2010) and Boland et al. (2013, 2014). However, in contrast to these previous studies, the experiments conducted in section 2.3.1 (exp. #1 and 2) were deoxygenated, and the recrystallization of ferrihydrite (Figure 2.5 A-C) occurred in the presence of both Fe(II) and O$_{2(aq)}$. To calculate the electrolyte potential (E$_{h,elec}$), the Nernst equation (eq. 2.5) was modified to include the E^0(O$_2$/H$_2$O) equation.

$$E_{h,elec} = (E^0_{Fe^{2+}/Fe^{3+}} + E^0_{O_2/H^+}) - 0.0592 \log \frac{\alpha(Fe^{2+})}{\alpha(H^+)\alpha(Fe^{3+})\alpha(O_2)^{0.25}} \qquad \text{eq. 2.7}$$

Using [Fe(II)] and [O$_{2(aq)}$] in Figure 2.6B and C for the aerated experiments at 6.25 and 12.5 A/m^2, we observed the point at which the formed ferrihydrite starts to transform into lepidocrocite. The calculated E$_{h,elec}$ is approximately +0.40 V and +0.31 V, respectively. It is important to consider that the ferrihydrite phase is in equilibrium with the apparent [Fe(II)] in Figure 2.6B, and Fe(II) is adsorbed to the ferrihydrite.

The reduction potential of ferrihydrite at the present [Fe(II)] (pH 7.0 and RT) is expected to vary between -0.05 V for low Fe(II) loading (10% surface coverage of ferrihydrite) and +0.05 V for high Fe(II) loading (90% surface coverage). This information was obtained from cyclic voltammetry in Li et al. (2019).

The ATR-FTIR results clearly depict the reductively catalyzed transformation of ferrihydrite to lepidocrocite in the range of 6.25-25 A/m^2, despite the more oxic prevailing E$_{h,elec}$ (ΔE = +0.25-0.30V). However, there is still a missing link in our understanding. It is possible that the adsorption of Fe(II) to the forming ferrihydrite and the subsequent electron transfer occur at a much faster rate than the heterogeneous oxidation of Fe(II) on the surface of ferrihydrite (Jeon and Dempsey, 2003).

For example, previous works by Jeon and Dempsey (2003) and Sheng et al. (2020a) have indicated rapid adsorption of Fe(II) by ferrihydrite upon mixing them together. This suggests that there is a net accumulation of unoxidized Fe(II) on the surface of ferrihydrite, creating an $E_{h,surf}$ that is separate from the $E_{h,elec}$ but more reduced than the reduction potential of ferrihydrite. This $E_{h,surf}$ drives the reductively catalyzed transformation of ferrihydrite.

For the three current densities studied here, the average rate of Fe(III) production (after subtracting the dissolved Fe(II) in Fig. 2.6B from the total electrochemically generated Fe(II)) is 0.26-1.04 μM/s at a current density (J) of 6.25-25 A/m^2. Considering the solubility of ferrihydrite at pH 7.0 ($K_{sp} = 10^{-37.5}$ M^4), such a production rate of Fe(III) indicates a constant and significant driving force for Fe(III) precipitation (Dousma and DeBruyn, (1976); Dousma et al. (1979); Flynn (1984); Dutrizac (1987)). The ATR-FTIR data obtained from the Fe-EC test (Fig. 2.5) and the FeSO₄ oxidation tests (Appendix 2A) support our findings that rapid precipitation leads to ferrihydrite formation and follows Ostwald's stages (Blesa and Matijevic 1989). As long as the solution remains supersaturated with respect to ferrihydrite, solvent-mediated recrystallization does not occur. This explains the observed inhibition of lepidocrocite or goethite formation and the preference for ferrihydrite formation, which remains relatively stable for the first 30 to 60 minutes. These findings raise the question of whether the direct formation of goethite or lepidocrocite from the oxidation of Fe(II) (Fe^{2+}_{aq}, $Fe(OH)^+_{aq}$, and $Fe(OH)_{2(s)}$) as reported by Oh et al. (2001) and Chen and Thompson (2021) might actually involve fast initial ferrihydrite formation followed by an instantaneous reductive transformation of this formed ferrihydrite into the more stable goethite or lepidocrocite. The experiments conducted in the FeSO₄ oxidation (Appendix 2A) and the Fe-EC experiments at 6.25 and 12.5 A/m^2 (Fig. 2.5A+B) confirm this hypothesis. One possible explanation for the absence of ferrihydrite in Fe(II) oxidation studies may be related to the method employed for the oxidation. In those studies, a starting concentration $[Fe(II)]_0$ (1 mM FeSO₄ in Chen and Thompson (2020)) is typically oxidized at pH 7.0 under buffered conditions by introducing $O_{2(aq)}$ to the solution. Even the slightest oxidation of the Fe(II) ions results in a very high $Fe(II)_{aq}/Fe(III)_s$ ratio (Fig. 2.6D), for example, the $Fe(II)_{aq}/Fe(III)_s$ ratio reaches 9 when 10% of the total [Fe(II)] is oxidized. Any ferrihydrite that forms in these experiments (as $Fe(III)_s$) undergoes unnoticed reductive transformation to lepidocrocite and/or goethite due to the abundance of dissolved Fe(II) ions. In the EC experiments conducted at 6.25-25 A/m^2, the electrochemically produced Fe(II) is directly oxidized by continuous O₂ supply to the electrolyte, resulting in a $Fe(II)_{aq}/Fe(III)_s$ ratio at the moment of ferrihydrite formation (at t = 30 min) that is < 0.2 (See Fig. 2.6D). Hence, this ratio is approximately 45 times lower than

the first 10% Fe(II) oxidation carried out by Chen and Thompson (2020). Consequently, ferrihydrite can persist for longer periods in aerated Fe-EC cells compared to direct oxidation of Fe(II).

2.3.4. Increasing the ferrihydrite production by seeding and aeration

Fig. 2.7(A-C) shows the ATR-FTIR data of the rust phase composition carried by Fe-EC run in synthetic ferrihydrite with a starting concentration of 208 mg Fe(III)/L (3.58 mM), 417 mg Fe(III)/L (7.14 mM), and 834 mg Fe(III)/L (14.28 mM). By using Faraday's Law (eq. 2.8) and a current efficiency of 98% (see Fig. 2.2), it can be calculated that a maximum concentration of Fe(III) of 417 mg Fe(II)/L (7.46 mM) is produced during the 240-minute experimental period at a current density of 12.5 A/m^2 and a stirrer speed of 750 rpm. Running Fe-EC for 240 minutes under fast oxygenated conditions (stirring speed of 750 rpm) in the presence of 208 mg Fe(III)/L (c(Fe(III))$_{Fh}$ = 3.58 mM), representing half of the total produced by the Fe-EC process, reduces the overall transformation rate of ferrihydrite into lepidocrocite and goethite significantly (see Fig. 2.7B for comparable current density, but under deoxygenated conditions, and compare with Fig. 2.5B experiment without seeds). This is evident from the weak appearance of the vibration bands of goethite at 800 and 880 cm^{-1} and the virtual absence of lepidocrocite-specific bands at 749, 1020, and 1115 cm^{-1} (bending vibration of Fe-OH) in the ATR-FTIR spectra, compared to the large vibration bands of synthetic ferrihydrite at 580 and 690 cm^{-1}. Adding 417 mg Fe(III)/L (c(Fe(III))$_{Fh}$ = 7.16 mM) in the form of ferrihydrite seeds further reduces the transformation of ferrihydrite, and adding 834 mg Fe(III)/L of (c(Fe(III))$_{Fh}$ = 14.32 mM) almost completely stops the transformation of ferrihydrite, with only weak observable bands of goethite (Fig. 2.7C). Based on a rough peak height estimation, adding seeds of ferrihydrite of 208, 417, and 834 mg Fe(III)/L allows for the production of 50%, 70%, and 80% more ferrihydrite than in unseeded experiments. The accumulation of Fe(II) in the electrolyte in the presence of synthetic ferrihydrite was not detected, indicating that [Fe(II)] was < 0.1 μM according to the UV-VIS method. The possibility that Fe(II)-ions would accumulate in the ferrihydrite phase if ferrihydrite was not added (Fig. 2.6B) is unlikely, as in that case, a reductively catalyzed transformation of the ferrihydrite into goethite or lepidocrocite would be expected. Therefore, the poor reductively catalyzed transformation of ferrihydrite means that the electrochemically generated Fe(II) ions were largely oxidized. Since ferrihydrite seeds are present at the onset of the Fe-EC experiment and act as catalysts for Fe(II) oxidation by adsorbing the Fe(II) and enabling this adsorbed Fe(II) to become a much stronger reducer than the aqueous one(s), the fast heterogeneous

38

oxidation of surface-associated Fe(II) catalyzed by the ferrihydrite seeds and the ferrihydrite formed upon (Tamura et al., (1976); Barnes et al., (2009); Larese-Casanova, (2012)) prevails. Additionally, the presence of ferrihydrite seeds prevents the accumulation of Fe(II) onto the surface of ferrihydrite, which reduces the development of a reduced $E_{h,surf}$ to reduce structural Fe(III) of ferrihydrite, thereby reducing the reductively catalyzed transformation of ferrihydrite to lepidocrocite and/or goethite. Consequently, adding seeds of ferrihydrite is a suitable method to produce a higher amount of ferrihydrite compared to Fe-EC without the presence of ferrihydrite at the onset.
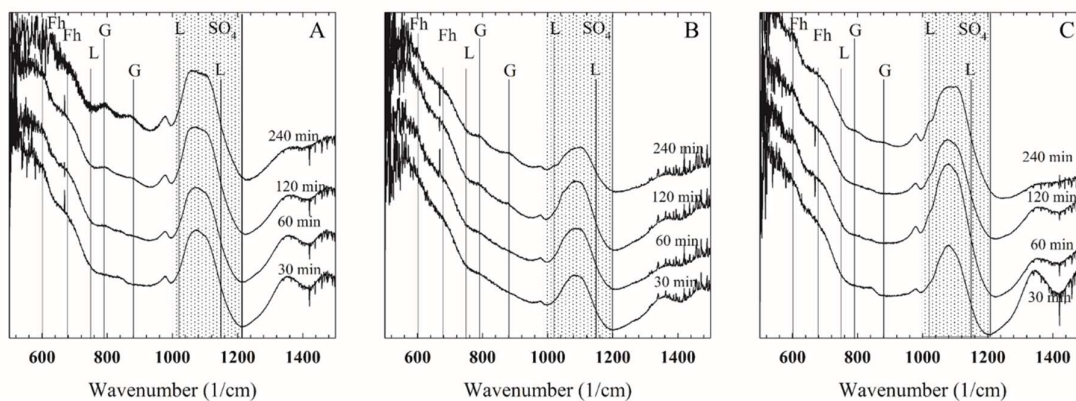

Fig. 2.7. *ATR-FTIR analysis was conducted on the rust phase obtained after a 120-minute Fe-EC run (aeration by stirring) at a current density of 12.5 A/m^2 in a suspension containing synthetic ferrihydrite seeds at concentrations of 200 mg/l on the left, 400 mg/l in the middle, and 800 mg/l on the right. The identification key for the detected phases is as follows: F represents Ferrihydrite, L represents Lepidocrocite, and G represents Goethite. The shaded area in the spectra corresponds to the prominent vibration bands of adsorbed SO$_4^{2-}$ ions.*

2.3.5. Discussion on the lepidocrocite vs. goethite formation from the Fe(II)-induced ferrihydrite recrystallization

The studies conducted by Liu et al. (2007), Hansel et al. (2005) and Boland et al. (2014) were the first to describe the phenomenon where an excess of [Fe(II)] over $c(Fe(III))_{Fh}$ leads to the formation of goethite (>0.5-1.0) instead of lepidocrocite (<0.2). In our experiments, the synthetic ferrihydrite recrystallized to goethite regardless of the ratio of [Fe(II)] to $c(Fe(III))_{Fh}$. This was observed at a ratio of 0.5 in exp. #1 and #2 (conducted under deoxygenated conditions) and at a very low ratio (<0.001) in exp. #6-#8. However, *in-situ* formed ferrihydrite explicitly transformed into lepidocrocite and not goethite at a ratio of [Fe(II)] to $c(Fe(III))_{Fh}$ of

0.05-0.10 (exp. #3 and #4, Fig. 2.6D at 30 min.). The difference is that the *in-situ* formed ferrihydrite is freshly generated and likely has a highly hydrated structure with loosely bound OH-groups before transforming into lepidocrocite. On the other hand, the synthetic ferrihydrite (exp. #1-#2 and #6-#8) is aged for one week prior to its use in the Fe-EC tests. Therefore, it possesses a higher degree of crystalline order, which is reflected in more distinct 2-Line features in XRD measurements (Liu et al., (2023)). The crystalline order of ferrihydrite affects the phase formed through reductive dissolution and precipitation of labile Fe(III), as demonstrated by Liu et al. (2023). They found that ferrihydrite produced by rapid hydrolysis within 2 hours predominantly transformed into lepidocrocite, while slowly hydrolyzed and less crystalline ferrihydrite (produced in 12 hours by slow NaOH addition) transformed into goethite (Liu et al., (2023)). The authors attribute the formation of lepidocrocite to the higher concentration of labile Fe(III), consisting of Fe(III) and small Fe(III)-oligomers, in the less crystalline phase. This phase exhibits higher activity and leads to a relatively higher supersaturation, which surpasses the nucleation barrier for both lepidocrocite and goethite. Under highly supersaturated conditions, the least stable phase, which is lepidocrocite, is favored (note: the driving force remains the same, but the intermediate could accelerate the conversion). Nonetheless, the labile Fe(III) concentration typically measured in the process of transformation, ranging from 0.1 to 0.4 mM, remains highly supersaturated with respect to all three phases (ferrihydrite, lepidocrocite, and goethite), indicating that the least stable phase, ferrihydrite, is expected to prevail. There is further evidence that the nuclei of secondary phases develop (Latta et al., (2023); Notini et al., (2022)) after local restructuring of the ferrihydrite phase upon the formation of a pool of labile Fe(III). During the early stage of electron transfer (referred to as the lag-time), where a high quantity of Fe(II) is adsorbed to ferrihydrite but no transformation to lepidocrocite or goethite is observed yet, a magnetically ordered structure resembling proto-lepidocrocite forms. This proto-lepidocrocite may act as a potential precursor for the subsequent dominance of lepidocrocite and/or goethite nuclei. However, due to the complexity of reactions occurring at the surface upon Fe(II) adsorption to ferrihydrite, our understanding of how electron transfer and labile Fe(III) formation influence the rates and extents of olation and oxolation (polymerization of Fe(III) to form O-Fe-O, see Cudennec and Lecerf, 2006) and result in the distinct structures of lepidocrocite or goethite remains rudimentary.

A more thermodynamic approach is to relate the reduction potential of ferrihydrite (+0.05-0.03V), lepidocrocite (-0.05V), and goethite (-0.2V) to the prevailing surface potential, i.e., $E_{h,surf}$, at the Fe(II)-ferrihydrite interface. Essentially, ferrihydrite is prone to transform into

lepidocrocite through reductive dissolution when the $E_{h,surf}$ exceeds the reduction potential of ferrihydrite but remains above the reduction potential of lepidocrocite. Similarly, goethite is likely to form when the $E_{h,surf}$ is lower than the reduction potential of both ferrihydrite and lepidocrocite. When assessing the $E_{h,surf}$ (using eq. 2.7), it is important to consider that the pH of the point of zero charge (pH_{pzc}) varies with the crystallinity of ferrihydrite. Very freshly formed ferrihydrite, which forms through rapid hydrolysis, undergoes a low dehydroxylation rate, resulting in a high pH_{pzc} of around 8.7-8.8. This high pH_{pzc} leads to the adsorption of large quantities of anions such as phosphate. Ferrihydrite that forms within the first 30 minutes of the aerated Fe-EC test is considered freshly formed, with an estimated surface area (A_s) of approximately 600 m^2/g. The synthetic ferrihydrite seeds used in the anaerobic and aerobic tests were aged for 1 week before testing and thus are presumed to have a pH_{pzc} of 8.1 and a generally lower A_s of 250 m^2/g. In the aerated Fe-EC test, the concentration of $Fe(III)_{Fh}$ reaches around 50 mg Fe(III)/L within the first 30 minutes at 6.25 and 12.5 A/m^2. In tests with synthetic ferrihydrite, concentrations of 200 mg (Fe(III)/L) or higher (400 and 800 mg Fe(III)/L) were used. These concentrations, along with the estimated A_s values and different pH_{pzc} values, were used in eq. 2.7 to calculate the $E_{h,surf}$ for the unseeded and deoxygenated Fe-EC tests. Figure 2.8 illustrates the relationship between $E_{h,surf}$ and the Fe(II)-loading, expressed as the [≡Fe-O-Fe(II)] / [≡Fe-OH] ratio. The reduction potentials of the four phases (ferrihydrite, lepidocrocite, goethite, and magnetite) are represented by different characteristic colors. These limits are not precisely defined, as the reduction potentials can vary by around ±0.05V. The relation between $E_{h,surf}$ and Fe(II)-loading shows that even at low Fe(II)-loadings, the $E_{h,surf}$ decreases below the reduction potential of ferrihydrite, initiating the reductively catalyzed transformation by oxidizing the surface-adsorbed Fe(II) to Fe(III) and forming labile Fe(III) upon detachment through oxidation. For freshly formed ferrihydrite, the $E_{h,surf}$ falls within the electrochemical stability region of lepidocrocite due to a relatively lower Fe(II)-loading per exposed ≡Fe-OH group, consistent with the ferrihydrite to lepidocrocite transformation observed in Figure 2.5. Aged ferrihydrite reaches more reduced conditions on the $E_{h,surf}$ due to a higher [≡Fe-O-Fe(II)] / [≡Fe-OH] ratio, which is sufficient for goethite formation as both lepidocrocite and ferrihydrite undergo reductive dissolution under these conditions. Even in the aerated tests with seeds, where Fe(II)-adsorption is much smaller, the $E_{h,surf}$ matches with the stability region of goethite due to the relatively higher [≡Fe-O-Fe(II)] / [≡Fe-OH] ratio. Therefore, this initial simplified relation not only provides an explanation for why ferrihydrite is susceptible to reductively catalyzed transformation, but also suggests that lepidocrocite or goethite nuclei may develop on the surface of ferrihydrite depending on the prevailing $E_{h,surf}$ upon Fe(II)

adsorption. Although electrolyte asymmetry and sulfate surface adsorption likely affect Fe(II) adsorption and pH_{pzc}, and that sulfate adsorption can mask the available $\equiv$Fe-OH-groups, these independent factors have not been included in the assessment of $E_{h,surf}$ and therefore remain rudimentary.

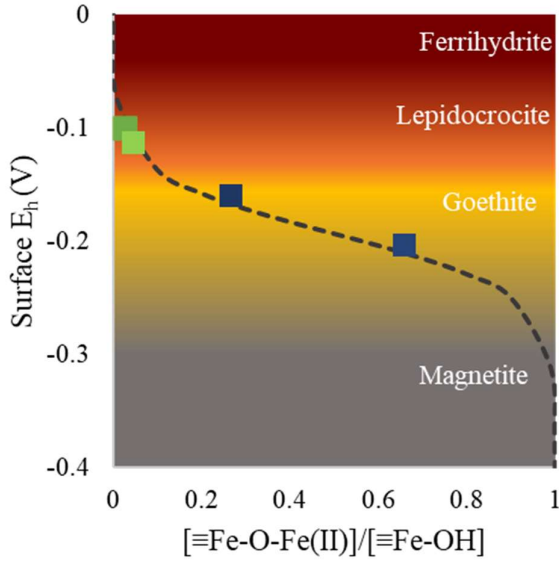**Fig. 2.8.** *The $E_{h,surf}$ (surface oxidation-reduction potential) is influenced by the presence of adsorbed Fe(II), specifically [$\equiv$Fe-O-Fe(II)] ([$\equiv$Fe-O-Fe(OH)^0] + [$\equiv$Fe-O-Fe+]), in contrast to non-complexed [$\equiv$Fe-OH] ([$\equiv$Fe-O-] + [$\equiv$Fe-OH)] + [$\equiv$Fe-OH$_2^+$]). The reduction potentials of ferrihydrite (+0.05 V), lepidocrocite (-0.05 V), goethite (-0.2 V), and magnetite (-0.30 V) are further depicted using shaded colors that represent the typical observed color of these phases. The $E_{h,surf}$ was calculated for both the freshly formed ferrihydrite during the aerated Fe-EC experiment (in experiments #3 and #4) and the aged synthetic ferrihydrite used in experiments #6 and #7 (as* shown in *Table 2.1).*

As shown in Figure 2.8, the $E_{h,surf}$ does not achieve the reduction potential of magnetite. This indicates that the loading of Fe(II) onto ferrihydrite is insufficient to reach the reduction potential required for the reductive dissolution and transformation of ferrihydrite and lepidocrocite into goethite. It is likely that increasing the pH above the pH_{pzc} of fresh or aged ferrihydrite (8.8 vs. 8.1) could potentially raise the [$\equiv$Fe-O-Fe(II)] / [$\equiv$Fe-OH] ratio and reach the reduction potential of magnetite, as magnetite is often observed at pH > 7. Furthermore, increasing the [Fe(II)] to a much higher level could enhance Fe(II) loading onto ferrihydrite and favor the formation of magnetite over lepidocrocite and goethite.

2.3.6. Effect of varying the O₂ supply on unseeded ferrihydrite formation in Fe-EC

The hypothesis that rapid oxidation of the electrochemically generated Fe(II) leads to the formation of stable ferrihydrite is being investigated under various oxygenated conditions. This is done by varying the stirrer speed of the electrolyte during a constant and unseeded Fe-EC run at 25 A/m^2. In comparison to the previous test conducted at a stirrer speed of 750 rpm, which corresponds to high oxygenation, additional tests were performed by increasing the supply of $O_{2(aq)}$ to the electrolyte through aeration and vigorous stirring (at 1000 rpm), and in the presence of H_2O_2 (1 wt% of 300 g H_2O, 526 mM $[H_2O_2]_T$). Further tests were conducted at 250 rpm (slow) and 500 rpm (moderate) to investigate the influence of different oxidation rates on ferrihydrite productivity.
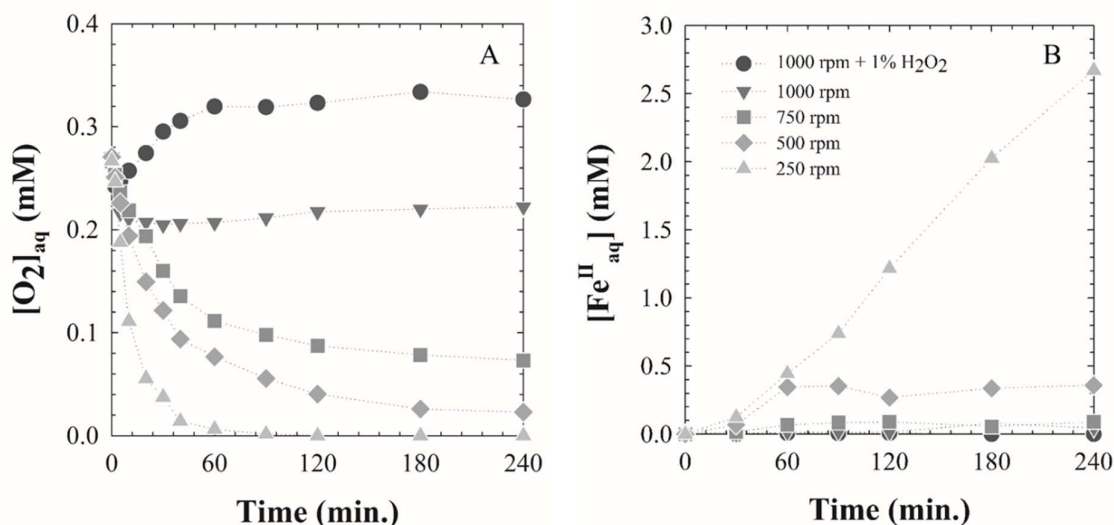

Fig. 2.9. *The effect of oxygenation levels on the concentration of dissolved oxygen ([O₂(aq)]) and ferrous iron ions ([Fe(II)aq]) was investigated during a 240-minute Fe-EC experiment carried out at a current density of 25 A/m² and pH 7.0. The oxygenation levels were manipulated by adding 1% hydrogen peroxide (H₂O₂) and vigorously stirring the solution at different speeds: maximum oxygenation at 1000 rpm, fast oxygenation at 750 rpm, moderate oxygenation at 500 rpm, and slow oxygenation at 250 rpm. The resulting rust phase compositions were analyzed using ATR-FTIR spectroscopy, and the corresponding spectra are presented in Figure 2.10.*

Fig. 2.9A and B show a clear relationship between the $[O_{2(aq)}]$ during the tests and the evolution of [Fe(II)]. Under conditions of vigorous mixing (1000 rpm), the $[O_{2(aq)}]$ remained saturated throughout the 240 minutes of Fe-EC (~8 mg/L, 0.25 mM). In the presence of H_2O_2,

the $[O_{2(aq)}]$ even increased to ~10 mg/L (0.33 mM). This occurs due to O_2 evolution by the following reaction: $2Fe^{2+} + 2H_2O_2 \rightarrow 2Fe^{3+} + 2H_2O + O_2$. In both tests, no [Fe(II)] was detected. When oxygenation was decreased by using lower stirrer speeds of 750, 500, and 250 rpm, the $[O_{2(aq)}]$ sharply decreased, with the decrease being faster at lower stirrer speeds. Consequently, $[Fe(II)_{aq}]$ initially increased at stirring speeds of 500 and 750 rpm but then remained fairly constant (Fig. 2.9B). At the poorest oxygenation, i.e., a stirrer speed of 250 rpm (low mixing rate), [Fe(II)] continued to increase to 2.5 mM, indicating that 17% of the electrochemically generated Fe(II) was not oxidized to Fe(III).

Fig. 2.10 displays the ATR-FTIR data of the final rust phase obtained after a 240-minute Fe-EC run at 25 A/m². When running the Fe-EC process in a 1% H_2O_2 solution, it only results in the production of ferrihydrite, as indicated by the prominent peaks observed at 600 and 690 cm^{-1}. However, when a saturated $O_{2(aq)}$ environment is provided by vigorously stirring the electrolyte and introducing aeration (by bubbling air through the electrolyte) during the Fe-EC tests, it predominantly leads to the formation of ferrihydrite with a smaller proportion of lepidocrocite. Managing to solely form ferrihydrite is challenging, despite the presence of detectable levels of [Fe(II)]. Hence, it is likely that Fe(II) adsorption occurs, and electron transfer drives a portion of the formed ferrihydrite towards lepidocrocite. This phenomenon becomes more evident at stirring speeds of 750 and 500 rpm, where a decrease in $[O_2]$ results in an increase in [Fe(II)] and a greater formation of lepidocrocite (at 745 and 1020 cm^{-1}) compared to ferrihydrite, indicating an enhanced transformation of the initially formed ferrihydrite. At the lowest oxygenation level (250 rpm), both goethite and lepidocrocite form (Fig. 2.10). In this case, similar to test #5 conducted at 25 A/m², goethite forms through the recrystallization of lepidocrocite induced by Fe(II) (Sheng et al., (2022)). The XRD data presented in appendix 2B confirms the formation range of these phases.
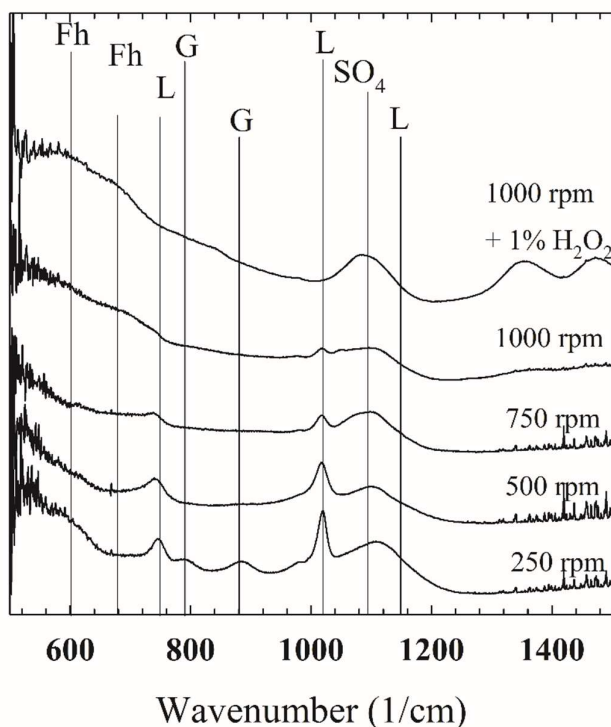
Fig. 2.10. *ATR-FTIR spectra of the corrosion products obtained after 240 minutes at a current density of 25 A/m² and pH 7.0 using different stirrer speeds, categorized in the following order of oxygenation:* **250 rpm** *(poorly oxygenated),* **500** *rpm (moderately oxygenated),* **750** *rpm (highly oxygenated),* **1000** *rpm (fully saturated $O_{2(aq)}$)), and* **1000 rpm + 1% H_2O_2** *(high oxidative conditions).*

The mere production of ferrihydrite in the presence of H_2O_2 indicates that very high oxidation rates are required to increase the production of ferrihydrite by Fe-EC. Even when operating at 1000 rpm with aeration (Fig. 2.10), where the accumulation of Fe(II) ions is below the detection limit (< 1.8 μM), it was not possible to produce ferrihydrite alone. The rate at which Fe(II) accumulates on ferrihydrite is very rapid, as evidenced by earlier experiments with ferrihydrite seeds, where [Fe(II)] was not detectable in the electrolyte. Based on the estimation from the seeded test, Fe(II) accumulates onto ferrihydrite at a rate 20 times faster than the oxidation rate of Fe(II) at pH 7.0 and saturated [$O_{2(aq)}$] (~0.07 mM/min in Morgan and Lahav, 2007). In that case, heterogeneous oxidation of Fe(II) by ferrihydrite can occur from the beginning and maintain low levels of Fe(II) accumulation in the electrolyte, ensuring the stability of ferrihydrite. In the test carried out in this section, no ferrihydrite seeds were initially added. Consequently, the amount of ferrihydrite is insufficient to sustain a high heterogeneous oxidation of Fe(II), causing Fe(II) to accumulate faster on the forming ferrihydrite than it can

be oxidized by $O_{2(aq)}$. This rapid uptake of Fe(II) by ferrihydrite leads to a sharp decrease in surface E_h, reaching the reduction potential of ferrihydrite, i.e., < 0.05 V, and causing a fast reductive transformation of ferrihydrite to lepidocrocite (Li et al., 2019). Only by rapidly oxidizing the Fe(II) ($[Fe(II)]_T$ = 14.9 mM) using an excess of highly oxidative H_2O_2 (1 V%, $E^0(H_2O_2/H_2O)$ = 1.77 V) with a maximum $[O_{2(aq)}]$ of 0.25 mM at room temperature, it is possible to overcome Fe(II) accumulation on the forming ferrihydrite and delay the reductive transformation of the forming ferrihydrite by maintaining a highly oxygenated surface Eh with H_2O_2 (See $[O_{2(aq)}]$ in Fig. 2.10B). As shown in Fig. 2.10, such highly oxidative conditions enable the formation of ferrihydrite throughout the entire 120-minute Fe-EC run.

Aeration (Figure 2.10), where the concentration of Fe(II) ions is below the detection limit (< 1.8 µM), does not allow for the exclusive production of ferrihydrite. The rate at which Fe(II) accumulates on ferrihydrite is very fast (i.e., 0.14 mM/min), as inferred from previous experiments with ferrihydrite seeds, where no detectable [Fe(II)] was found in the electrolyte. Based on the estimation from the seeded test, the rate of Fe(II) accumulation on ferrihydrite is 20 times faster than the oxidation rate of Fe(II) at pH 7.0 and saturated [O2(aq)] (~0.07 mM/min in Morgan and Lahav, 2007). In this case, the heterogeneous oxidation of Fe(II) by ferrihydrite can occur from the beginning and maintain low levels of Fe(II) accumulation in the electrolyte, as well as on the ferrihydrite surface, ensuring the stability of ferrihydrite. In the test performed in this section, no ferrihydrite seeds were initially added. Consequently, the amount of ferrihydrite is low, which leads to a high heterogeneous oxidation of Fe(II), resulting in the rapid accumulation of Fe(II) on the forming ferrihydrite, faster than its oxidation by $O_{2(aq)}$. This rapid uptake of Fe(II) by ferrihydrite causes a significant decrease in surface $E_{h,surf}$, likely reaching the reduction potential of ferrihydrite, i.e., < 0.05 V, and causing a rapid reductive transformation of ferrihydrite to lepidocrocite (Li et al., 2019). Only through the fast oxidation of Fe(II) ($[Fe(II)]_T$ = 14.9 mM) with an excess of highly oxidative H_2O_2 (1 V%, $E^0(H_2O_2/H2O)$ = 1.77 V), i.e., 789 mM compared to a maximum $[O_{2(aq)}]$ of 0.25 mM at room temperature, is it possible to overcome the accumulation of Fe(II) on the forming ferrihydrite and delay the reductive transformation of the forming ferrihydrite by maintaining a highly oxygenated surface Eh with H_2O_2 (See $[O_{2(aq)}]$ in Figure 2.10B). As depicted in Figure 2.10, such highly oxidative conditions facilitate the formation of ferrihydrite throughout the entire 120-minute duration of the Fe-EC run.

2.3.7. Removal of PO₄ with rust phases produced in unseeded batch experiments at various stirring speeds

To investigate the adsorption capacity of the rust phases formed under different levels of oxygenation, as mentioned in section 2.4.3, the final suspensions were collected and utilized for PO₄ adsorption experiments. The adsorption experiments involved adding Na_2HPO_4 to the slurry suspension to achieve a $[PO_4]_T$ of 2.0 mg/l (0.021 mM) and continuously monitoring the reduction in $[PO_4]_T$ while maintaining a pH of 7.0. The decreasing $[PO_4]_T$ are illustrated in Figure 2.11. It is evident that rust phases with higher amounts of ferrihydrite (refer to Figure 2.9) exhibit greater efficiency in removing PO₄ (>99%).
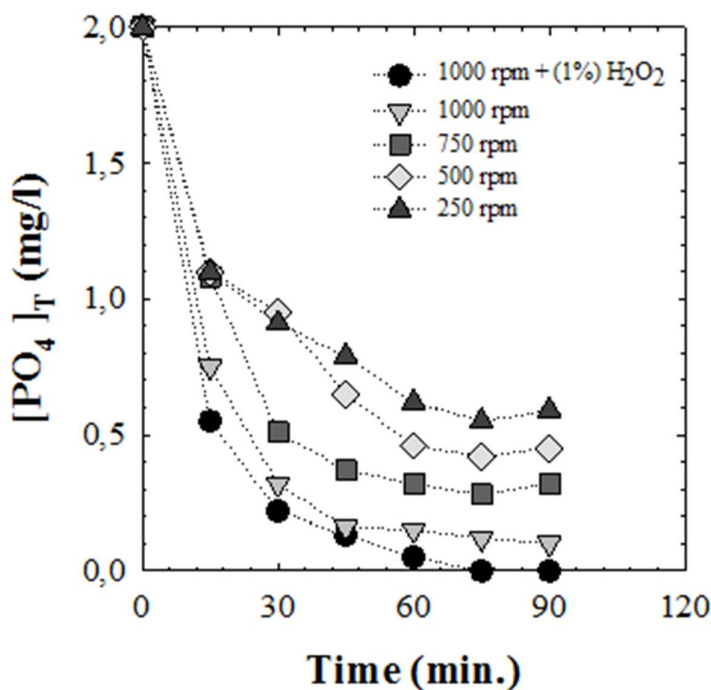

Fig. 2.11. *PO₄ adsorption experiments were conducted using iron oxyhydroxides that were first produced by running a Fe-EC (electrocoagulation) process at 25 A/m² for 120 minutes. The electrolyte's oxygenation was varied by adjusting the stirrer speed to 250 (low oxygenation), 500 (moderate oxygenation), 750 (fast oxygenation), and 1000 rpm (maximum oxygenation). Additionally, a separate experiment was conducted with the stirrer speed set at 1000 rpm in the presence of 1 V% H₂O₂. The pH during the production of iron oxyhydroxides and the subsequent adsorption tests was maintained at 7.0. Prior to initiating the adsorption experiments, any remaining Fe(II)-ions were oxidized to Fe(III) using air to eliminate potential competition from Fe(II) adsorption on the iron oxyhydroxide surface. Refer*

to Figure 2.10 for the composition of the rust. Throughout the 120-minute adsorption period, the pH was kept constant after the addition of PO$_4$.

The difference in adsorption capacity between these phases can be attributed to the following factors: (1) the number of [≡Fe-OH] groups on the surface to which PO$_4$ binds and (2) the acidity of these groups. The specific surface area of ferrihydrite typically ranges between 250-1100 m^2/g, which is higher compared to lepidocrocite (80-150 m^2/g) and goethite (15-60 m^2/g). For a 120-minute aged ferrihydrite, the adsorption surface area is estimated to be around 350-400 m^2/g for As. Furthermore, the density of ≡Fe-OH/m^2 is higher for ferrihydrite (up to 6.0 ≡Fe-OH/nm^2) compared to lepidocrocite (2.1 ≡Fe-OH/nm^2) and goethite (1.9 ≡Fe-OH/nm^2) (Cornell and Schwertmann, (2003)). Additionally, ferrihydrite has a higher pH$_{pzc}$ of 8.1 (which may be lower due to SO$_4^{2-}$ adsorption and subsequent shift to lower pH$_{pzc}$) compared to lepidocrocite (5.9) and goethite (6.1) (Zhong et al., (2022)). This indicates that ferrihydrite has a higher concentration of ≡Fe-OH$_2^+$ (as indicated by the equilibrium reaction: ≡Fe-OH$_2^+$ (≡FeOH + H$^+$) at pH 7.0 and RT), making it more conducive to the adsorption of negatively charged H$_2$PO$_4^-$ (the dominant form). Overall, this results in a 5 to 10 times higher adsorption capacity of ferrihydrite, enabling the removal of PO$_4$ to [PO$_4$]$_T$ < 0.1 μM.

2.4. Conclusion

This study showcases the formation of ferrihydrite and its stability in Fe-EC process applications. The Fe-EC run, conducted in a deoxygenated electrolyte with synthetic ferrihydrite (200 mg or 3.58 mmol Fe/L) at pH 7.0, produces Fe(II) ions that drive the reductively catalyzed transformation of ferrihydrite into the more stable goethite. As the current densities increase from 3.13 to 6.25 A/m^2, a higher amount of Fe(II) is generated, resulting in an increased fraction of goethite in the rust phase compared to the initial synthetic ferrihydrite. However, despite the [Fe(II)]/c(Fe(III)$_{Fh}$) ratio reaching 0.2, no magnetite is observed, which contradicts expectations based on thermodynamic solubility data. Nevertheless, the transformation rate of ferrihydrite to goethite is kinetically faster than the formation of magnetite, leading to the dominance of goethite formation over magnetite formation.

In aerated, yet unseeded, Fe-EC experiments, ferrihydrite was the first phase to form through the *in-situ* oxidation of the electrochemically generated Fe(II) ions, ruling out the formation of lepidocrocite as a mere phase resulting from Fe(II) oxidation. After approximately 30-60 minutes of continuous Fe-EC operation, the supply of O$_{2(aq)}$ became limited, leading to

an increase in [Fe(II)] and a rapid reduction of the formed ferrihydrite. With higher applied current densities (6.25, 12.5 to 25 A/cm^2), the limitation in the supply rate of O2(aq)- increased accordingly, and the formation of ferrihydrite from Fe(II) oxidation was further restricted due to its quick catalytic transformation into lepidocrocite. At 25 A/cm^2, a secondary transformation of lepidocrocite into goethite was observed, catalyzed by Fe(II). Furthermore, a relationship was observed between the $E_{h,surf}$ and the reduction potential of ferrihydrite, lepidocrocite, and goethite.

In seeded Fe-EC experiments using synthetic ferrihydrite (200 (3.58 mmol), 400 (7.16 mmol), and 800 mg (14.32 mmol) Fe/L), only small amounts of goethite were formed with the lowest amount of seeds (200 mg (3.58 mmol) Fe(III)/L), and overall ferrihydrite transformation was significantly hindered by the rapid removal of electrochemically generated Fe(II) from the electrolyte. This removal was mainly attributed to the prevailing heterogeneous oxidation rates of Fe(II) in the presence of ferrihydrite seeds. Therefore, adding ferrihydrite seeds is an effective method to enhance the net production of ferrihydrite with the Fe-EC process.

In unseeded Fe-EC tests at 12.5 A/m^2, with vigorous stirring and saturation of $O_{2(aq)}$ to maximize Fe(II) oxidation, ferrihydrite could not be exclusively produced, and lepidocrocite co-formed through the partial transformation of in-situ formed ferrihydrite. Only in the presence of excessive amounts of strong oxidants like H_2O_2 (789 mM vs. maximum $[O_{2(aq)}]$ of 0.25 mM under full saturation) was it possible to produce pure ferrihydrite through the Fe-EC process. This indicates the difficulty in producing ferrihydrite, primarily due to the rapid onset of electron transfer reactions between adsorbed Fe(II) and ferrihydrite, even when [Fe(II)] was below the detection limit of 1.8 μM $[Fe(II)]_T$. Lower oxygenation conditions using lower stirrer speeds resulted in reduced ferrihydrite production and increased lepidocrocite formation, and even the formation of goethite was observed at the lowest oxygenation rate of 250 rpm. The results indicated that thermodynamic stability is directly influenced by oxygenation and, therefore, the oxidation rate of Fe(II), resulting in more ferrihydrite > lepidocrocite > goethite under higher oxidation rates of electrochemically generated Fe(II).

The adsorption capacity of these various compositions was evaluated through PO_4-adsorption. A relationship was found between higher PO_4-removal and the ferrihydrite content of the rust phase. This is a clear effect of ferrihydrite having a significantly higher specific surface area and higher [≡Fe-OH] per generated Fe(III) compared to lepidocrocite and goethite. Additionally, a relationship was observed between the surface potential, $E_{h,surf}$, and the reduction potential of ferrihydrite and the products resulting from the reductively driven transformation of ferrihydrite. The adsorption of Fe(II) on ferrihydrite created a strongly

49

reduced $E_{h,surf}$, which dropped below the reduction potential of ferrihydrite and induced its reductive dissolution. Furthermore, the crystallinity of ferrihydrite in relation to the pH at the point of zero charge, pH_{pzc}, was found to be essential in determining whether lepidocrocite or goethite would form from the reductively driven recrystallization of ferrihydrite. Freshly precipitated ferrihydrite with a relatively high pH_{pzc} and corresponding low $E_{h,surf}$ only transformed into lepidocrocite, whereas aged ferrihydrite used in unseeded tests had a lower pH_{pzc}, and the adsorption of Fe(II) resulted in an $E_{h,surf}$ below the reduction potential of both ferrihydrite and lepidocrocite, resulting in a significant transformation of ferrihydrite into goethite.

References

APHA (2005) Standard methods for the examination of water and wastewater, 21 ed. American Public Health Association

Arai Y. Sparks D.L, J. Colloid and Interface Sci., 2001, 241, 2, 317-326

Barnes A., Sapsford D.J., Dey M., Williams K.P., J. Geochem. Exploration, **2009**, 100, 2-3, 192-198

Boland D.D., Collins R.N., Miller C.J.; Glover C.J., Waite T.D., Environ. Sci. Technol., **2014**, 48, 10, 5477-5485.

Boland D.D., Collins R.N., Miller C.J.; Glover C.J., Waite T.D., Coll. And Surf. A: Phyisochem. And Eng. Aspects, **2013**, 20, 2-8

Blesa M.A., Matijevic E., *Advances in Colloid and Interface Science* **1989,** 29, (3-4), 173-221.

Cornell R.M., Schwertmann U., The Iron Oxides, second ed.,Wileye Iron Oxides, second ed., **2003**, 521-542

Cudennec Y.; Lecerf A., Journal of Solid State Chemistry **2006,** 179, (3), 716-722.

Dousma J., De Bruyn P.L., J. Colloid Interface Sci. **1976**, 56, 527.

Dousma J., Den Ottelander D., De Bruyn P.L., J. Inorg. Nucl. Chem., **1979,** 41, 1565.

Dublet G., Pacheco G.L., Bargar J.R., Fendorf S., Kumar N., Gregory V. Lowry G.V., Brown Jr G.E. *Geochimica et Cosmochimica Acta*, **2017**, 215, 122-140

Dutrizac J.E., Cim Bulletin **1987**, 80, (903), 94-9421.

Fei Y, Hua J., Liu C., Li F., Zhu Z., Xiao T., Chen M., Gao T., Wei Z., Hao L, Minerals **2018**, 8(8), 357

Flynn C.M., Chem. Rev. **1984**, 84, 31-41.

Gomez M.A., Jiang R., Song M., Li D., Lea As, Ma X.,Wang H., Yin X.,Wang X, Jiae W Nanoscale Adv., **2020**,2, 4938-495

Gorski C.A., R. Edwards, M. Sander, T.B. Hofstetter, Sydney M. Stewart, Environ. Sci. Technol., **2016**, 50, 8538-8547.

Hansel C.M.; Benner S.G.; Fendorf S., *Environ. Sci. & Technol.* **2005,** 39, (18), 7147-7153.

Hiemstra T., Mendez J.C., Li J., *Environ. Sci.: Nano*, **2019**, (3), 820-833.

Holt P.K., Barton G.W., C. A. Mitchell, *Chemosphere*, 2005, 59, 3, 355-367

Honda T., Murase K., Hirato T., Awakura Y., *J. App. Electrochemistry*, **1998**, 28, 617-622.

http://hyperphysics.phy-astr.gsu.edu/hbase/Tables/electpot.html

Jeon B.H., Dempsey B.A., Royer R.A., Burgos W.D., *Environ. Sci. & Technol.*, **2003**, 37, 3309-3315

Jain, A.; Raven, K. P.; Loeppert, R. H. *Environ. Sci. Technol.* **1999**, 33 (8), 1179–1184.

Jia Y., Xu L., Wang X, Demopoulos G.P., *Geochimica et Cosmochimica Acta*, **2007**, 71, 1643–1654

Jolivet J.P.; Tronc E.; Chaneac C., *Comptes Rendus Geoscience* **2006,** 338, (6-7), 488-497.

Jones A.M., Collins R.N., Waite T.D., *Geochim. et Cosmochim.*, 218, **2017**, Pages 257-272

Karapinar N. *Water, Air, & Soil Pollution*, **2016**, 227, 193

Kiyama M.; Takada T.; Shimizu S.; Okuda Y.; Akita T., *Bull. Chem. Soc. Japan* **1972,** 45, (11), 3422-&.

Lakshmanan D., Clifford D.A., Samanta G., *Env. Sci. Tech*., **2009**, 43, 10, 3853-3859

Larese-Casanova P., Kappler A. and Haderlein S.B., *Geochim. Et Cosmochim. Acta,* **2012**, 91, 171-186.

Latta D., Rosso K.M., Scherer M.M., *ACS earth and space chemistry*, **2023**, 7, 10, 1814-1824

Lee K.; Clydesdale F.M., *Journal of Food Science* **1979,** 44, (2), 549-554.

Li X, Liu L, Wu Y., Liu T., *ACS Earth Space Chem.* **2019**, 3, 711−717

Liu H., Zhao X., Qu J., *Chapter 10, Electrocoagulation for water treatment, Electrochemistry for the environment*, **2010**, 245-263.

Liu H.; Li P.; Zhu M.Y.; Wei Y.; Sun Y.H., Journal of Solid State Chemistry **2007,** 180, (7), 2121-2128.

Liu Y, Ding Y, Sheng A, Li A, Chen J., Arai Y. and Liu J. Environ. Sci. Technol. **2023**, 57, 6934−6943

Misawa T. ; Hashimoto K.; Shimodai.S, *Corrosion Science* **1974,** 14, (2), 131-149.

Mollah M.Y.A., Schennach R., Parga J.R., D.L. Cocke, J. Hazardous Mat., **2001**, 84, 1, 29-41

Mollah M.Y.A; R. Schennah; J.R. Parga; D.L. Cocke, Journal of Hazardous Materials B87 **2001,** B84, 29-41.

Moreno H.A., Cocke D.L, Gomes J.A.G., Morkovsky P., Parga J.R., Peterson J. and Garcia C.. *ECS Transactions,* **2007,** 6 (9) 1-15

Morgan B.; Lahav O., Chemosphere **2007,** 68, (11), 2080-2084.

Music M.; Gotic M.; Popovic S., Journal of Materials Science **1993,** 28, (9), 5744-5752.

Yee N., Shaw S., Benning L.G., Nguyen T.H., Am. Mineralogist, **2006**, 91, 92-96

Notini L., Arrigo L.K.T., Kaegi R., Kretzschmar R., *Environ. Sci. Technol.* **2022**, 56, 17, 12723–12733

Oh S.J.; Kwon S.J.; Lee J.Y.; Yoo J.Y.; Choo M.Y*., Corrosion*, **2002,** 58, (6), 498-504.

Persson P.; Lovgren L., *Geochimica Et Cosmochimica Acta* **1996,** 60, (15), 2789-2799.

Park B.; Dempsey B.A., *Environ. Sci. and Technol.* **2005,** 39, (3-4), 6494-6500.

Parks G.A., *Chem. Rev*. **1965**, 39, 177

Pedersen H.D.; Postma D.; Jakobsen R.; Larsen O., *Geoch. Et Cosmoch. Acta* **2005,** 69, (16), 3967-3977.

Qian G.; Chen W.; T. T. Lim; P. Chui, *Journal of Hazardous Materials* **2009**, 70, (2-3), 1093-1100

Raven, K. P.; Jain, A.; Loeppert, R. H., *Environ. Sci. Technol.* **1998**, 32 (3), 344–349

Richmond W.R.; M. Loan; J. Morton; G.M. Parkinson; *Environmental Science Technology* **2004,** 38, (8), 2368-2372.

Ruan H.D.; R. L. Frost; J. T. Kloprogge; L. Duong, Spectrochimica Acta Part a-Molecular and Biomolecular Spectroscopy **2002,** 58, (5), 967-981.

Russell J.D., *Clay Minerals*, **2018**, 14(2), 109–114

Shahedi A. Darban A.K., Taghipour F., Jamshidi-Zanjani A., *Current Opinion in Electrochemistry*, **2020**, 22, 154-169

Scheck J., Wu B., Drechsler M., Rosenberg R., Van Driessche A.E.S, Stawski T.M., and Gebauer D. *J. Phys. Chem. Lett.* **2016**, 7, 3123−3130

Schwertmann U., Cornell R.M., *Iron oxides in the laboratory, 2ⁿᵈ edition*, Wiley-VCH, New York, **2000**, XV.

Schwertmann U., Fischer W, **1973**, Geoderma 10:237–247

Schwertmann U., Friedl J.; Stanjek H., J. Coll. and Interface Sci., **1999,** 209, (1), 215-23.

Schwertmann U.; Stanjek H.; Becher H.H., Clay Minerals **2004,** 39, (4), 433-438

Sheng A., Liu J., Li X., Qafoku O., Collins R.N., Jones A.M., Pearce C.I., Wang C., Geoch. et Cosmochimica Acta 2020, 272, 105-120

Sheng A, Liu J., Li X., Luo L., Ding Y., Chen C., Zhang X., Wang C., Rosso K.M., *Geoch. et Cosmochimica Acta,* **2021**, 309, 272-285

Stanjek H, Weidler PG, *Clay Minerals*, **1992**, 27:397–412.

Stumm W.; Lee G.F., Industrial and Engineering Chemistry **1961,** 53, (2), 143-146.

Tejedor-tejedor M.I.; Anderson M.A., *Langmuir* **1986,** 2, (2), 203-210.

Thamdrup B. *Adv. Microb. Ecol.*, **2000**, 16, 41-84.

Trivedi P.; Axe L., *Environmental Science Technology* **2000,** 34, (11), 2215-2223.

Tronc E., Belleville P., Jolivet J.P., Livage J., *Langmuir*, **1992**, 8, 313–319

Van Genuchten C.M., Behrends T., Kraal P., Stipp S.L.S, Dideriksen K., *Electrochimica Acta*, **2018**, 286, 324-338

Van Genuchten C.M., Pena J., Amrose S.E., Gadgil A.J., *Geoch. et Cosmochim. Acta*, **2014**, 127, 285–304

Villacís-García M. , Mariana Ugalde-Arzate M., Vaca-Escobar K., Villalobos M., Zanella R., Martínez-Villegas N., *Boletín de la Sociedad Geológica Mexicana,* **2015***, 67, 3, p. 433-44

Von der Heyden B. and A.N. Roychoudhury, *Curr. Pollution Rep*., **2015**, (1), 265-279

Wang X., Gu C., Feng X., Zhu M, *Environmental Science and Technology*, **2015**, 49(17)

Weckler B., Lutz H.D., *Eur. J. Solid State & Inorg. Chem*. **1998**, 35, 8-9, 531-544

Yang L., Steefel C.I., Marcus M.A., Bargar J.R., *Environ. Sci. Technol*., **2010**, 44, 14, 5469-5475

Yuwono V. M., Burrows, N. D., Soltis J. A., T. A. Do, Penn L. P., *Faraday Discuss*. **2012**, 159, 235-245 .

Zhang T.C.; Huang Y.G., *Water Research* **2006,** 40, (12), 2311-2320

Zhang Z. Wang. L, Zhou B., Wang S., Fan F, Hu S., Wu Y. *Bulletin of Environmental Contamination and Toxicology*, **2021,** 107, 1191–1201
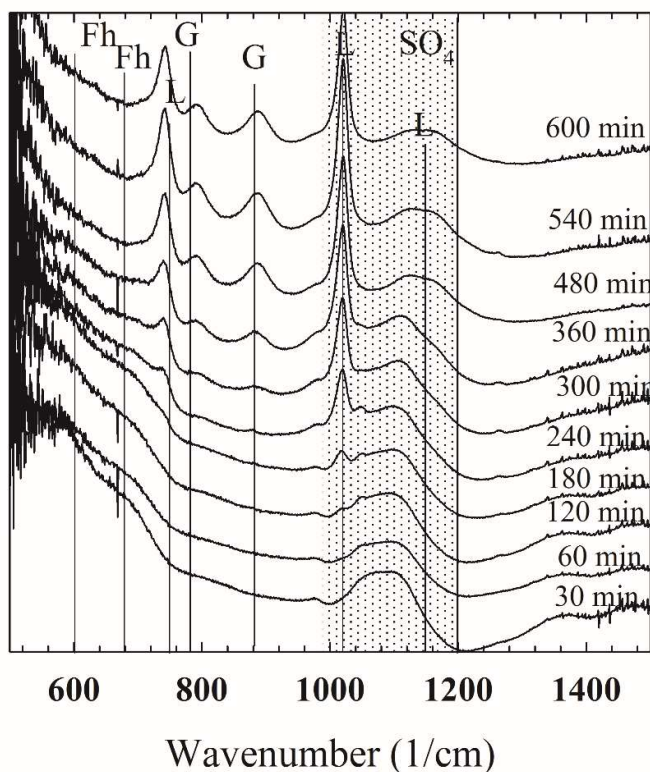
Appendix 2A

Fig. 2A. *The ATR-FTIR data reveals the composition of the rust phase of the iron oxyhydroxide obtained by adding 0.1M FeSO$_4$ to 200 ml of demi-water over a period of 600 minutes. The pH was maintained at 7.0 and the stirrer speed was set at 750 rpm. The dosing rate was adjusted to match the theoretical Fe^{2+} generation rate of 12.5 A/m^2 (equivalent to 6.2 µmol Fe^2+ per minute, with A$_{elec}$ = 0.0016 m^2). Ferrihydrite, lepidocrocite, and goethite are represented by the abbreviations Fh, L, and G respectively. The presence of large and broad bands signifies the adsorbed SO$_4$-vibration bands onto the iron oxyhydroxide phases formed.*

Appendix 2B. XRD data of the phases formed 250 rpm, 500 rpm, 750 rpm, 1000 rpm, 1000 rpm+aeration+1 V% H_2O_2
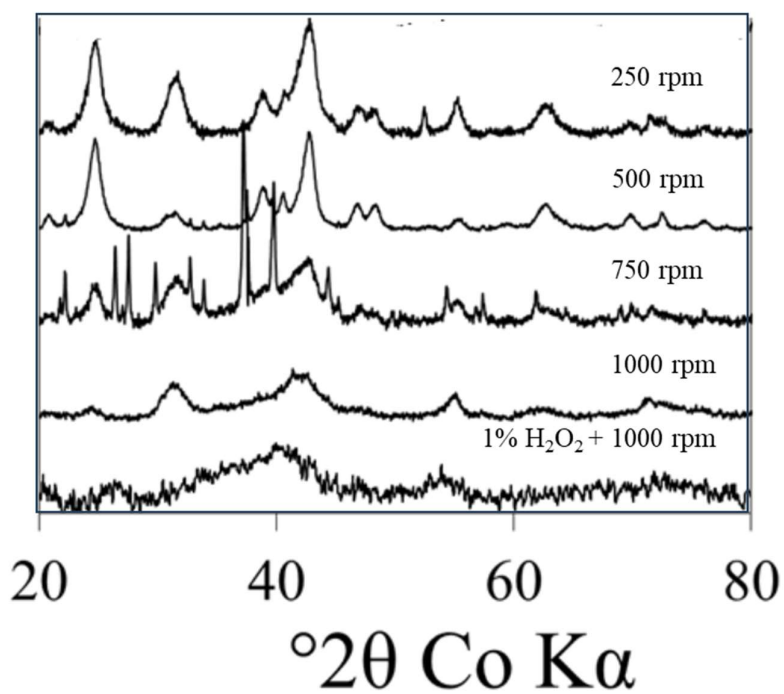
Ferrihydrite formation in iron electro-coagulation system; the role of CO_3 and PO_4.

Abstract. Ferrihydrite is a preferred adsorbent for removing heavy metals and hazardous anions from water streams. The objective of this study is to investigate the role of CO_3- and PO_4- ions in the formation of ferrihydrite during the iron electro-coagulation (Fe-EC) process. ATR-FTIR analysis of the rust phase product of the aerated Fe-EC cell at 20 A/m^2 reveals that higher $[CO_3]_T$ in mixed $[CO_3]_T/[SO_4]_T$ solutions ($[CO_3]_T$ = 5.0-250 mM + $[SO_4]_T$ = 245-0 mM) or $[PO_4]_T$ in $[PO_4]_T/[Cl^-]_T$ solutions ($[PO_4]_T$ = 0.20 and 0.50 mM) result in increased ferrihydrite formation. Although various mechanisms were evaluated, the main process enabling ferrihydrite production was the stabilization of the in-situ forming ferrihydrite against Fe(II)-mediated reductive transformation to goethite and lepidocrocite. This reductive transformation was mediated by the unoxidized fraction of Fe(II), which accumulates in the electrolyte if not fully oxidized by $O_{2(aq)}$. The stabilization was attributed to the competition from adsorbed CO_3- and PO_4- ions on the adsorption of Fe(II) onto ferrihydrite and the subsequent significant decrease in the required electron transfer reaction for the reductive transformation. In waste and process water treatment, these anions are present in significant quantities, and their stabilizing effect on ferrihydrite supports its production through the Fe-EC process.

3.1. Introduction

The Iron Electro-Coagulation (Fe-EC) technology offers the removal of contaminants, such as heavy metals (e.g., Pb(II), Zn(II), Cd(II), Cu(II)), and hazardous anions (Se(VI), As(V)), from wastewater streams without increasing salinity. This advantage enables easier reclamation of water bodies and the restoration of water bodies to previous process conditions, or for use in other purposes, such as irrigation (Xu et al., (2018); Al-Zghoul et al., (2023)). Fe-EC can be easily integrated into existing treatment facilities and has a lower application cost compared to membrane-based and iron-salt treatments (refer to Table 1.1). The Fe-EC process typically achieves the removal of contaminants by in-situ production and utilization of the scarcely soluble iron oxyhydroxide products of steel corrosion (%Fe > 99%). The Fe-EC process operates under an applied electric current (see 1.1-1.12) to control the dosage of Fe(II) and Fe(III) in the water body. However, the Fe-EC process is not effective in removing all types of contaminants, as certain contaminants like Pb(II), Zn(II), As(III,V), (Se(IV,VI)) that are present in low concentrations (in the mg/L range), but still hazardous to health and the environment, require a relatively high Fe(III) dosage of 500-1000 (molar Fe(III)/cont.) to effectively reduce their concentration below the permitted levels for discharge or reclamation (Kim et al., 2014; Karapinar, 2016; Lu et al., 2023). This consequently leads to large sludge production, high electrode consumption (i.e., Fe(0) consumption), and energy usage for steel corrosion, resulting in general operational costs of 12-36 Wh/L of treated wastewater (Ebba et al., 2021).

Ferrihydrite has a relatively high adsorption capacity, with values ranging from 250-1100 m^2/g and approximately $6 \equiv Fe-OH/nm^2$. It has been found to be an effective iron oxyhydroxide in removing contaminants (Karapinar, 2016). Ferrihydrite has successfully removed some of these difficult-to-remove contaminants mentioned above. However, the formation of ferrihydrite in Fe-EC has only been observed under specific pH conditions. According to the studies of Van Genuchten et al. (2014, 2018) and Pan et al. (2017), ferrihydrite is observed at specific pH levels below 5 (Pan et al., 2017) and at a pH of approximately 9 (Van Genuchten et al., 2018). Typically, ferrihydrite formation is accompanied by crystalline phases such as lepidocrocite and goethite. Various studies, including those by Oh et al. (1998, 2002), El-Naggar (2006), Van Genuchten et al. (2014, 2018), Maldonado-Reyes et al. (2015), Pan et al. (2017), and Syam Babu et al. (2021), have characterized the composition of the rust

phase produced by the Fe-EC process at pH 5-9, with the dominant phases being crystalline lepidocrocite and goethite. Kiyama et al. (1972), Chen and Thompson (2021), and Sheng et al. (2020, 2021) have explained the limited formation of ferrihydrite at pH 5-9 due to the enhanced crystallization of Fe(III) when Fe(III) is produced from Fe(II) oxidation during the Fe-EC process (see eq. 1.1-1.12). In Chapter 2, we have demonstrated that ferrihydrite does form but undergoes simultaneous transformation when Fe(II) is not fully oxidized under fully oxygenated electrolyte conditions. Chapter 2 was dedicated to understanding the formation and potential production methods for ferrihydrite through the Fe-EC process. However, for the sole production of ferrihydrite, it was necessary to operate the Fe-EC under vigorous stirring and add 1V% H_2O_2 to mitigate the Fe(II)-mediated reductive transformation of ferrihydrite to lepidocrocite and/or goethite.

CO_3- (dissolved from air) and PO_4- ions (a major contaminant in municipal wastewater) are important components of wastewater, such as domestic sewage. However, their roles in the formation of ferrihydrite are diverse and often unclear. Both CO3- and PO4- ions can form aqueous complexes with Fe(III), which can enhance the formation of ferrihydrite by promoting the polymerization of Fe(III) in favor of ferrihydrite formation (Rose et al., 1997). On the other hand, the formation of aqueous Fe(III)-CO_3 complexes can increase the solubility of ferrihydrite, making it more susceptible to transformation into goethite (Qafoku et al., 2020). In fact, Qafoku et al. (2020) found that CO_3- ions promote the reductive transformation of ferrihydrite to goethite mediated by Fe(II).

The dominant precipitation of siderite ($FeCO_3$) can significantly affect ferrihydrite productivity, as siderite has poor oxidation potential (Guo et al., 2011; Yu et al., 2023). Similarly, the precipitation of vivianite, a form of Fe(II)-PO_4 precipitate, can also impact ferrihydrite formation and stability in municipal waste sludge (Sleimann et al., 2016; Wang et al., 2019).

Regarding the oxidation of ferrous iron, Voegelin et al. (2013) and Kraal et al. (2022) have shown that intermediate am-Fe(PO_4) and Fe-rich ferric hydrous PO_4 (P-HFO) can outcompete ferrihydrite formation when the Fe/P ratio exceeds 0.16. These phases are prone to transformation into lepidocrocite.

Under near-neutral conditions, CO_3- and PO_4- ions are known to adsorb onto ferrihydrite, stabilizing it against dissolution in soil environments (Qafoku et al., 2020). When it comes to Fe electrocoagulation (Fe-EC) applications, the adsorption of CO_3- and PO_4- ions can compete with the adsorption of Fe(II) species (i.e. Fe^{2+} and $Fe(OH)^+$) on the available ≡Fe-OH sorption sites. This competition may potentially reduce the reductive dissolution of

ferrihydrite. However, it remains unclear which of these processes mentioned above dominate ferrihydrite formation and its productivity in the Fe-EC process.

Thus, this study aims to investigate the role of CO_3 and PO_4 in the formation of ferrihydrite phases, particularly in relation to the catalytic role of Fe(II) ions, at varying concentrations of CO_3 and PO_4. Throughout this paper, the total concentration of bicarbonate and phosphate will be denoted as $[CO_3]_T$ and $[PO_4]_T$, respectively.

3.2. Experimental

3.2.1. Experiments

The experiments were conducted in the same electrochemical cell as described in section 2.2.1. The surface area of the iron plates was 0.002 m^2 (4x4 cm). The Fe-EC process (equations 1.1-1.3) was operated at a constant direct current of 0.04 A, corresponding to a current density (J) of 20 A/m^2. The cell voltages ranged from 1.2-1.4 V throughout the 120-minute duration of the experiments (refer to similar cell voltages in Figure 2.5A).

As described in appendix 2A, at this current density, the Fe(0) (steel plates) primarily oxidizes to Fe(II) (98%) at the anode surface according to equation 1.1. In order to ensure a continuous supply of $O_{2(aq)}$ to the electrolyte (through dissolution of $O_{2(g)}$ as $O_{2(aq)}$), the electrolyte was mixed at a moderate stirrer speed of 750 rpm using a magnetite stirrer. Based on the results in Chapter 2 (section 2.3.2), this stirring speed was found to be sufficient for the oxidation of a significant portion of Fe(II) ions formed electrochemically (equation 1.1). The remaining unoxidized portion is allowed to accumulate in the electrolyte, creating conditions for the reductively catalyzed transformation of any formed ferrihydrite. This process was studied in relation to the $[CO_3]$- and $[PO_4]$-.

Table 3.1 presents an overview of the conducted Fe-EC experiments using different electrolyte compositions. Experiments #1-#9 were carried out to investigate the impact of $[CO_3]_T$ + $[SO_4]_T$ (experiments #1-6) and $[PO_4]_T$ + $[Cl^-]_T$ (experiments #7-9) on the formation of iron oxyhydroxide. In these experiments, $NaSO_4$ + $NaHCO_3$ and $NaCl$ + NaH_2PO_4 were dissolved in varying proportions in Milli-Q water. Prior to initiating the Fe-EC experiments, the pH was adjusted to 7.0 using NaOH and H_2SO_4 for experiments #1-6, and with NaOH and

HCl for experiments #7-9. The total electrolyte volume was set to 200 ml before commencing the Fe-EC process.

Tab. 3.1. *The performed Fe-EC experiments under varying $[CO_3]_T/[SO_4]_T$ and $[PO_4]_T/[Cl]_T$.*

Exp.	J (A/m^2)*	$[SO_4]_T$ (mM)	$[CO_3]_T$ (mM)	$[PO_4]_T$ (mM)	$[Cl^-]_T$ (mM)	Stirring speed (rpm)
1	20	245.0	5.0			750
2	20	240	10.0			750
3	20	225.0	25.0			750
4	20	200.0	50.0			750
5	20	100.0	150.0			750
6	20	0.0	250.0			750
7	20				250.0	750
8	20			20.0	250.0	750
9	20			50.0	250.0	750

electrode surface is 0.0025 m^2.

3.2.2. Analysis

At 30, 60, 90, and 120-minute intervals, electrolyte samples were collected and filtered directly under N_2-blanketing using a 0.2 μm pore diameter (Merck-Millipore). The spectroscopic determination of [Fe(II)] was carried out using the 1,10-phenanthroline method with a XION 500 Spectrophotometer (method described in Lee and Clydesdale (1970)) from the supernatant. Additionally, $[PO_4]_T$ was determined spectroscopically using the molybdenum blue method with the same spectrophotometers mentioned earlier, from the supernatant of experiments #7-#9. The filtrate was thoroughly washed with Milli-Q water (under N_2 atmosphere) and left to air dry. ATR-FTIR spectra were obtained from all solid samples using a Shimadzu 4800-sn between the wavenumbers 500 and 4000 cm^{-1}.

Table 3.2. *The vibrational modes of the relevant iron oxyhydroxides were considered in the ATR-FTIR data in this study (Tejedor-Tejedor, (1986); Weckler and Lutz, (1998);* Villacís-García, *(2015); Dutrizac et al., (1987)).*

Iron oxyhydroxide	Wavenumbers (cm^{-1})

Ferrihydrite (2- or 6-line)	~600 (ν(Fe-O)$_{sym}$) ~690 (Fe-OH)$_{sym}$
Lepidocrocite	749 (ν(Fe-O)$_{sym}$), 1020 (Fe-OH)$_{sym}$ and 1115 (Fe-OH)$_{asym}$
Siderite	862 (ν(Fe-O-P)$_{sym}$)
Vivianite	980 (ν(Fe-O-P)$_{sym}$)
Goethite	800 (Fe-OH)$_{sym}$, 890 (Fe-OH)$_{asym}$

3.2.3. Surface complexation modelling

To evaluate the adsorption or complexation of Fe(II), CO$_3$, and PO$_4$ on ferrihydrite phases' surface, the PHREEQC program was utilized. The complexation model data was derived from measurements of [Fe(II)], [CO$_3$]$_T$/[SO$_4$]$_T$, and [PO$_4$]$_T$/[Cl]$_T$. The relevant surface site density and specific surface area can be found in Table 3.2. In the surface complexation modeling, it was assumed that CO$_3$- and SO$_4$- ions form complexes with singly surface-bound $\equiv$Fe-OH groups (referred to as $\equiv$Fe-OH$^{+0.5}$ in Mendez and Hiemstra (2019)). The contribution of triply bound groups $\equiv$Fe$_3$-OH$^{+0.5}$ was not considered significant when compared to the binding of anions by singly bound $\equiv$Fe-OH+0.5 groups (Mendez and Hiemstra (2019)). PO$_4$ was assumed to form both mono- and bidentate complexes (Hiemstra and Zhao (2016)). Additionally, the standard A$_s$ value of 250 m^2/g, used in the 2-site binding model of Dzombak and Morel (1990) in the PHREEQC code for aged (> 1 month) ferrihydrite, was adjusted to approximate realistic conditions of the Fe-EC process, specifically an A$_s$ value of ~470 m^2/g, resembling that of more freshly formed ferrihydrite (Hiemstra et al. (2019)). Further details on this topic are provided in the results and discussion section.

Table 3.3. *PHREEQC modeling parameters and their corresponding surface complexation reactions for the adsorption of PO$_4$, CO$_3$, and SO$_4$ on 2-line ferrihydrite are provided. The model parameters for the adsorption of Fe(II) onto ferrihydrite can be found in Table 2.1.*

Reaction	Log K	pH	OH/ nm^2	A$_s$ (m^2/g)	Reference
$\equiv$Fe-OH$_2^{0.5}$ $\leftrightarrow$ $\equiv$Fe-OH$_2^{-0.5}$ + H$^+$ check	8.1	7.0	6.0	470	(Mendez and Hiemstra, 2019)
2$\equiv$Fe-OH + HCO$_3^-$ $\leftrightarrow$ ($\equiv$Fe-O)$_2$CO +H$_2$O	21.7	7.0	6.0	470	(Mendez and Hiemstra 2019)
2$\equiv$Fe-OH + HPO$_4^{2-}$ $\leftrightarrow$ ($\equiv$Fe-O)$_2$PO$_2$ + 2H$^+$	28.3	7.0	6.0	470	Arai and Sparks (2001) Hiemstra and Zhao (2016), Tiberg et al. (2013)
$\equiv$Fe-OH + HPO$_2^-$ $\leftrightarrow$ $\equiv$Fe-OPO$_2$OH + H$^+$	26.4	7.0	6.0	470	Hiemstra and Zhao (2016)

$\equiv Fe\text{-}OH + SO_4^{2-} \leftrightarrow \equiv Fe\text{-}OSO_4^- + H^+$	0.8	7.0	6.0	470	Das et al. (2013)

3.3. Results and Discussions.

3.3.1. Rust composition at varying $[CO_3]_T/[SO_4]_T$.

The ATR-FTIR data of the iron oxyhydroxides obtained during a 120-minute run of Fe-EC at 20 A/m^2 Fe-EC, with different $[CO_3]_T$ (predominantly HCO_3^- form)/$[SO_4]_T$ (predominantly SO_4^{2-} form) ratios (exp. #1-#6), are shown in Figure 3.1A-F. In the case of the Fe-EC test with 5 mM $[CO_3]_T$ + 245 mM $[SO_4]_T$ (exp. #1, Fig. 3.1A), the bending modes of the $\equiv Fe\text{-}OH$ groups of lepidocrocite (L, γ-FeOOH) dominate the entire 120-minute Fe-EC run at 749 cm^{-1} (ν(Fe-O)$_{sym}$), 1020 cm^{-1} (Fe-OH)$_{sym}$, and 1115 cm^{-1} (Fe-OH)$_{asym}$. Running the Fe-EC with $[CO_3]_T$ of 10 mM (and 240 mM $[SO_4]_T$) (exp. #2, Fig. 3.1B) results in the formation of more goethite, with characteristic bending bands of $\equiv Fe\text{-}OH$ groups of goethite at 612 cm^{-1} (ν(Fe-O)$_{sym}$), 800 cm-1 (ν(Fe-OH)$_{sym}$), and 890 cm^{-1} ((Fe-OH)$_{asym}$) (see Table 3.2). Ferrihydrite (600 cm^{-1} (ν(Fe-OH)$_{sym}$) and 690 cm^{-1} (Fe-OH)$_{asym}$) is not observed in the initial FTIR data at 30 minutes, although in a previous experiment (Chapter 2, Fig. 2.5) of Fe-EC run at 250 mM $[SO_4]_T$ and 20 A/m^2 without CO_3, ferrihydrite formation within the first 30 minutes was clearly demonstrated. Therefore, it is expected that ferrihydrite does form in $[CO_3]_T$ of 5 mM (+245 mM $[SO_4]_T$) and 10 mM (+245 mM $[SO_4]_T$), but it transforms to lepidocrocite at the very early stage (t < 30 min.) of the Fe-EC run. Moreover, the small amount (5 and 10 mM) of $[CO_3]_T$ appears to increase the recrystallization rate of ferrihydrite to lepidocrocite.

At higher $[CO_3]_T$ of 25 and 50 mM (+225 mM and +200 mM $[SO_4]_T$, respectively, exp. #3 and #4 in Fig. 3.1C+D), lepidocrocite is no longer observed, and goethite (α-FeOOH, G) begins to form after 60 minutes of the Fe-EC run, dominating the final rust phase (i.e., 120 minutes). Interestingly, ferrihydrite (Fh, $Fe_5O_7OH\cdot5H_2O$) at 600 cm^{-1} (ν(Fe-OH)$_{sym}$) and 690 cm^{-1} (Fe-OH)$_{asym}$ is observed to precede the goethite formation. This ferrihydrite was found to dominate the rust phase in the first 60 minutes of the Fe-EC run, indicating an increase in ferrihydrite production in electrolytes with $[CO_3]_T > 10$ mM, up to 50 mM. At higher $[CO_3]_T$ of 150 mM (+$[SO_4]_T$ = 100 mM, exp. #5, Fig. 3.1E) and 250 mM (exp. #6, Fig. 3.1F), both lepidocrocite and goethite were no longer observed, and only ferrihydrite (as indicated by bands at 600 and 690 cm^{-1}) was present in the rust phase. These results indicate that higher $[CO_3]_T$ in the electrolyte increases the productivity of ferrihydrite and enables its stability against transformation into goethite.

Some small siderite formations were identified in the first ATR-FTIR run with $[CO_3]_T$ of 150 mM (+$[SO_4]_T$ = 100 mM, exp. #5) and 250 mM (exp. #6) by observing bands at 860 and 910 cm^{-1} (Fig. 3.1E+F). However, compared to the bands of ferrihydrite (Fh), lepidocrocite (L), and goethite (G), the bands representing siderite were relatively small. It is estimated that the formation of siderite accounted for less than 10% of the rust phase. Additionally, no evidence of CO_3-green rust (indicated by sharp bands at 770 cm^{-1}) was observed in the ATR-FTIR. This absence could be due to the insufficiently high pH level (i.e., pH > 8) required for the co-precipitation of Fe(II) and Fe(III), as discussed by Legrand et al. (2004).
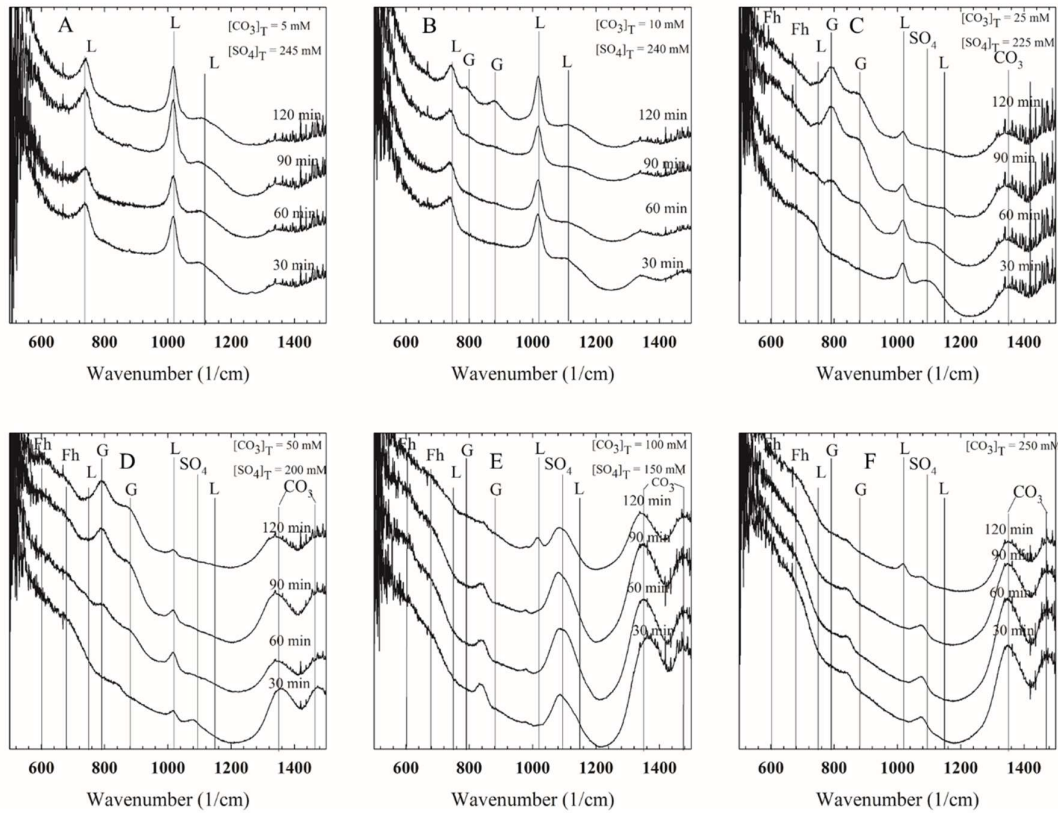

Fig. 3.1. *Periodically, obtained ATR-FTIR spectra of the iron oxyhydroxide phases formed during the Fe-EC run at pH 7.0, with varying $[CO_3]_T$ / $[SO_4]_T$ ratios. Please refer to Table 3.1 for the concentrations. The results of experiments #1-#6 are shown in Figures A-F respectively. These experiments were conducted at a current density of J = 20 A/m^2, with an electrode area of $A_{electrode}$ = 0.0020 m^2, and the electrolyte was mixed at a stirring speed of 750 rpm. This stirring speed ensured high oxygenation (O_2-supply) to the electrolyte. The peaks corresponding to ferrihydrite ($Fe_5O_7OH \cdot 5H_2O$) are denoted as F, lepidocrocite (γ-FeOOH) as L, and goethite (α-FeOOH) as G.*

The increase in goethite formation compared to lepidocrocite formation in high $[CO_3]_T$ (5-50 mM $[CO_3]_T$) is a common feature observed in Fe(II) oxidation studies conducted with Fe(II)-salts such as $FeCl_2$ + $NaHCO_3$. This distinction in goethite formation is generally explained by the "goethite promoting effect" of CO_3-ions, as stated by Tronc et al. (1992) and Rose et al. (1997). According to this effect, CO_3-ions are believed to direct the polymerization of double face-sharing $Fe(OH)_3O_3$ -octahedra into the planar structure of goethite via aqueous complexation (Rose et al., (1997)). However, if the only effect of CO_3-ions on Fe(III) polymerization were this, one would expect an even higher formation of goethite when increasing the $[CO_3]_T$ to 100 and 250 mM (150 mM and 50 mM $[SO_4]_T$, respectively) in the electrolyte. However, in practice, this "goethite-promoting" effect of CO_3-ions disappears and only ferrihydrite dominates the rust phase (Fig. 3.1E and F). In fact, considering the extremely low solubility of Fe(III)-ions and the production rate of Fe(III) of 50-60 μM/min (after extraction of the [Fe(II)] in Fig. 3.2 from the total Fe(II) produced) at the applied current density (J) of 20 A/m^2, a high supersaturation is created throughout the Fe-EC operation period. This supersaturation generally follows Ostwald's rules of stages, where ferrihydrite is typically observed as the initial phase that precipitates. The observation that ferrihydrite forms in ≥ 25 mM $[CO_3]_T$ is consistent with Ostwald's rules of stages. However, despite the prevailing supersaturation, we still observe the transformation of ferrihydrite, whereas fast precipitation studies on Fe(III) at pH 7.0 and room temperature have shown that ferrihydrite transforms very slowly into goethite and hematite (α-Fe$_2$O$_3$) over periods that can last over 10 years (Schwertmann et al., 2004).

In the work of Li et al. (2023), CO_3-ions have been shown to increase the recrystallization rate of ferrihydrite to goethite at $[CO_3]_T$ of 0.20-21 mM (using room temperature and pH 7.5 in Li et al., (2022)). This causes a shortening of the transformation period (more than 40% reduction in an 11 mM $[CO_3]_T$) from 1 year to 80 days. The situation in Fe-EC systems is different because the Fe(III)-ions are produced from the oxidation of Fe(II)-ions (Eq. 1.3). Additionally, the unoxidized Fe(II) can drive the reductively catalyzed transformation of ferrihydrite, as shown by the works of Hansel et al. (2005), Pedersen et al. (2005), Boland et al. (2013, 2014), and Sheng et al. (2020, 2021).

In the following section, the role of Fe(II) in ferrihydrite formation in relation to $[CO_3]_T$ / $[SO_4]_T$ is further studied and discussed by incorporating the data on Fe(II) and considering the electrolyte potentials at the ferrihydrite interface as an indicator of the electron transfer process between Fe(II) and ferrihydrite.

3.3.2. The Fe(II)-induced recrystallization ferrihydrite in relation to $[CO_3]_T/[SO_4]_T$.

The $[O_{2(g)}]$ and $[Fe(II)]$ values measured throughout the 120-minute Fe-EC course at 20 A/m^2 are depicted in Figure 3.2. In all tests, the $O_{2(aq)}$ supply at the applied stirring speed (750 rpm, moderately high oxygenation) was insufficient to fully oxidize the generated Fe(II) (with a Fe(II) production rate of 62 μM/min). As a result, $[O_{2(g)}]$ decreased and $[Fe(II)]$ subsequently increased over the course of 120 minutes of Fe-EC operation. From the total amount of electrochemically produced Fe(II) (designated as $[Fe(II)]_T = 7.46$ mM with 100% current efficiency), approximately 84-90% was oxidized within the $[CO_3]_T$ range of 5-250 mM ($[SO_4]_T$ ranged from 0-245 mM, refer to the table for the applied concentrations in the electrolyte phase). For comparison, the overall oxidation rates of Fe(II) observed in this study were 30-40 times faster than the general oxidation rate of aqueous Fe(II) using the rate expression by Morgan and Lahav (2007). The difference lies in the continuous formation of ferrihydrite, lepidocrocite, and goethite, which are known to catalyze the oxidation of adsorbed Fe(II) (Chen and Thompson (2021)). While the exact reason for this catalytic role is not yet fully understood, it is hypothesized that the electron transfer driving the reductively catalyzed transformation of ferrihydrite, which involves the adsorption of Fe(II) onto ferrihydrite, lepidocrocite, and goethite, lowers the oxidation-reduction potential of Fe(II) (0.05 V on ferrihydrite compared to 0.77 V in aqueous form), making it more reduced and enabling faster reaction rates with $O_{2(aq)}$. Consequently, the faster oxidation rates observed in this study can be attributed to the dominating heterogeneous oxidation of Fe(II) mediated by the formed rust phases as compared to the overall oxidation of Fe(II) (Barnes et al., (2009)).
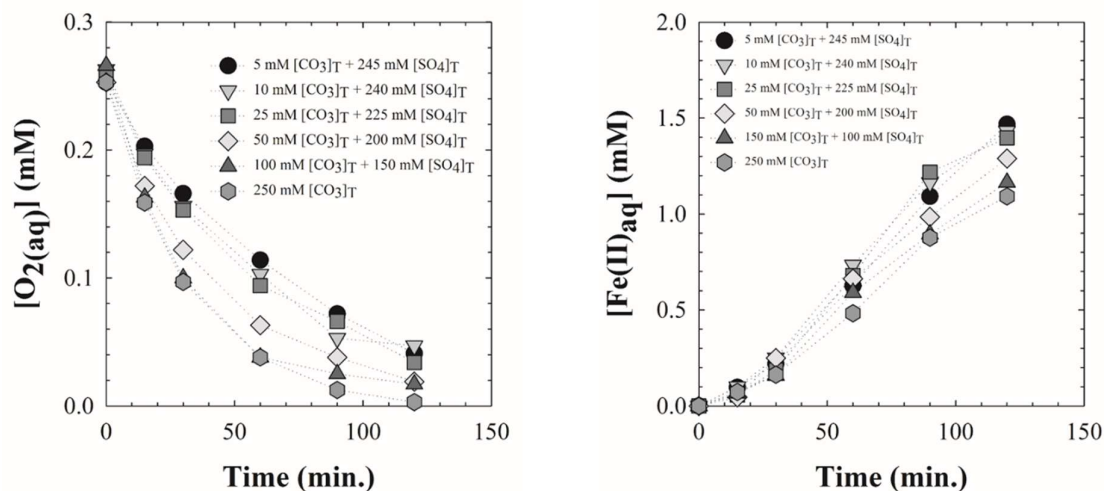
Fig. 3.2. *The changes in the [$O_{2(aq)}$] and [Fe(II)] were observed during the Fe-EC run at pH 7.0, while varying the ratio of [CO_3]$_T$ to [SO_4]$_T$. The experiments were conducted with a current density of J = 20 A/m^2 (with an electrode area of 0.0020 m^2) and the electrolyte was mixed at a stirring speed of 750 rpm. This stirring speed ensured a high level of oxygenation (O_2-supply) to the electrolyte solution.*

The catalytic transformation of ferrihydrite by Fe(II) involves an electron transfer process between Fe(II) and the ferrihydrite at the liquid-surface interface. The driving force of this electron transfer has been attributed to the electrolyte potentials and the reduction potential of ferrihydrite. Basically, when the $E_{h,elec}$ reaches below the reduction potential of ferrihydrite (+0.05 V, Xi et al. (2023) at pH 7.0 and RT), electron transfer is presumed to reduce the Fe^{3+} structure of ferrihydrite. The constant electron transfer and redissolution of Fe^{2+} are then considered to drive a rapidly catalyzed transformation of ferrihydrite (see eq. 2.3-2.6) to stable lepidocrocite and/or goethite. This phenomenon is outlined and described in the works of Yang et al. (2010) and Boland et al. (2013, 2014). The electrolyte potential, $E_{h,elec}$ (see eq. 2.5 appendix 2D), arises from the redox couple between the accumulated Fe(II)-ions (Fig. 3.2b) and non-precipitated Fe(III)-ions (as determined by the solubility of the apparent iron oxyhydroxide phase). In contrast to the ferrihydrite recrystallization studies carried out under deoxygenated conditions and in the presence of Fe(II), in our experiments, the [$O_{2(aq)}$] is not depleted and remains continuously present in the electrolyte. $O_{2(aq)}$ is a redox-active species that contributes to the $E_{h,elec}$ and is included to determine the apparent $E_{h,elec}$ (see eq. 2.5). A second distinctive aspect of the experiments carried out in this work is that both Fe(II) and Fe(III) ions form aqueous complexes with CO_3- ions, and these aqueous complexes are not redox-active. Therefore, their formation alters the speciation of the aqueous redox-active Fe(II)

(Fe^{2+}, $FeOH^+$) and Fe(III) ($FeOH^{2+}$, $Fe(OH)_2^+$, $Fe(OH)_4^-$) and consequently affects the $E_{h,elec}$. To provide the closest approximation for quantifying the $E_{h,elec}$, the speciation of Fe(II) and Fe(III) were further analyzed and included to determine the most appropriate $E_{h,elec}$. According to King et al. (1999), Fe(II) ions are known to form $Fe(HCO_3)(OH)$- complexes in the presence of CO_3. Using the stability constant in King et al. (1999), it was determined that approximately 2% of the accumulated [Fe(II)] exists as $Fe(HCO_3)(OH)$, while the majority is present in the Fe^{2+} form (97%), and only a small percentage exists as $Fe(OH)^+$-ions (1%). Therefore, the measured [Fe(II)] in Fig. 3.2 can largely be considered to exist in the Fe^{2+} form. On the contrary, Fe(III)- and CO_3- ions form stronger aqueous $FeOHCO_3$ complexes at pH 7.0 and room temperature (RT) through the following reaction (Grive et al. (2014) and Mendez and Hiemstra (2019):

$$Fe^{III} + OH^- + CO_3^{2-} \leftrightarrow FeOHCO_3^0 \qquad\qquad\text{eq. 3.2}$$

Grive et al. (2014) and Mendez and Hiemstra (2019) conducted studies on complexes in ferrihydrite-CO_3 systems at pH 5-9 and RT. They observed that these complexes significantly increase the solubility of ferrihydrite. However, these studies were conducted without the presence of Fe(II). The situation is quite different in the Fe(II)-catalyzed reductive transformation of ferrihydrite, as this process produces the labile Fe(III) intermediate (Sheng et al., (2020)). The [Fe(III)]$_{labile}$ can consistently reach up to 0.1-0.4 mM, compared to the original ferrihydrite's solubility of [Fe(III)]$_{Fh}$ = $3*10^{-17}$ mM (Sheng et al., (2020)). Although the composition of this labile Fe(III) is yet to be determined, it has been shown to form aqueous complexes with Xylenol orange, suggesting that the labile Fe(III) mainly consists of aqueous forms of Fe(III)-ions. Therefore, it can be presumed that the labile Fe(III) also forms aqueous $FeOHCO_3$-complexes, which impact the speciation of labile Fe(III). The stability constant for the $FeOHCO_3$-complex is $logK_{FeOHCO3}$ = 10.7 (Grive et al., (2014)). A minimum concentration of 0.1 mM was used for [Fe(III)]$_{labile}$ in calculations based on the studies by Sheng et al. (2020, 2021) and Li et al. (2022) to estimate the [Fe(III)] and [$FeOHCO_3$]. Based on these calculations (shown in Tab. 3.4), it was found that only a small fraction of labile Fe(III) ions (>97%) were complexed as $FeOHCO_3$ complexes in the Fe-EC experiment with a low [CO_3]$_T$ of 5 mM ([SO_4]$_T$ of 245 mM). In contrast, a substantially larger proportion of labile Fe(III) (58%) was complexed in the Fe-EC experiment with a [CO_3]$_T$ of 250 mM (+ [SO_4]$_T$ 0 mM), indicating the significant role of aqueous $FeOHCO_3$ complexes in the speciation of labile [Fe(III)].

Tab. 3.4. *The labile Fe(III) speciation for experiments #1-#6 assumes the formation of a labile [Fe(III)]$_T$ of 0.1 mM during the process of ferrihydrite formation and transformation (refer to Fig. 3.1A-F). This concentration is based on the findings of Sheng et al. (2020a), who observed intermediate labile Fe(III) at this concentration. The [FeOHCO$_3$] and [Fe(III)] were calculated using reaction 3.2 and a logK$_{FeOHCO3}$ value of 10.76.*

Exp.	J (A/m^2)*	[CO$_3$]$_T$ (mM)	Labile [Fe(III)] (%)	Labile [FeOHCO$_3$] (%)
1	20	5.0	97	3
2	20	10.0	93	7
3	20	25.0	85	15
4	20	50.0	72	28
5	20	150.0	51	49
6	20	250.0	42	58

The calculated non-complexed [Fe(III)] was found to be 0.10-0.04 mM. Assuming a calculated α(Fe(III)) (activity coefficient, γ(Fe(III)) = 0.9) at an ionic strength of approximately 200 mM (Millero et al. (1987)), and using the [Fe(II)] and [O$_{2(aq)}$] values shown in Figures 3.2a and 3.2b respectively, the electric potential (E$_{h,elec}$) is determined to range between +0.3 and +0.40V using equation 2.5 (Appendix 2D). Although the poor transformation of ferrihydrite to goethite observed in experiments conducted with a [CO$_3$]$_T$ + [SO$_4$]$_T$ of 150 + 100 mM (exp. #5) and a [CO$_3$]$_T$ of 250 mM (exp. #6) initially suggests that the E$_{h,elec}$ is above the reduction potential of ferrihydrite (E$_{h,elec}$ < -0.05 using cyclic voltammetry in Liu et al. (2019)), indicating that no catalytic transformation is expected to occur, the transformation of ferrihydrite to goethite still takes place through this catalyzed pathway in experiments conducted with a [CO$_3$]$_T$ + [SO$_4$]$_T$ of 25 + 225 mM (exp. #3) and 50 + 200 mM (exp. #4). This demonstrates that the use of E$_{h,elec}$ as a measure to describe the Fe(II)-induced catalytic transformation of ferrihydrite does not apply in this situation. Further steps have been taken to investigate whether the catalytic process involves a surface-mediated process, regardless of the E$_{h,elec}$ value.

3.3.3. The role of adsorbed carbonate on the ferrihydrite recrystallization by Fe(II)

CO$_3$- ions, and to a lesser extent SO$_4$- ions, are known to adsorb onto the surface of ferrihydrite. These complexes have the potential to compete with Fe(II) for the available binding sites (i.e. ≡Fe-OH). The adsorption of CO$_3$- onto ferrihydrite is supported by the ATR-FTIR data (Fig. 3.1 A-F), which show large and broad asymmetric (ν(C-O)$_{symm}$) and symmetric (ν(C-O)$_{symm}$) bending bands of CO$_3$- ions at 1345 and 1430 cm^{-1} (Villalobos and Leckie, (2001); Hausner, (2009)). The bending band at 1345 cm^{-1} is attributed to bidentate inner-sphere complexes, i.e. (≡Fe-O)$_2$-CO (Mendez and Hiemstra, (2019)), while the bending band at 1430 cm^{-1} is caused by outer-sphere complexation. In this study, we focus on the role of bidentate inner-sphere complexes in potentially masking the electron transfer process between Fe(II) ions and ferrihydrite. ATR-FTIR data alone are not suitable for directly quantifying the adsorbed CO$_3$- ions on ferrihydrite. Instead, we applied a two-site thermodynamic adsorption model of PHREEQC (see Dzombak and Morel model parameters in section 3.2) to assess the competitive adsorption of Fe(II), SO$_4$-, and CO$_3$- ions. We used the [Fe(II)]$_T$ and [CO$_3$]$_T$ values obtained from the data in Fig. 3.2 as input data for the modeling. For the relevance of this work, the surface complexation model is only applied during periods in which ferrihydrite forms (refer to ATR-FTIR data in Fig. 3.1 for the periods in which ferrihydrite was formed prior to transformation). As ferrihydrite is *in situ* formed during the Fe-EC tests, we assume that the ferrihydrite formed in the first 30-60 minutes has a relatively high A$_s$ content compared to aged ferrihydrite, as aging leads to a decrease in A$_s$ content over time (e.g., As = 250 m^2/g after >1 week aging, as reported in Hiemstra et al., (2019)). Therefore, we used a higher specific surface area of 470 m^2/g (refer to Tab. 3.1) (Hiemstra et al., (2019); Majzlan, (2014)) instead of the commonly used value of 250 m^2/g for aged ferrihydrite. For comparison, the surface complexation modeling was also applied without the presence of CO$_3$- ions. The c(Fe(III))$_{Fh}$ was roughly estimated to be single-digit. The results of this modeling are presented in Tab. 3.5.

Table 3.5. *The surface occupation of Fe(II), [CO$_3$]$_T$, [SO$_4$]$_T$ on ferrihydrite was periodically measured during the Fe-EC experiments conducted under different [CO$_3$]$_T$ + [SO$_4$]$_T$ conditions (exp. #1-#6). The table also includes model calculations without carbonate, only considering [SO$_4$]$_T$. The available non-complexed ≡Fe-OH groups are represented by (Fe-OH). Surface complexation calculations are performed only until ferrihydrite formation is observed. These values are obtained using the two-site surface complexation model by Dzombak and Morel, implemented in the PHREEQC code (refer to Tab.*

time (min)	$Fe(II)_T$ (%)	CO_{3T} (%)	SO_{4T} (%)	$\equiv$Fe-OH (%)	$Fe(II)_T$ (%)	CO_{3T} (%)	SO_{4T} (%)	$\equiv$Fe-OH (%)
	250mM [CO₃]ₜ							
30	2.6	94.2	0.0	2.7	14.3	0.0	0.0	84.9
60	3.1	93.9	0.0	3.0	12.8	0.0	0.0	36.8
90	3.1	93.6	0.0	3.0	19.5	0.0	0.0	79.9
120	3.0	93.6	0.0	3.0	17.6	0.0	0.0	81.9
	100mM [CO₃]ₜ + 150mM [SO₄]ₜ				*150mM [SO₄]ₜ*			
30	2.9	92.5	0.1	4.4	12.1	0.1	24.5	63.0
60	3.5	92.0	0.1	4.3	16.8	0.2	24.9	57.9
90	3.9	91.7	0.1	4.2	17.4	0.1	24.9	57.3
120	3.8	91.7	0.1	4.3	16.3	0.1	24.9	58.5
	50 mM [CO₃]ₜ + 200 mM [SO₄]ₜ				200mM [SO₄]ₜ			
30	3.9	86.1	0.5	9.3	12.1	0.1	24.5	63.0
60	5.6	84.8	0.6	8.9	16.8	0.2	24.9	57.9
	25 mM [CO₃]ₜ + 225 mM [SO₄]ₜ				225 mM [SO₄]ₜ			
30	5.3	78.9	1.5	14.2	12.2	0.2	26.2	54.3
60	7.5	77.0	1.7	13.6	17.2	0.1	26.6	55.9
	10 mM [CO₃]ₜ + 240 mM [SO₄]ₜ				240 mM [SO₄]ₜ			
15*	3.7	64.6	4.2	24.6	5.7	0.2	25.2	65.9
	5 mM [CO₃]ₜ + 245 mM [SO₄]ₜ				245 mM [SO₄]ₜ			
15*	4.6	50.0	8.4	34.2	6.2	0.2	25.3	65.4

* These model calculations are obtained on the assumption that ferrihydrite forms in the first 30 min.

The modeling results indicate that CO_3-ions cover a significant portion of the available surface $\equiv$Fe-OH groups (also referred to as $\equiv$Fe-OH$^{+0.5}$) on ferrihydrite, resulting in strong

competition for Fe(II) binding and leaving only a small amount of non-complexed ≡Fe-OH. Testing at higher $[CO_3]_T$ leads to increased adsorption of CO_3-ions and stronger competition for Fe^{2+} adsorption onto the formed ferrihydrite. At the highest $[CO_3]_T$ of 100 mM ($+[SO_4]_T = 150$ mM) and 250 mM, the total surface-bound Fe^{2+} is about 5.5-6.0 times lower compared to the modeled data in the absence of any CO_3-ions. The extensive occupancy of surface sites by CO_3-ions and Fe(II) reduces the availability of ≡Fe-OH groups by a factor of 27-31 times, indicating that very few free ≡Fe-OH groups remain. Since the electron transfer rate to the ferrihydrite phase and the rate of ferrihydrite transformation are directly determined by Fe^{2+} adsorption (Yang et al. (2010), Boland et al. (2014), eq. 2.3 + eq. 2.4), the large amounts of bound CO_3-ions appear to lower the electron transfer rates to ferrihydrite and consequently its reductive dissolution rate, as evidenced by the increased ferrihydrite production through the Fe-EC process at higher $[CO_3]_T$. It should be noted that adsorbed CO_3-ions do not completely block Fe(II) adsorption, so it can be suggested that the reductively catalyzed transformation is expected to occur after longer Fe-EC tests than the ones applied here (2 hours), especially considering that CO_3-ions can further enhance the transformation of ferrihydrite to goethite in the long term (>20-30 hours) by forming $FeOHCO_3$ complexes (Li et al. 2022). In the Fe-EC experiments conducted with an electrolyte containing 25 and 50 mM $[CO_3]_T$, the percentage of Fe(II) on the surface of ferrihydrite rapidly increases from ~3% to 6-7% within the 30 to 60-minute period, coinciding with the start of ferrihydrite transformation into goethite. Presumably, as more Fe(II) starts to outcompete the adsorption of CO_3-ions, this increase in adsorbed Fe(II) triggers the transformation of ferrihydrite to goethite. Furthermore, the fact that the transformation almost ceases within the 120-minute Fe-EC run at higher $[CO_3]_T$ (≥ 100 mM) suggests that CO_3-ions act as goethite promoters after long aging periods (according to Qafoku et al. (2020), Hansel et al. (2005)), while acting as strong inhibitors during the short 120-minute period.

Although direct measurement of labile Fe(III) is not done in this study, the works of Sheng consistently indicate that labile Fe(III) forms during the catalytic conversion process of ferrihydrite. This leads to the second effect on the transformation of ferrihydrite to lepidocrocite and/or goethite, which is the role of adsorbed CO_3- ions in the production of labile Fe(III) and the [Fe(III)]. The formation of labile Fe(III), its concentration evolution during the transformation period, and the subsequent consumption rates by secondary precipitation depend on the rates of electron transfer from Fe(II) to ferrihydrite and the subsequent surface oxidation of adsorbed Fe(II) to Fe(III). Generally, faster electron transfer temporarily leads to higher levels of labile [Fe(III)]. The adsorbed CO_3- ions on the surface of ferrihydrite can be

observed to reduce the rates of labile Fe(III) formation, limiting the increase in labile [Fe(III)]. Assuming that the surface oxidation of Fe(II) to Fe(III) is proportional to the adsorbed Fe(II), it can be assumed that the experiments (exp. #5 and #6) conducted with $[CO_3]_T$ of 150 (+ $[SO_4]_T$ = 100 mM) and 250 mM, which exhibited 6 times lower adsorption of Fe(II) to ferrihydrite, would produce labile Fe(III) up to [Fe(III)] < 0.017 mM. Taking into account that labile Fe(III) forms the $FeOHCO_3$ complex, the estimated labile [Fe(III)] (0.008 mM) is 12 times lower than the typically observed labile [Fe(III)] of > 0.1 mM in Fe(II)-driven ferrihydrite transformation in the absence of carbonate (Sheng et al., (2020a)). Similar to the effect of citric acid complexation on labile Fe(III), where the formation of labile Fe(III)-citric complexes reduces the crystallization rates of labile Fe(III), it can be expected that the formation of the $FeOHCO_3$ complex significantly affects the crystallization rate of goethite nuclei, in addition to the role of adsorbed CO_3- ions in reducing the rates of electron transfer. Furthermore, in addition to the pronounced delay in the recrystallization of ferrihydrite into goethite observed at $[CO_3]_T$ of 150 (+ $[SO_4]_T$ = 100 mM) and 250 mM due to the presence of adsorbed CO_3- ions, the reduction in labile [Fe(III)] can also be partially attributed to the significant decrease in goethite formation.

The effect of SO_4 on reducing the catalytic event is much smaller than that of CO_3, and this effect is clearly evident in the poor formation of ferrihydrite at the highest $[SO_4]_T$ of 240 and 245 mM. In these cases, sulphate outcompetes the adsorption of Fe(II) by less than 2 to 5% in the range of $[SO_4]_T$ from 5 to 245 mM. It should be noted that this model only considers simplified adsorption of CO_3- and Fe(II)-ions, while ferrihydrite may consist of various active sites with different binding energies. The types and extent of binding are also much more complex.

3.3.4. Strong reduction in the recrystallization of ferrihydrite by PO4-ions

Fig. 3.3 shows the ATR-FTIR spectra of Fe-EC carried out in the absence of PO_4 (as Na_2HPO_4) and in the presence of 0.20 and 0.50 mM of $[PO_4]_T$ (background electrolyte of 0.25 M NaCl). In the absence of PO_4 ions (0.25M NaCl), ferrihydrite (denoted as Fh at 600 and 690 cm^{-1}) is not observed at all, while lepidocrocite with bands at 749, 1021, and 1115 cm^{-1} dominates the rust phase, similar to earlier tests in SO_4-rich solution (see Fig. 1a). As discussed in section 2.3, we speculate that ferrihydrite forms at an early stage of the Fe-EC and that it transforms (see Chapter 2 for more discussion) before the first analysis on the rust phase was done, which is at 30 min of the Fe-EC run. In 0.20 mM of $[PO_4]_T$, ferrihydrite forms (denoted as Fh in Fig. 3.3) up to 30-60 min, beyond which the formed ferrihydrite transforms to lepidocrocite. In 0.50 mM $[PO_4]_T$, ferrihydrite forms up to 90 min and is still observed in the final rust phase together with

lepidocrocite. This clearly demonstrates that increasing the $[PO_4]_T$ increases the production of ferrihydrite and delays its transformation. Goethite (800 and 880 cm^{-1}) was not observed, indicating that ferrihydrite recrystallization does not occur at 20 mM $[PO_4]_T$ (vibration bands at 749, 1020, and 1116 cm^{-1}).
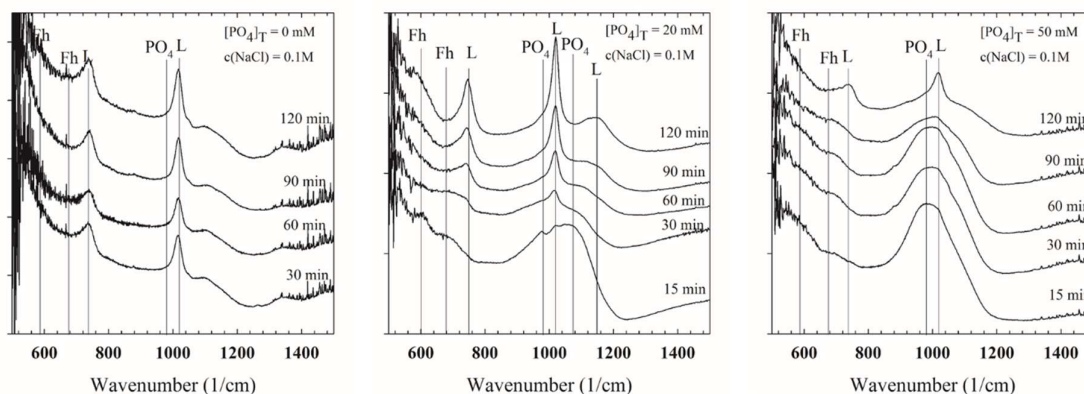

Fig. 3.3. *ATR-FTIR spectra were periodically obtained for the iron oxyhydroxide formed during an aerated Fe-EC run at pH 7.0. The electrolyte composition was 0.25M $[NaCl]_T$, with no presence of PO_4, and in the presence of 0.20 mM and 0.50 mM $[PO_4]_T$. The experiments were conducted with $J = 20$ A/m^2 and an electrolyte mixing using a stirring speed of 750 rpm, which resulted in high oxygenation of the electrolyte (O_2-supply). The peaks corresponding to ferrihydrite ($Fe_5O_7OH \cdot 5H_2O$) were represented by Fh, lepidocrocite (γ-FeOOH) by L, and goethite (α-FeOOH) by G. The background electrolyte consisted of 100 mM of NaCl.*

Fig. 3.4 depicts the $[PO_4]_T$, $[O_{2(aq)}]$, and $[(Fe(II)]$ during the test. When the test was conducted with an initial $[PO_4]_T$ of 0.20 mM, the $[PO_4]_T$ decreased rapidly initially and was completely eliminated after 60 minutes of Fe-EC operation. A similar trend was observed when the test was conducted with an initial $[PO_4]_T$ of 0.50 mM, except that in this case, the complete removal of PO_4 occurred after 120 minutes of Fe-EC run. In all tests, the $[O_{2(aq)}]$ dropped rapidly to approximately 0.02 mM within the first 30 minutes and remained constant for the remainder of the Fe-EC run. As a result, the oxidation rate of Fe(II) decreased, leading to the accumulation of Fe(II) ions (indicated by an increase in $[(Fe(II)]_{aq}$) throughout the 120-minute duration of the Fe-EC process.

Out of the total Fe(II) ions produced at an applied current density of $J = 20$ A/m^2 (n(Fe^0) = 2, as explained in chapter 2), 94%, 90%, and 87% were oxidized in the absence of $[PO_4]_T$, with an initial [PO4]T of 0.20 mM, and with an initial $[PO_4]_T$ of 0.50 mM, respectively. The

slightly faster oxidation rate of Fe(II) in the absence of PO$_4$ ions (as observed from the faster O$_2$ consumption in Figure 3.4) can be attributed to the reduction in the heterogeneous oxidation of Fe(II) due to the competing adsorption of PO$_4$ ions onto the forming precipitates.

In the first 30-minute period, the electrolyte composition shows a measurement of 0.02 mM [Fe(II)] and 0.05 mM [PO$_4$]$_T$. These conditions are found to be supersaturated with respect to vivianite (Fe$_3$(PO$_4$)$_2$.8H$_2$O) with a Log(ion activity product) – log K$_{sp}$ value of 6.8. However, the ATR-FTIR data (Fig. 3.4a and b) does not indicate the presence of vivianite, which is characterized by bending bands at 621 and 827 cm^{-1}. The precipitation of vivianite seems to have a minor role in controlling the [Fe(II)]$_T$ and [PO$_4$]$_T$. This is likely due to the low levels of supersaturation, which are not sufficient to promote enough vivianite precipitation to compete with the formation of ferrihydrite (as observed in ATR-FTIR analysis). Therefore, in the tests carried out with 0.20 and 0.50 mM [PO$_4$]$_T$, the removal of PO$_4$-ions is primarily achieved by the *in-situ* formation of ferrihydrite.
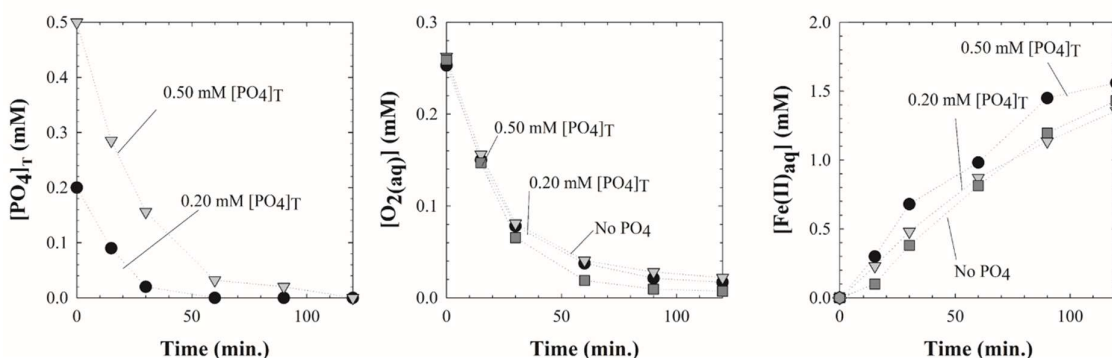

Fig. 3.4. *The [PO$_4$]$_T$, [O$_{2(aq)}$], and [Fe(II)]$_T$ were recorded over time in an aerated Fe-EC run at pH 7.0. The electrolyte composition consisted of 0.25M [NaCl]$_T$ with no PO$_4$, and experiments were conducted with 0.20 mM and 0.50 mM [PO$_4$]$_T$. The experiments were performed at a current density (J) of 20 A/m^2. The electrolyte was stirred at a speed of 750 rpm, which facilitated high oxygenation of the electrolyte.*

Contrary to CO$_3$-ions, which form FeOHCO$_3$-complexes with Fe(III), PO$_4$-ions form weak complexes with Fe(III)-ions. This means that the formation of aqueous complexes between labile Fe(III) or Fe(III) in general with PO$_4$-ions is not significant in the speciation of Fe(III)-ions. Instead, the dominant species in Fe(III) speciation is Fe(OH)$_2^+$ -ions. On the other

hand, Fe(II)-ions also form weak complexes with PO$_4$-ions, resulting in the majority of Fe(II) existing as Fe^{2+}- (98%) and FeOH$^+$-ions (2%) based on previous analysis in section 2.3.1.

Using the [Fe(II)] and [O$_{2(aq)}$] in Fig. 3.4 for the test conducted with 0.20 and 0.50 mM [PO$_4$]$_T$, and assuming a labile [Fe(III)] of 0.1 mM (which is formed when electron transfer leads to surface oxidation and release of Fe(III) to the electrolyte), Eq. 2.5 was used to determine the E$_{h,elec}$, which was found to be around +0.1 V in the first 60 minutes when ferrihydrite was still present in the rust phase (30 minutes in 0.20 [PO$_4$]$_T$ and 60 minutes in 0.50 mM [PO$_4$]$_T$). This calculated E$_{h,elec}$ is higher than the reduction potential of ferrihydrite (+0.05 V) reported by Liu et al. (2022), suggesting that electron transfer-driven transformation was not expected. However, this contradicts the observed reductively catalyzed transformation of ferrihydrite (Fig. 3.3A).

As described in Chapter 2, the development of surface potentials appears to enable the Fe(II)-catalyzed transformation of ferrihydrite. Considering the consistent trend observed in experiments conducted with [PO$_4$]$_T$ 0.20 and 0.50 mM, where PO$_4$-ions cause a significant delay in ferrihydrite transformation in the first 60-90 minutes of the 120-minute Fe-EC run (Fig. 3.3), it is hypothesized that the removal of PO$_4$-ions may be responsible for the reduction in the reductively catalyzed transformation of ferrihydrite due to surface effects. Evidence of adsorbed PO$_4$-ions is seen in the ATR-FTIR spectra, indicated by broad bands at 900-1200 cm^{-1} (ν(P-O)$_{sym}$ and ν(P-O)$_{asym}$) (Fig. 3.3), corresponding to both bidentate and monodentate complexation reactions (See Tab. 3.1 for details of these surface adsorption reactions).

To further investigate the competition between Fe(II)- and PO$_4$-ion adsorption on ferrihydrite, a two-site adsorption model developed by Dzombak and Morel (1990) was used. The modeling was based on data obtained from [PO$_4$]$_T$- and [Fe(II)]-data in Fig. 3.4, and focused on the period when ferrihydrite forms (Fig. 3.3). Tab. 3.5 summarizes the results of this modeling, including the total adsorbed Fe(II) ([(Fe-O-FeOH]+[(Fe-O-FeO$^+$]), total adsorbed PO$_4$ (bidentate + monodentate), and total non-complexed hydroxyl groups [$\equiv$Fe-OH]. The adsorbed PO$_4$-ions cover approximately 94% and 95% of the total available surface (Fe-OH groups of the ferrihydrite phase that evolved in the first 30 minutes of the Fe-EC run) in 0.20 mM and 0.50 mM [PO$_4$]$_T$, respectively, leaving only 2.7% and 2.1% of FeOH free from any complexation. Additionally, the presence of adsorbed PO$_4$-ions leads to a 4.6 and 5.7 times lower adsorption of Fe(II), as indicated by [(Fe-O-Fe(II)], compared to the modelled data in the absence of PO$_4$-ions.

Therefore, considering that the rate of reductively catalyzed transformation of ferrihydrite depends on Fe(II) association and subsequent electron transfer to the structure of

ferrihydrite, as well as the formation of surface potential (as discussed in section 2.7), the presence of adsorbed PO_4-ions, and possibly structural incorporation of PO_4, significantly decreases the reductively catalyzed transformation of ferrihydrite by competing with the binding sites for Fe(II) adsorption. This decrease occurs during the initial stages, beyond which the decrease in $[PO_4]_T$ due to ongoing removal of PO_4-ions and the continuous generation of Fe(III) leads to a decrease in PO_4-loading onto forming ferrihydrite, thereby exposing more surface sites for Fe(II) adsorption. The simultaneous increase in [Fe(II)]/[Fe(III)] ratio enables more adsorption of Fe(II) onto the forming ferrihydrite, contributing to the reductively catalyzed transformation of ferrihydrite after approximately 30 and 60 minutes of the Fe-EC experiments conducted in 0.20 mM and 0.50 mM $[PO_4]_T$ (exp. #8 and #9). This subsequent decrease in adsorption capacity caused by the transformation of ferrihydrite does not result in a re-increase in $[PO_4]$, which would be expected based on data shown in Fig. 2.11, where lepidocrocite exhibits lower scavenging capacity for PO_4-ions compared to ferrihydrite. It is plausible that some formed ferrihydrite (not detectable by the ATR-FTIR technique) remains in the rust phase and contributes to the observed phosphate removal.

Table 3.6. *The surface occupation of Fe(II) and PO_{4T} on ferrihydrite was modeled during the Fe-EC experiments conducted at $[PO_4]_T$ of 0.20 and 0.50 mM (experimental numbers 8 and 9). The model simulation covers the initial 60 minutes of the Fe-EC experiments, during which ferrihydrite formation was observed. The table also includes the model calculation without PO_4. The non-complexed $\equiv$Fe-OH groups available on the surface are indicated as (Fe-OH). These surface complexations were obtained using the 2-site surface complexation model of Dzombak and Morel (1990) with the PHREEQC code. The $c(Fe(III))_{Fh}$ was determined by subtracting the total Fe(II) produced by the Fe-EC process (calculated using equation 2.1) from the spectroscopically determined $[Fe(II)]_T$. The data for $[Fe(II)]_T$ was obtained from Figure 3.4.*

time (min)	Fe(II)$_T$ (%)	PO$_{4T}$ (%)	$\equiv$Fe-OH (%)	Fe(II)$_T$ (%)	$\equiv$Fe-OH (%)
	0.20 mM [PO$_4$]$_T$				
30	3.1	94.2	2.7	14.3	84.9
60	4.6	90.7	4.7	12.8	87.4
	0.50mM [PO$_4$]$_T$				
30	2.5	95.4	2.1	14.3	84.9
60	3.1	94.1	2.7	12.8	87.4
90	4.8	90.3	4.9	17.4	82.6

The Fe(III)/PO$_4$ ratios for the precipitates formed at the 120-minute mark are shown in Fig. 3.5. The Fe(III)/PO$_4$ ratio decreases over this 120-minute period of aerated Fe-EC due to a continuous increase in c(Fe(III)). The Fe(III)/PO$_4$ ratio ranges from 4-20 and 2-8 for the periods when ferrihydrite evolves (first 0-30 minutes and 0-60 minutes in 0.20 mM and 0.50 mM [PO$_4$]$_T$, respectively). This *in-situ* formed ferrihydrite removes 5-10 times the amount of PO$_4$ per generated Fe(III) compared to the ferrihydrite initially produced by Fe-EC in 1 V% H$_2$O$_2$ and then exposed to PO$_4$ (by adding 0.021 mM [PO$_4$]$_T$ to the electrolyte) to enable adsorption (Fe/P = 150 in Fig. 2.10). Such large quantities of PO$_4$-ion removal cannot be explained by adsorption alone, given the limited ≡Fe-OH on ferrihydrite (PO$_4$-removed: [≡Fe-OH] = 3). The high PO$_4$ retaining capacity of freshly formed ferrihydrite aligns with the work of Hiemstra and Zhao (2016), where they found that large quantities of PO$_4$-ions were included into the smallest identified ferrihydrite structure, i.e., Fe$_{20}$-clusters, during the rapid hydrolysis of Fe(III) in the presence of PO$_4$. As adsorption of this nature cannot be explained by surface complexation alone, we presume that the same large inclusion took place.

3.3.4 Ferrihydrite formation in Fe-EC vs. ferrous oxidation.

In these studies, which involved oxidizing [Fe(II)]$_T$ at 1 mM in the presence of 0-2 mM [PO$_4$], an amorphous Fe(III)PO$_4$ (Trincite, Fe$_6$(PO$_4$)$_4$(OH)$_6$·7H$_2$O, Jonasson et al. (1988)) was observed to form as the first precipitate when Fe(III)/PO$_4$ < 1.8. This amorphous phase transforms into P-HFO (hydrous ferric oxide) as the oxidation of Fe(II) continues and the Fe(III)/PO4 reaches the range of 1.8 < Fe(III)/PO$_4$ < 5.3. Complete oxidation of Fe(II) ultimately converts the P-HFO phase into lepidocrocite. It's important to note that the intermediate P-HFO form should not be confused with ferrihydrite, as its structure consists of edge-sharing linkages with monomer and oligomer entities linked to PO$_4$. This structure bears more resemblance to lepidocrocite than ferrihydrite.

The am-Fe(III)PO$_4$ phase exhibits vibration bands at 592, 898, 1008, and 1040 cm^{-1}. However, these bands are absent in the ATR-FTIR (Fig. 3.2), indicating that am-Fe(III)PO$_4$ does not form during the initial stages of the Fe-EC tests, nor does it precipitate onto the surface of ferrihydrite (Wang et al. (2017)). Both ferrihydrite and P-HFO display vibration bands at 600 cm^{-1}, but P-HFO can be distinguished in the ATR-FTIR data by the absence of the 690 cm^{-1} bending vibration modes of Fe-O$_6$ in ferrihydrite (Voegelin et al. (2013)). Although small amounts of P-HFO may be obscured under the band at ~600 cm^{-1}, the dominant presence of

the 690 cm^{-1} bands associated with ferrihydrite indicates that ferrihydrite is the major phase under these conditions.
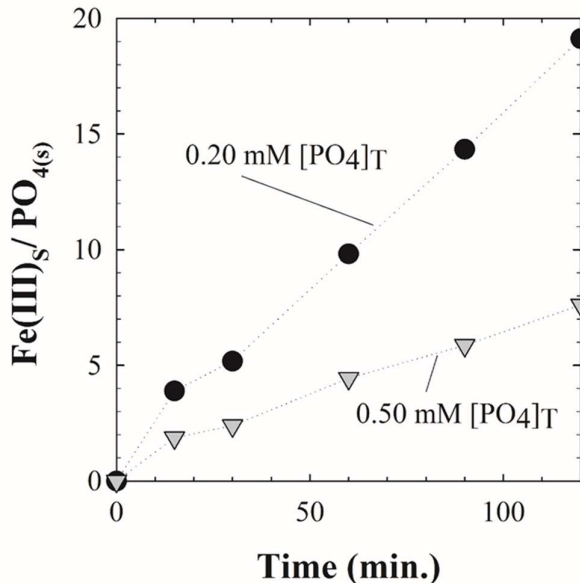

Fig. 3.5. *The molar ratio of Fe(III) to PO$_4$ obtained in the aerated Fe-EC run at pH 7.0 and an electrolyte composition of 0.25M [NaCl]$_T$ with [PO$_4$]$_T$ of 0.20 mM and 0.50 mM [PO$_4$]$_T$, was determined. The experiments were conducted at a current density (J) of 20 A/m^2 and pH 7.0. The electrolyte was mixed using a stirring speed of 750 rpm, which resulted in a high level of electrolyte oxygenation (O$_2$-supply).*

A distinct difference between FeCl$_2$/FeSO$_4$ oxidation studies and the Fe-EC process that may lead to different phase formations is the prevailing Fe(II)$_{aq}$/Fe(III)$_s$ ratios during the oxidation process of Fe(II). In oxidation studies, a starting concentration of FeCl$_2$/FeSO$_4$ is typically oxidized by introducing O$_2$ into the solution, which creates very high prevailing Fe(II)$_{aq}$/Fe(III)$_s$ ratios. The much longer periods used to oxidize all the Fe(II), e.g. t > 80h, retain these high Fe(II)$_{aq}$/Fe(III)$_s$ ratios during the course of the oxidation period (Voegelin et al., (2013); Kraal et al., (2022); Xie et al., (2023)).

For instance, in the methods used by Voegelin (2013) and Kraal et al. (2022), when 10% of the initial 1mM Fe(II) is oxidized in an electrolyte containing [PO$_4$]$_T$ of 1mM, the [Fe(II)] exceeds the [PO$_4$]$_T$, causing a strong competition for the adsorption of PO$_4$-ions on any possibly unnoticed formed ferrihydrite (pH$_{edge}$ is equal for both Fe(II) and PO$_4$) (Choi et al.,

2001; Hie). This makes it hard to produce ferrihydrite due to the presumably fast inception of the Fe(II)-induced transformation of ferrihydrite.

Xie et al. (2023) demonstrated that operating the Fe-EC process by allowing Fe(II) to accumulate in a PO_4-ions solution under deoxygenated conditions and then supplying O_2 to the electrolyte to oxidize the accumulated Fe(II) explicitly forms am-Fe(III)PO_4 and lepidocrocite.

In aerated Fe-EC cells, where the electrochemically generated Fe(II) ions are continuously oxidized by $O_{2(aq)}$, the Fe(II)$_{aq}$/Fe(III)$_s$ ratios will be much lower than in the oxidation studies of Voegelin et al. (2013), Kraal et al. (2022), and Xie et al. (2023) (Fig. 3.4). The adsorption of PO_4-ions is then sufficient to outcompete the binding of Fe(II), substantially reducing the Fe(II)-induced catalytic transformation of the forming ferrihydrite (see Fig. 3.2). This shows that the operating manner of the Fe-EC process in relation to the O_2-supply rates can make a large difference in the way the iron oxyhydroxides form and transform.

3.3.5 Discussion on the formation of lepidocrocite versus goethite from Fe(II)-recrystallization of ferrihydrite.

In previous studies on the reductive transformation catalyzed by Fe(II), it is commonly observed that goethite formation occurs at high [Fe(II)]$_T$/c(Fe(III))$_{Fh}$ or higher c(Fe(III))$_{Fh}$ levels (Boland et al., 2013, 2014; Sheng et al., 2020, 2021; Liu et al., 2023). However, in our findings, we have noticed that higher [CO$_3$]$_T$ (ranging from 5 to 50 mM) delay the transformation of ferrihydrite and increase both c(Fe(III))$_{Fh}$ and [Fe(II)]$_T$/c(Fe(III))$_{Fh}$ to a value greater than 0.2 before ferrihydrite converts into goethite. At first glance, this seems consistent with the observations made in the aforementioned studies. Interestingly, the adsorption of PO_4-ions onto the growing ferrihydrite also causes a delay in its transformation and simultaneously increases [Fe(II)]$_T$/c(Fe(III))$_{Fh}$ and c(Fe(III))$_{Fh}$ (Fig. 3.5). However, in this case, the recrystallization of ferrihydrite surprisingly leads to the formation of lepidocrocite, contradicting the general preference for goethite. This implies that the distinct choice between goethite and lepidocrocite is not solely dependent on [Fe(II)]$_T$/c(Fe(III))$_{Fh}$ or higher c(Fe(III))$_{Fh}$, and that other processes must also play a crucial role in distinguishing between these two minerals.

In section 2.3.4, we have discussed the relationship between goethite and lepidocrocite formation and the difference in pH$_{pzc}$ (point of zero charge) between fresh and aged ferrihydrite. It was found that the adsorption of Fe(II) to aged ferrihydrite with a lower pH$_{pzc}$ than freshly formed ferrihydrite leads to a more reduced E$_{h,surf}$ (surface redox potential), as shown in Figure 2.8. When the E$_{h,surf}$ (-0.15 V) falls below the reduction potential of ferrihydrite

(+0.05 V) and lepidocrocite (-0.05 V), but remains higher than goethite's reduction potential (-0.20 V), the transformation of ferrihydrite into goethite is generally favored over lepidocrocite. These analyses were performed using an electrolyte containing Na_2SO_4, where SO_4^- ions weakly bind to forming ferrihydrite.

The situation is different in $NaHCO_3$- and NaH_2PO_4-electrolytes, as strongly adsorbed CO_3^- or PO_4^- ions can increase the acidity of nearby non-complexed $\equiv$Fe-OH. At small to moderate loadings (e.g. 50% occupation of surface $\equiv$Fe-OH), the adsorption of these anions shifts the pH_{pzc} of ferrihydrite from the original 8.1 to 6.7 (at 50% occupation of surface sites). For example, in Qafoku et al.'s (2020) study, the transformation of ferrihydrite to goethite in the presence of Fe(II) is much faster in $[CO_3]_T$ of 1-10 mM compared to NaCl or Na_2SO_4 electrolytes. However, their results did not attribute this fast transformation to the shift in pH_{pzc} leading to the distinct formation of goethite. Arguably, changes in the surface pH_{pzc} caused by CO_3^- and PO_4^- ions affect the $E_{h,surf}$ and, in turn, the reduction potential of ferrihydrite and lepidocrocite.

In our experiment using a SO_4/CO_3-electrolyte, we employed the PHREEQC program and assumed a pH_{pzc} of 6.7 (assuming 50% surface occupation by CO_3^- ions) for the Fe(II) adsorption to ferrihydrite. We used this assumption to estimate the Fe(II) and CO_3 adsorption and the $E_{h,surf}$ for the Fe(II)-EC test in $[CO_3]_T + [SO_4]_T$ of 25 + 225 mM and 50 + 200 mM. It was found that this shift in pH_{pzc} to 6.7 increased the Fe(II) loading by 10 times compared to the originally predicted Fe(II) loading with a pH_{pzc} of 8.1 (as shown in Table 3.2). The calculated $E_{h,surf}$ was -0.25 V, which was lower than the reduction potential of both ferrihydrite (+0.05 V) and lepidocrocite (-0.10 V) phases (Thamdrup, 2000). This implies that neither phase is stable under these conditions and undergoes reductive dissolution. The predominantly observed formation of goethite indicates that goethite is the stable phase ($E^0_{(goethite)}$ = -0.2 V), and the reductively catalyzed transformation of ferrihydrite to goethite is the predominant reaction.

In experiments conducted using $[CO_3]_T + [SO_4]_T$ of 5 + 245 mM and 10 + 240 mM, the CO_3^- loading on ferrihydrite was much lower compared to higher $[CO_3]_T + [SO_4]_T$. Assuming that the CO_3^- loading on the supposedly formed ferrihydrite at 30 minutes is less than 10% of the total exposed $[\equiv$Fe-OH], the pH_{pzc} is estimated to be around 7.9. In this case, a low Fe(II) loading corresponds to an $E_{h,surf}$ of -0.01 V, which aligns with the reductive dissolution of ferrihydrite. As this $E_{h,surf}$ is higher than the reduction potential of lepidocrocite, reduction dissolution of lepidocrocite does not occur. This demonstrates that lepidocrocite is stable under

$[CO_3]_T + [SO_4]_T$ of 5 + 245 mM and 10 + 240 mM but undergoes reductive dissolution in higher $[CO_3]_T + [SO_4]_T$ of 25 + 225 mM and 50 + 200 mM.

In experiments conducted using $[CO_3]_T + [SO_4]_T$ of 150 + 100 mM and 250 + 0 mM, we observed a higher CO_3- loading on ferrihydrite, which occupied more than 80-90% of the total (Fe-OH). This high CO_3- loading eventually inhibits Fe(II) adsorption and the reductively catalyzed transformation of ferrihydrite.

PO$_4$ adsorption to ferrihydrite creates a similar shift in pH_{pzc} and surface E_h of -0.24 V, as shown in Figure S7 by Mendez and Hiemstra (2019). The surface complexation model simulations revealed that this results in a 10x increase in Fe(II)-loading on the formed ferrihydrite compared to ferrihydrite without adsorbed PO$_4$-ions. The $E_{h,surf}$ is accompanied by the formation of goethite, but goethite was not observed during the recrystallization of ferrihydrite in the Fe-EC test carried out at 0.20 and 0.50 $[PO_4]_T$ (exp. #8 and #9). As the $[PO_4]$ is continuously removed during these tests, with 10% occupancy of exposed [≡Fe-OH] by PO4, the $E_{h,surf}$ decreases to -0.02 V, which is consistent with the reductive dissolution of ferrihydrite and the stability window of lepidocrocite. This indicates that PO$_4$-ions do not necessarily promote goethite formation. However, an important point to consider in the tests with 0.20 and 0.50 mM $[PO_4]_T$ is that the PO$_4$-ions are completely removed from the electrolyte by the formed ferrihydrite after about 30-60 minutes of the Fe-EC run, resulting in an electrolyte depleted in PO$_4$-ions. In comparison to CO_3- and PO$_4$-ions, Cl$^-$ ions form weak outer-sphere complexes with ≡Fe-OH and have a minor impact on the pH_{pzc} of ferrihydrite. Therefore, the ferrihydrite formed after this removal likely has a pH_{pzc} that is similar to fresh ferrihydrite (i.e., 8.1 according to Jain et al. (1999)), and due to a relatively lower [(Fe-O-Fe(II))/[(Fe-OH)] ratio, the calculated $E_{h,surf}$ is only -0.08 V, which agrees with the observation that ferrihydrite undergoes a reduction transformation to lepidocrocite. Higher $[PO_4]_T$ were not tested as this could lead to the predominant formation of vivianite (Wang et al., (2019)) and am-Fe(III)PO$_4$ (Voegelin et al., (2013); Sleimann et al., (2016)). In the tests with carbonate, the $[CO_3]_T$ remains constant throughout the 120-minute Fe-EC run, as the formed phases remove only < 1% of $[CO_3]_T$. Therefore, there is a constant drive for CO_3- ion adsorption onto the continuously formed fresh ferrihydrite, which likely maintains the shifts in pH_{pzc} on the forming ferrihydrite and creates a more negative $E_{h,surf}$ compared to pristine ferrihydrite, promoting the formation of goethite through the reductive dissolution of ferrihydrite.

In addition to this, there could be a potential relationship drawn between labile Fe(III) complexation with PO$_4$- and CO$_3$- ions. As mentioned earlier, in $[CO_3]_T + [SO_4]_T$ electrolyte, labile Fe(III) can form Fe(OH)CO$_3$ complexes, while labile Fe(III) forms weak complexes with

$[PO_4]_T + [Cl]_T$. Aqueous complexation can influence the crystallization of labile Fe(III), as shown by the work of Sheng et al. (2020b). They demonstrated that a higher citrate content in the reactive medium leads to the formation of more labile Fe(III)-citrate complexes, which consequently reduces the rate of labile crystallization to lepidocrocite or goethite. However, they observed that a higher citrate-labile Fe(III) favors the formation of lepidocrocite over goethite. They explained this as a difference in supersaturation levels, which leads to the formation of goethite or lepidocrocite nuclei on the surface of ferrihydrite. Considering that $Fe(OH)CO_3$ complexes lower the labile [Fe(III)], it can be argued that $[CO_3]_T + [SO_4]_T$ should lead to more lepidocrocite than goethite formation, but we observe the opposite. This suggests that the surface charge effects on the pH_{pzc} and $E_{h,elec}$, as described above, are more determining factors for the distinct formation of goethite vs. lepidocrocite nuclei on ferrihydrite's surface. However, it is unclear whether $Fe(OH)CO_3$ complexes have influenced the crystallization of Fe(III) in favor of goethite, like the suggested complexation of CO_3 ions onto tetrameric units which favors goethite formation (Rose et al., 1997). Therefore, it is suggested to study the formation and consumption rate of labile Fe(III) in electrolyte containing CO_3 ions.

Earlier, we indicated in a previous experiment ($[SO_4]_T$ of 250 mM, as shown in Figure 2.2 in Chapter 3.3.1) that ferrihydrite forms and transforms into lepidocrocite. However, in a subsequent experiment with a $[CO_3]_T$ of 5 mM (+245 mM $[SO_4]_T$), we did not observe any ferrihydrite formation. This suggests that ferrihydrite forms and transforms more rapidly in the presence of a $[CO_3]_T$ of 5 mM (+245 mM $[SO_4]_T$) compared to a 250 mM $[SO_4]_T$ Additionally, the presence of CO_3- ions enhances the catalytic transformation of ferrihydrite. Qafoku et al. (2019) demonstrated a similar phenomenon, where the transformation of ferrihydrite was accelerated by the presence of small quantities of $[CO_3]_T$ (in $NaHCO_3/Na_2CO_3$-buffer). They attributed this to the increased Fe(II)-loading resulting from the pH_{pzc} shift (< 8.1) caused by the adsorbed CO_3- ions, enabling greater electron transfer rates between Fe(II) and ferrihydrite. However, it is not clear why goethite is formed instead of lepidocrocite. It can be presumed that the adsorption of CO_3- ions in the experiment with 5 mM $[CO_3]_T$ is not significant enough to accelerate the transformation to goethite. It is possible that the $E_{h,surf}$ has only reached the reduction potential required for lepidocrocite formation and not goethite. In experiments with slightly higher $[CO_3]_T$ of 10 mM (+240 mM $[SO_4]_T$), more goethite formation is observed compared to lepidocrocite. This suggests that a higher CO_3-loading increases the Fe(II)-loading and reduces the $E_{h,surf}$ sufficiently to surpass the reduction potential required for lepidocrocite, leading to goethite formation. As shown in our results, goethite is observed towards the end of the experiment, and it appears to evolve from lepidocrocite recrystallization rather than directly

from ferrihydrite, which is no longer observed when lepidocrocite begins to transform into goethite. Similar to ferrihydrite, lepidocrocite can also undergo a reductive transformation to goethite, as demonstrated in studies by Sheng et al. (2021) and Boland et al. (2014). In this case, adsorbed CO_3- ions may have similarly reduced the $pH_{pzc, Lp}$ (< 7.1) and increased the Fe(II)-loading in lepidocrocite, driving its reductive transformation.

3.4. Conclusions and implications to wastewater treatment with the Fe-EC process.

The formation and productivity of ferrihydrite through the aerated Fe-EC process were studied in the presence of PO_4- and CO_3-ions in an electrolyte medium containing NaCl and Na_2SO_4, respectively. Ferrihydrite was found to evolve during the aerated Fe-EC process, regardless of the type of anions present. However, its further transformation into lepidocrocite or goethite was influenced by the [Fe(II)], $[PO_4]_T$ and $[CO_3]_T$. Both PO_4 and CO_3 ions, with PO_4 being more effective, promoted the formation of ferrihydrite by facilitating the reductive transformation under high [Fe(II)] conditions. This effect was attributed to the strong adsorption of these anions to the surface sites (Fe-OH) of ferrihydrite, which reduced the adsorption of Fe(II) and inhibited its reductive transformation. The inhibitory effect was correlated to the $[CO_3]_T$ and $[PO_4]_T$: higher values of $[CO_3]_T$ and $[PO_4]_T$ (<50 mM) led to stronger inhibitory effects on the reductive transformation of ferrihydrite due to increased adsorption. In an electrolyte containing $[CO_3]_T+[SO_4]_T$ of 150+100 and $[CO_3]_T$ of 250 mM, large quantities of adsorbed CO_3 ions fully inhibited the catalytic transformation of ferrihydrite, resulting in continuous ferrihydrite production throughout the 120-minute Fe-EC test run. In the Fe-EC tests conducted with $20 \leq [PO_4]_T \leq 50$ mM, ferrihydrite formation was observed, but it did not occur continuously as ferrihydrite transformed into lepidocrocite. Testing $[PO_4]_T >$ 50 mM was not possible to avoid the formation of other PO_4-bearing phases such as vivianite, am-Fe(III)PO_4, and P-HFO.

Furthermore, reasonable evidence has been found indicating that when moderate amounts of CO_3 are loaded (e.g. 50% occupation of total (Fe-OH) to ferrihydrite), it promotes the formation of goethite instead of lepidocrocite. This is attributed to a shift in the pH_{pzc}, which is below 8.1, leading to increased Fe(II)-loading and the creation of a more reduced $E_{h,surf}$ (i.e. below 0.20V), which favors the formation of goethite. In addition, the presence of PO_4 ions in

the electrolyte containing NaCl inhibits this shift in pH_{pzc} as more Fe/PO_4 is added. As a result, in the NaCl electrolyte, the $E_{h,surf}$ of the formed ferrihydrite is below the reduction potential of ferrihydrite but above that of lepidocrocite. Consequently, the transformation of ferrihydrite mainly proceeds towards the lepidocrocite phase.

The finding that ferrihydrite forms during Fe-EC has major implications for the application of Fe-EC to wastewater treatment. Higher removal yields of heavy metals such as Zn(II), Ni(II), Cd(II), Cr(VI), and hazardous anions such as As(III,V) and Se(VI,IV) have often been reported with ferrihydrite (Das et al. (2013) for Se(IV,VI) and Zhao et al. (2011) for As(III,IV)), partly mediated by the pH_{pzc} shift due to partial anion adsorption and the formation of tertiary complexes. For instance, a tertiary complex can form between Zn(II) and PO_4 onto ferrihydrite (Van Eynde (2022)). Ferrihydrite has also been observed in the presence of anions such as Cr(VI) (Pan et al. 2017) or arsenates (As(VI), As(III)) (Maldonado-Reyes et al. (2015), Syam Babu et al. (2021)). The redox-active Se(VI) is even more effectively removed by reduction to Se(IV) (or even Se(0)) in Fe(II)-ferrihydrite systems, even when ferrihydrite is transformed into goethite (Wang et al. (2020)). However, this is not the case for the removal of Zn(II), where the recrystallization of ferrihydrite into lepidocrocite and goethite (Fig. 3.2) induced by Fe(II) reduces the adsorption capacity of the rust phase (Yang et al. 2022). This also applies to the removal of PO_4, whereby more PO_4 is removed with ferrihydrite per generated Fe(III) than with lepidocrocite and goethite (Nguyen et al. (2017), Xie et al. (2023)). Therefore, the presence of PO_4- and CO_3- ions in wastewater treated with the Fe-EC process can help increase the productivity of ferrihydrite and, consequently, enhance the removal of heavy metals. Moreover, the adsorption of these anions shifts the pH_{pzc} of ferrihydrite in favor of cation binding (Mendez and Hiemstra (2019)).

In wastewater treatment, the objective is always to efficiently remove PO_4 below the prescribed discharge limits (< 1.0 mg/L for WWTPs in the Netherlands) by using the lowest possible dose of Fe(III), in order to minimize treatment costs. The resulting sludge is mostly disposed of in landfill areas, where it is stored for several years under controlled conditions. The mobilization of PO_4 can lead to eutrophication if it enters the surrounding environment. Therefore, it is crucial to ensure that the post-mobilization of PO_4-ions does not occur during storage. As demonstrated by the results presented here, freshly formed ferrihydrite effectively removes P (12-25 mol%) to the same extent as the P content in P-HFO, which can contain 5-20 mol% P (Kraal et al., (2022)). Rust generated through the Fe-EC process, such as am-Fe(III)PO$_4$ and lepidocrocite (Xie et al., (2023)), also achieves efficient removal of P with a capacity of 44.5 mg P/g Fe (Fe(III)/PO$_4$ of 12, P/Fe = 0.08). The removal efficiency is

comparable to the direct removal of PO$_4$-ions through the *in-situ* application of Fe-EC, although the rust phases were not characterized (Nguyen et al., (2017)). However, both am(Fe(III)PO$_4$ and P-HFO are prone to rapid recrystallization to lepidocrocite (Kraal et al., (2022)). In this regard, ferrihydrite is more stable in the presence of PO$_4$ (Hiemstra and Zhao, (2016)), and it is often observed to minimize the immobilization of PO$_4$ under soil conditions. Therefore, removing PO$_4$ using ferrihydrite might be a better option compared to the removal driven by the formation of am(Fe(III)PO$_4$ and P-HFO. However, as indicated in this study, PO$_4$-rich ferrihydrite transforms into lepidocrocite under higher concentrations of Fe(II). As shown in Chapter 2, increasing the O$_{2(aq)}$ concentration reduces the reductive transformation of ferrihydrite by minimizing the accumulation of Fe(II) in the electrolyte. Though not presented in this study, one potential approach to mitigate the transformation of PO$_4$-rich ferrihydrite is to enhance aeration through techniques such as vigorous mixing or the addition of strong oxidants like H$_2$O$_2$.

References.

Aeppli M, Kaegi R, Kretzschmar R, Voegelin A, Hofstetter TB, Sander M, Env. Sci. & Tech 53 (7), **2019**, 53, 7, 3568-3578.

Al-Zghoul; Al-Jamrah, Z. Al-Qodah 2,* and Ahmad Al-Jamrah Wastewater. *Water* **2023**, 15, 980.

Amaral S.T.; I. L. Muller, *Corrosion Science* **1999,** 41, (4), 747-758.

Blesa M.A., Matijevic E., *Advances in Colloid and Interface Science* **1989,** 29, (3-4), 173-221.

Hansel C.M., Benner S.G., Fendorf S., *Environmental Science & Technology* **2005,** 39, (18), 7147-7153.

Choi S.; Hong S.; Ahn K., Baumann E.R, *Environmental Science of Technology,* **2001,** 22, (5), 355-365.

Cudennec Y.; Lecerf A., *Journal of Solid State Chemistry* **2006,** 179, (3), 716-722.

Das S., Hendry M.J., Essilfie-Dughan J., *Applied Geochemistry*, **2013**, 28, 185-193

Deng Y.W., *Water Research* **1997,** 31, (6), 1347-1354.

Dutrizac, J.E. *Cim Bulletin* **1987,** 80, (903), 94-94.

Dzombak D.A., Morel F.M.M., *Surface complexation modelling, hydrous ferric oxide,* John Wiley and Sons, **1990**

Ebba M., Asaithambi P, Alemayehu E, *Applied Water Science* , **2021**, 11, 175

El-Naggar M.M., *Applied Surface Science* **2006,** 252, (18), 6179-6194.

Hiemstra T., Mendez J.C., Li J., *Environ. Sci.: Nano*, **2019**, (3), 820-833.

Hiemstra T. and Zhao W., *Environ. Sci.: Nano*, **2016**, 3, 1265-1279

Guo H., Li Y., Zhao K., Ren Y., Wei C. *J Hazard Mater.*, **2011**, 186(2-3), 1847-54.

Jolivet J.P.; Tronc E.; Chaneac C., *Comptes Rendus Geoscience* **2006,** 338, (6-7), 488-497.

Jonasson R.G., Martin R.R., Giuliacci M.E. and Tazaki K., *J. Chem. Soc., Faraday Trans*., **1988**, 84, 2311–2315.

Kiyama M.; Takada T.; Shimizu S.; Okuda Y.; Akita T., *Bull. Chem. Soc. Japan* **1972**, 45, (11), 3422-&.

Kim D-G, Palacios R.J.S., Ko S-H, *Desalination and Water Treatment* , **2014**, 52, 4-6

Latta D., KM Rosso K.M., Scherer M.M., *ACS earth and space chemistry*, **2023**, 7, 10, 1814-1824

Lee K., Clydesdale F.M., *Journal of Food Science* **1979,** 44, (2), 549-554.

Legrand L. Mazerolles L., Chaussé A, *Geochim. Et Cosmoch*. 2004, 68, 17, 3497-3507

Li Y., Zhang C, Meijun Yang M., He H., Arai Y. Geoderma, 2022, 115811

Liu Y., Ding Y., Sheng A., Li X., Chen J., Arai Y., Liu J., *Environmental Sci. & Tech*., **2023**, 57 (17), 6934-6943

Liu H., Li P., M. Y. Zhu M.Y., Y. Wei Y., Sun Y.H., *J. of Solid State Chemistry* **2007,** 180, (7), 2121-2128.

Lu X, Xu T, Zhou Y, Peng Q, Ou J, Hu B, Xie Z, Lei X, Yu G. *J. Env. Sci.* **2023**, 124, 823-834

Maldonado-Reyes A, Montero-Ocampo C. Medina-Garcia J., Bolado-Rodríguez S. Alvárez-Benedí J., Herrera-Vazquez A., Castaño V.M. *Water Air Soil Pollut*, **2015**, 226: 249

Mendez J.C. and Hiemstra T., *ACS Earth Space Chem.* **2019**, 3, 1, 129–141

Millero F.J.; Sotolongo S.T.; Izaguirre M., *Geochimica Et Cosmochimica Acta* **1987,** 51, (4), 793-801.

Misawa T. ; Hashimoto K.; Shimodai.S, *Corrosion Science* **1974,** 14, (2), 131-149.

Mishima I, Hama M, Tabata Y. Nakajima *J. Water Sci Technol* , **2018** 78 (6): 1304–1311.

Morgan B., Lahav O., *Chemosphere* **2007,** 68, (11), 2080-2084.

Mukesh K.; Y. D. Panday, *Environmental Technology* **2001,** 22, (2), 137-150.

Music S.; Gotic M.; Popovic S., *Journal of Materials Science* **1993,** 28, (21), 5744-5752.

Oh S.J., Kwon S.J., Lee J.Y., Yoo J.Y, Choo W.Y., *Corrosion* **2002,** 58, (6), 498-504.

Oh S.J.; Cook D.C; Townsend H.E., *Hyperfine Interactions* **1998,** 112, (1-4), 59-65.

Pan C, Troyer L.D., Liao P., Catalano J.F., Li W., Giammar D.E., *Environ. Sci. Technol.* **2017**, 51, 11, 6308–6318

Park U., Dempsey B.A., *Environmental Science and Technology* **2005,** 39, (3-4), 6494-6500.

Pedersen H.D., Postma D., Jakobsen R., Larsen O., *Geoch. Et Cosmochim. Acta* **2005,** 69, (16), 3967-3977.

Persson P., Lovgren L., *Geochimica Et Cosmochimica Acta* **1996,** 60, (15), 2789-2799.

Qafoku O, Kovarikb L, Bowdena M.E. Nakouzib E, Sheng A, Liuc J, Pearce C.A., Rosso K.M., *Environmental science*, *Nano*., **2020** 7 (10). 2020.

Rose J., Flank A.-M., Masion A., Bottero J.-V., Elmerich P., Langmuir **1997**, 13, 6, 1827–1834

Ruan H.D.; Frost R. L., Kloprogge J.T.; Duong L., *Spectrochi. Acta Part a-Mol. And Biomol. Spec.* **2002,** 58, (5), 967-981.

Schwertmann U., Stanjek H. Becher H.H., *Clay Minerals*, **2004**, 39 (4),433-438

Schwertmann U., Cornell R.M., *Iron oxides in the laboratory*, 2nd edition, Wiley-VCH, New York, **2000**, XV.

Schwertmann U., Friedl J., Stanjek H., *Journal of Colloid and Interface Science* **1999,** 209, (1), 215-223.

Schwertmann U., *Plant and Soil* **1991,** 130, (1-2), 1-25

Schwertmann U.; Taylor R.M., *Clays and Clay Minerals*, **1972**, 20, 151-158.

Sheng A., Liu J., Li X., Qafoku O., Collins R.N., Jones A.M., Pearce C.I., Wang C., *Geoch. et Cosmochima Acta* **2020a**, 272, 105-120

Sheng A., Li X., Arai Y., Ding Y., Rosso K.M., Liu J., Env. Sci. & Tech., **2020b**, 54 (12), 7309-7319

Sheng A, Liu J., Li X., Luo L., Ding Y., Chen C., Zhang X., Wang C., Rosso K.M., *Geoch. et Cosmochimica Acta*, **2021**, 309, 272-285

Sleiman N., Deluchat V., Wazne M., Courtin A., Saad Z., Kazpard, *RSC Adv*., **2016**,6,162

Stumm W.; Lee G.F., *Industrial and Engineering Chemistry* **1961,** 53, (2), 143-146.

Syam Babu D., Vijay K, Nidheesh P.V., Suresh Kumar M., *Sust. Energy Tech. and Assessments* **2021** 47, 101476

Tamura H, Goto K, Nagayama M., *Corrosion Science* **1976,** 16, (3-4), 197-207.

Tejedor-tejedor M.I., Anderson M.A., *Langmuir* **1986,** 2, (2), 203-210.

Tiberg C., Sjostedt C. , Persson I., Gustafsson J.P., *Geochim. Cosmochim. Acta*, **2013**, 120 ,140–157.

Tronc E., Belleville T., Jolivet J.P., Livage J., *Langmuir* **1992,** 8, (1), 313-319.

Van Eynde E., Hiemstra T., Comans R.N.J. Geochimica et Cosmochimica Acta, 2022, 320, 1, 223-237

Van Genuchten C.M., Behrends T., Kraal P., Stipp S.L.S, Dideriksen K., *Electrochimica Acta*, **2018**, 286, 324-338

Van Genuchten C.M., Pena J., Amrose S.E., Gadgil A.J., Geoch. et Cosmochim. Acta, **2014**, 127, 285–304

Villalobos, M.; Leckie, J. O. *J. Colloid Interface Sci.* 2001, 235 (1), 15−32.

Wang R. Wilfert P, Dugulan I., Goubitz K., Korving L., Witkamp G-.J., Van Loosdrecht M.C.M., *Sep. and Purific. Tech.*, **2019**, 220, 126-135

Wang S, Lei L, Zhang D, Zhang G, Cao R., Wang X., Lin J, Jia Y., *J. Hazardous Materials*, **2020**, 384, 121365

Weckler B.; Lutz H.D, *European Journal of Solid State and Inorganic Chemistry* **1998,** 35, (8-9), 531-544.

Wijnja, H.; Schulthess, *Soil Sci. Soc. Am.* J. 2001, 65 (2), 324−330.

Xu L, Xu X, Cao G, Liu G, Duan Z, Song S, Song M, Zhang M. *J. Env. Management* **2018**, 218, 129-138

Xie S, Bai Z, Shao W, Wang C, Qin J., Liu Z. Liao P. *Environ. Sci.: Adv*., **2023**, 2, 898-907

Yang Y, Li Y., Mao R., Shi Y., Lin S., Qiao M., Zhao X, *Sep. Purif. Technol*., **2022**, 286, 120439.

Yu W., Cao Y., Yan S., Guo H. *Sc. Of Total Environment*, **2023**, 882, 163556

Zhao Z., Jia Y., Xu L., Zhao S., *Water Research*, **2011**, 45, 19, 6496-6504

Zhang Y; Charlet C.; Schindler Y.W., *Colloids and Surfaces* **1992,** 63, (3-4), 259-268.

4

Near electrode effects of the Fe-EC process on rust formation: catalyzed transformation of lepidocrocite to goethite by Fe(II)-ions in alkaline conditions.

Abstract. Lepidocrocite (γ-FeOOH), with its higher sorption capacity, is preferred as an adsorbent for contaminants compared to goethite (α-FeOOH). Producing lepidocrocite through the iron electro-coagulation (Fe-EC) process, as opposed to goethite, results in lower sludge production and reduced material/energy consumption. However, in the Fe-EC process, the creation of alkaline regions (> pH 7) on the cathode surface and the incomplete oxidation of Fe(II) levels during high current Fe-EC cell operations (> 1 A/m^2) have the potential to significantly enhance the transformation rate through a catalytic process. It was observed that in a 1M NaOH and Fe(II) solution, the transformation rate from lepidocrocite to goethite was catalyzed by Fe(II), transforming it within 4-10 hours with a Fe(II)/Fe(III) ratio of 1-10 (1-10 mM [Fe(II)]$_T$ in solution, 1 mM of Fe(III) in the solid lepidocrocite phase), compared to a conversion period of over 1 year at pH 7.0 and room temperature. This catalytic process was attributed to the combined effects of Fe(OH)$_2$ acting as seeds for goethite nucleation and the reductively-driven dissolution of lepidocrocite through a surface electron transfer reaction between Fe(II) and lepidocrocite, potentially forming an intermediate conductive phase upon Fe(II) co-precipitation on the lepidocrocite phase. Higher temperatures (40-80 °C) decrease this catalytically-driven transformation rate by increasing the solubility of Fe(OH)$_2$ seeds and reducing the formation of an intermediate conductive phase. In lower concentrations of NaOH (0.01 and 0.1), the electron transfer reactions occur at a faster rate than the reductive dissolution of lepidocrocite, resulting in a larger accumulation rate of Fe(II) on lepidocrocite. In these cases, the co-precipitation of Fe(II) and Fe(III) to magnetite (Fe$_3$O$_4$) dominates over the dissolution and reprecipitation pathway to goethite.

4.1.   Introduction

Iron electro-coagulation (Fe-EC) is a widely researched water treatment technology for removing trace pollutants like As, Cu, Cd, Cr, Se (Moreno et al., 2007) from wastewater. It is an easily integrable technology into existing wastewater treatment facilities and has proven effective for treating various types of wastewater from industrial and domestic sources. Removal is typically achieved by utilizing in-situ generated iron oxyhydroxides (Mollah et al., (2001); Mollah et al., (2004)). The removal process involves adsorption, co-precipitation, coagulation, and the structural incorporation of the pollutant into the iron oxyhydroxide structure. Oxyhydroxides are produced through the electrolytic oxidation of Fe(0) to Fe(III), or through a two-step process involving the electrolytic oxidation of Fe(0) to Fe(II), followed by the aqueous oxidation of Fe(II) by introducing dissolved oxygen, $O_{2(aq)}$, into the wastewater to oxidize Fe(II) into Fe(III). In general, the $[O_{2(aq)}]$ is not sufficient in water conditions to accompany the current density usually applied for Fe-EC, so aeration is typically required (eq. 1.1-1.12). As the direct oxidation of Fe(0) to Fe(III) is nearly impossible, and Fe(II) is predominantly formed, aeration is usually necessary during wastewater treatment.

In general, the cost of treatment, sludge production and handling, and the successful and efficient removal of pollutants depend on the type of iron oxyhydroxide produced during the Fe-EC application process for treating wastewater. It is crucial to control the speciation of iron oxyhydroxide in wastewater treatment, as it exists in various forms. The most commonly observed and characterized iron oxyhydroxide products in aerated Fe-EC are ferrihydrite ($Fe_5O_7OH.5H_2O$), lepidocrocite (γ-FeOOH), and goethite (α-FeOOH) (Oh et al., (2002)) (Van Genuchten et al., (2014, 2018)). These products have different adsorption capacities, with ferrihydrite having the highest capacity, followed by lepidocrocite and then goethite (Cornell and Schwertmann, (2003); Das et al., (2013)). The speciation of iron oxyhydroxide phases formed through the precipitation of Fe(II) and Fe(III) during Fe-EC determines the required Fe dosage for pollutant removal. Ferrihydrite, due to its high adsorption capacity per unit of Fe(III) generated, is the preferred corrosion product for removing pollutants with the lowest possible Fe dosage, in order to minimize electricity and material consumption, as well as sludge handling. However, as discussed in chapters 2 and 3, the production of ferrihydrite is hindered by its fast transformation to lepidocrocite. Ferrihydrite production is established under highly oxygenated conditions (H_2O_2) or in the presence of inhibiting anions such as PO_4 and CO_3 (Chapter 2 and 3). Lepidocrocite is generally the observed phase and is preferred over goethite

due to its higher specific surface area (80-150 m^2/g compared to 15-60 m^2/g for goethite). This chapter focuses on these two phases due to their abundance in rust formation.

Lepidocrocite is thermodynamically less stable than goethite and therefore tends to transform into goethite over time. Under circumneutral conditions (pH 7.0 and room temperature), the aging period of lepidocrocite is very slow, with 80% transformation taking more than 1 year (Schwertmann and Taylor, (1972)). In wastewater treatment using Fe-EC (iron electrocoagulation) systems, where the reaction time between iron oxyhydroxides and pollutants spans a few hours (0-20h), it may initially seem unlikely for lepidocrocite to undergo transformation during Fe-EC treatment. However, what makes Fe-EC systems unique is the possibility of elevated Fe(II) levels existing during operation. This can occur when Fe(II) is not fully oxidized by $O_{2(aq)}$ or when Fe(III) (in the form of oxyhydroxides or Fe(III)-ions) is reduced at the cathode, such as through reductive dissolution of lepidocrocite (Legrand, (2005)). Reductive dissolution driven by Fe(II)-ions has been observed under acidic (pH 2-3, 50 K) and neutral pH conditions, with a shorter transformation period of 2-5 days (Bechine et al., (1982); Cornell et al., (1989); Ishikawa et al., (2005); Boland et al., (2013, 2014); Sheng et al., (2020, 2021); Liu et al., (2023)), compared to the longer period observed by Schwertmann and Taylor (1972). Despite this, the transformation period of lepidocrocite in Fe-EC operations, occurring within 0-20h reaction time, is still shorter than the observed transformation period under these conditions. The role of OH$^-$ ions evolution (along with H_2 gas) at the cathode (eq. 1.2) has not been considered to have an impact on the transformation period. However, it is worth noting that local pH levels near the cathode surface can range between 9 and 12 (Deligiani and Romankiw, (1993); Deslouis et al., (1997)), and in some cases, can even reach levels exceeding 15 (Honda et al., (1998)). These high pH levels have been shown to be capable of transforming lepidocrocite to goethite in approximately 30 hours at 1M KOH and high temperatures, even though wastewater treatments are typically carried out at room temperature. Additionally, it should be considered that Fe(II) can exist near these alkaline conditions, which could potentially impact the transformation of lepidocrocite to goethite. In wastewater streams, the use of stacked Fe-EC cells with large electrode surface areas for industrial wastewater treatment can increase the residence period of lepidocrocite near these alkaline regions (Mao et al., 2023). At alkaline conditions, reactions between Fe(II) and lepidocrocite have been observed to transform lepidocrocite into magnetite (Fe_3O_4), which contains a mixture of Fe(II) and Fe(III) in a 1:2 ratio (eq. 1.9). However, at very alkaline conditions (0.1-5M NaOH), Traina and He (2015) observed that magnetite becomes undersaturated and transforms into goethite, suggesting that magnetite formation is hindered under very alkaline conditions, similar to those

92

near the cathode surface during Fe-EC process operation. The role of Fe(II) in accelerating the transformation of lepidocrocite to goethite under locally high pH conditions is not well understood, but it is essential to investigate these unknown processes in order to improve the efficiency of Fe-EC application for wastewater treatment. In this study, the transformation of lepidocrocite into goethite was investigated at various Fe(II) concentrations (ranging from 1.0 to 10.0 mM), different temperatures (ranging from 20 to 80 °C), and with varying sodium hydroxide concentrations (0.01, 0.1, and 1.0M).

4.2. Experimental

4.2.1. Lepidocrocite synthesis

Lepidocrocite particles are produced following the recipe described in Schwertmann and Cornell (2000). $FeCl_2.4H_2O$ salts were added to a deionized Milli-Q solution and quickly adjusted to a pH range of 6.5-7. The pH of the solution was maintained within this range by titrating with 1 M HCl and 1 M NaOH. In order to prevent goethite formation and allow for significant oxidation of the Fe(II) ions, air was bubbled through the solution. This also prevented CO_2 from entering the system. Prior to bubbling air through the solution, it was purged with a 5 M NaOH solution to remove any CO_2. The final concentration of (solid) Fe(III) in this lepidocrocite suspension was set at 20 mM, with a background electrolyte concentration of 40 mM NaCl.

4.2.2. Lepidocrocite transformation experiments

2 mL (100 μmol of Fe(III)) of the lepidocrocite suspension were mixed with various quantities of 5M NaOH solutions. Water was then added to the volumes indicated in Table 4.1. These mixtures were prepared in 100 mL plastic vessels with a septum. The suspensions were purged with a H_2/N_2 mixture (5/95%) for 2 hours to remove all dissolved O_2. Next, a solution containing 50 mM Fe(II) ($FeCl_2.4H_2O$) was prepared under acidic conditions and a N_2 atmosphere. Different volumes of this solution were then added to the lepidocrocite suspension using a syringe, resulting in c(Fe(II)):c(Fe(III)) ratios of 1mM:1mM, 2mM:1mM, 5mM:1mM, and 10mM:1mM (as shown in Table 4.1). Additional tests were performed using a 1mM:1mM ratio, but at [NaOH] of 0.1M, 0.01M, and 0.001M. The total volume of the reaction mixture was maintained at 100 ml. Throughout the text, $[Fe(II)]_T$ refers to the total initial concentration of Fe(II)-species in the system, as does [Fe(III)] for Fe(III)-complexes, solids, and liquids. The

experiment at 1mM:1mM was replicated at temperatures of 40°C, 60°C, and 80°C using a water bath. Samples were taken at different time intervals and filtered through 0.2 μm membrane filters under a N_2 blanket. The filtrate was thoroughly washed with deionized, deoxygenated water and dried under a N_2 blanket. ATR-FTIR spectra were obtained from the precipitates using a Shimadzu 4800-SN within the wavenumber range of 500 to 4000 cm-1. The lepidocrocite to goethite ratios were determined from these spectra using the Gaussian fitting procedure to analyze the peak area associated with the lepidocrocite to goethite ratio. For the experiment conducted at 20°C with a Fe(II):Fe(III) ratio of 1, additional XRD analysis was performed. The same solid samples were further analyzed using a scanning electron microscope (JEOL JSM-6480 LV) and through visual observation. The colors of the solution and solid materials were identified using the color plates described in Schwertmann and Cornell (2000).

Tab. 4.1. *The volumetric mixtures of Fe(II), Fe(III), (5M) NaOH and H_2O used for the lepidocrocite conversion experiments.*

Exp. Fe(II):Fe(III)	V(Fe(III))* (ml)	V(Fe(II))** (ml)	V(5M NaOH) (ml)	V(H_2O) (ml)	T (°C)
1:1	2	2	20	76	20
2:1	2	4	20	74	20
5:1	2	10	20	68	20
10:1	2	20	20	58	20
1:1	2	2	2	94	40
1:1	2	2	2	94	60
1:1	2	2	2	94	80
1.1	2	2	0.2	75.8	20
1:1	2	2	0.02	76	20

*as 50 mM Fe(III) suspension in lepidocrocite form)

**acidic 50 mM $FeCl_2$-solution

4.3. Results

4.3.1. Effect of Fe(II)

Throughout the text, $[Fe(II)]_T$ refers to the total initial concentration of Fe(II) species in the system, as well as for Fe(III) (complexes, solids, liquids). The XRD spectra of the suspensions

before and after aging for 10 hours at 20 °C in 1M $[NaOH]_T$ in the presence of $[Fe(II)]_T =$ $[Fe(III)]_T = 1.0$ mM are shown in Figure 4.1. It is evident that lepidocrocite was completely transformed into pure goethite within 10 hours. This transformation occurred approximately 520 times faster than the full transformation period (>5200 hours) in the absence of Fe(II) (as reported by Schwertmann and Taylor (1972). There were no indications of co-precipitation of Fe(II) and Fe(III) into magnetite, which would have occurred if the structural incorporation of Fe(II) into lepidocrocite had taken place. This suggests that Fe(II) at most acts only as a catalyst for the lepidocrocite to goethite transformation.
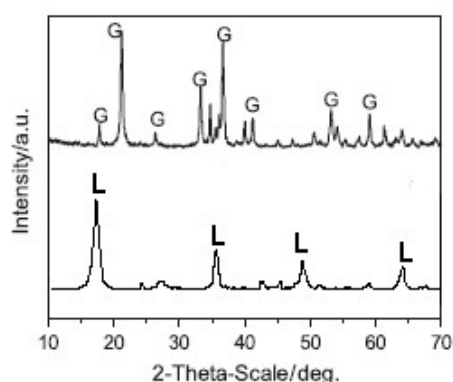
Fig. 4.1. *XRD of the solid phases obtained from a lepidocrocite suspension aged at 20 °C, 1.0M $[NaOH]_T$ and ($[Fe(II)]_T = [Fe(III)]_T = 1.0$ mM). Upper: 10h and lower: 0h. The peaks of lepidocrocite and goethite phases are denoted by L or G resp.*

The ATR-FTIR spectra obtained at different points in time verify this transformation (Fig. 4.2, n(Fe(II)): n(Fe(II)) = 1). The bending vibrations of $(Fe^{3+}-)O-H$ groups at 580, 746, and 1020 cm^{-1} (represented as L in Fig. 4.2) indicate the presence of pure lepidocrocite (Weckler and Lutz, (1998)) in the early stage. The transformation of lepidocrocite over time can be observed by the gradual reduction of the peak at 746 and 1020 cm^{-1} and the emergence of the bending vibration of goethite at 612, 789, and 880 cm^{-1} (represented as G in Fig. 4.2) (Persson et al. (1996), Ruan et al. (2002)). In the absence of Fe(II), only a minor transformation occurred within 10 hours (Fig. 4.2, Fe(II) = 0), supporting the catalytic role of Fe(II).
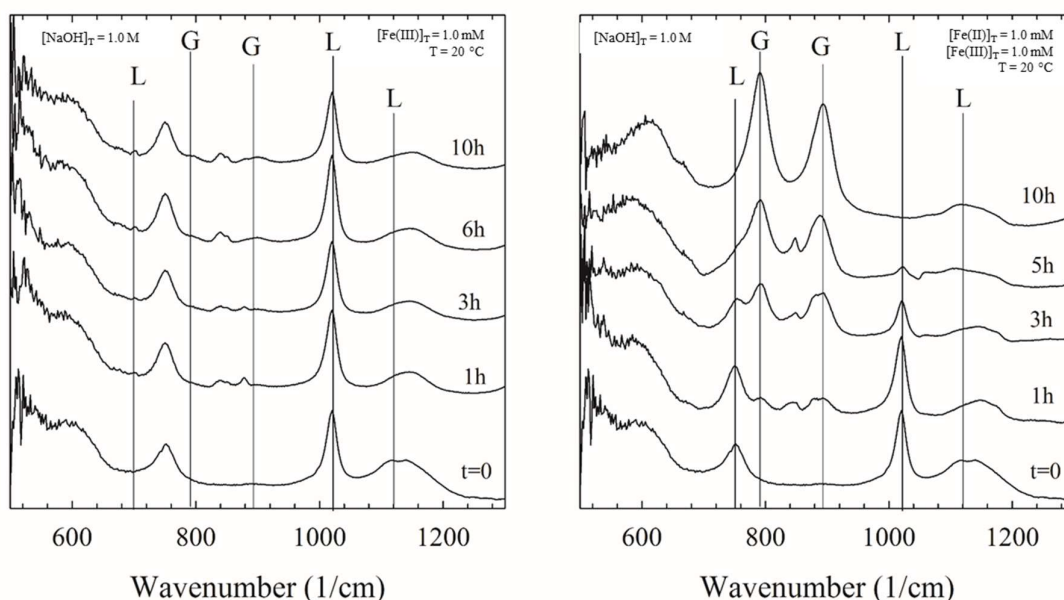
Fig. 4.2. *ATR-FTIR spectra of lepidocrite aged for 10h (1.0M [NaOH]$_T$ and T = 20 °C) at [Fe(III)]$_T$ = 1.0 mM (left) and [Fe(II)]$_T$: [Fe(III)]$_T$ = 1.0 mM : 1.0 mM. The initial Fe(III) is added in form of lepidocrite.*

The tiny synthetic lepidocrite particles displayed the characteristic flat, scaly crystal structure (Fig. 4.3 left) (Schwertmann and Taylor (1972)). The lepidocrite particles are quite small, approximately 1 μm in size, primarily resulting from the preparation method involving fast precipitation through aerated oxidation of $FeCl_2$ (Cornell and Schwertmann (2000)). Upon transformation, slender needle-like goethite particles were formed (Fig. 4.3 right). Similar to lepidocrite, goethite crystals are elongated and thin (Murad and Schwertmann (1983)). The goethite particles were within the same size range as lepidocrite particles, possibly slightly longer and thinner (up to 1 μm long, <100 nm wide). No evidence of hexagonal $Fe(OH)_2$ phases was observed in SEM analysis.
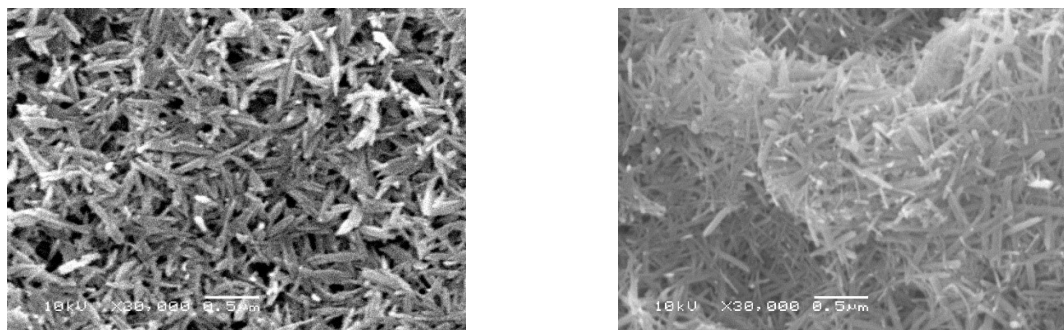
Fig. 4.3. *Lepidocrocite aged (6 hrs) at 20 °C in 1.0M [NaOH]$_T$ at [Fe(II)]$_T$: [Fe(III)]$_T$ = 1 (1.0 mM/1.0 mM). left) lepidocrocite phases at the start of the experiment. Right) goethite phases after 10h of aging in the presence of Fe(II).*

Moreover, color changes (not shown here) were useful in tracking this transformation through naked-eye observations. The initial lepidocrocite solution displayed a distinct orange color. However, as the conversion occurred and goethite started forming, the solution gradually changed to a more brown-yellow hue. Interestingly, in experiments conducted without the presence of Fe(II), the suspension maintained its orange color, indicating the persistence of lepidocrocite crystals throughout.

4.3.2. Effect of [Fe(II)]

Fig. 4.4 illustrates that the conversion of lepidocrocite occurs at a faster rate when the content of [Fe(II)]$_T$ is increased to 2.0, 5.0, or 10.0 mM, with respect to a lepidocrocite concentration of [Fe(III)]$_T$ = 1.0 mM. In experiments with [Fe(II)]$_T$: [Fe(III)]$_T$ ratios of 2.0 mM : 1.0 mM and higher, the transformation of lepidocrocite is initially accelerated (0-1.0h), but gradually slows down as lepidocrocite is consumed. These transformation patterns indicate that the diminishing amount of lepidocrocite, the sole source of Fe(III) for growing goethite crystals, eventually restricts the growth of the goethite crystals. Similar trends were also observed by Schwertmann and Taylor (1972).
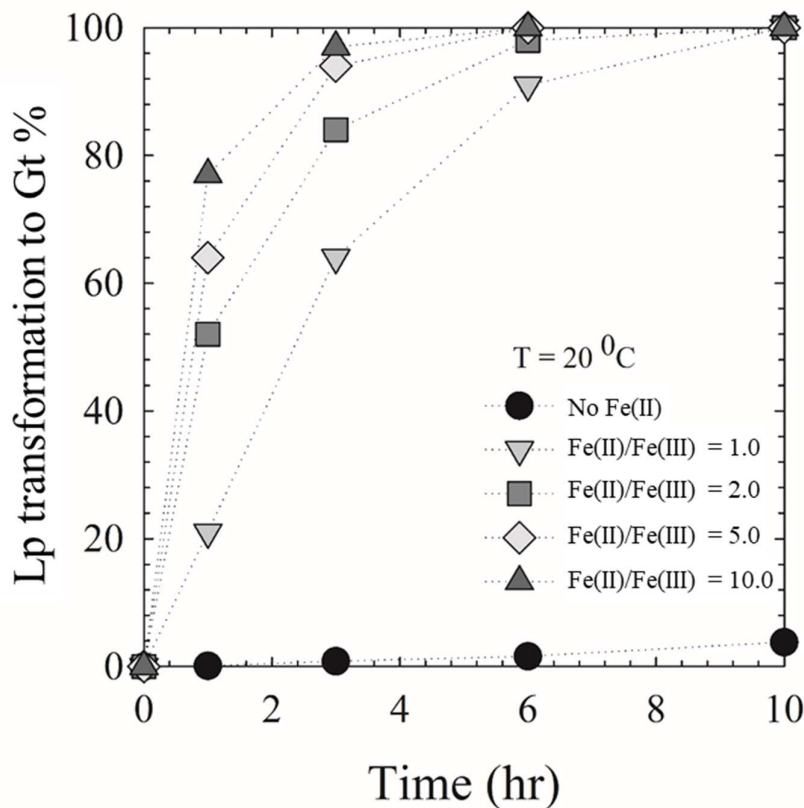
Fig. 4.4. *[Fe(II)]$_T$ dependent transformation of lepidocrocite (Lp) into goethite (Gt) as function of time. The [Fe(III)]$_T$ (added initially as lepidocrocite) was 1.0 mM in all experiments, while the [Fe(II)]$_T$ was varied from 1.0 mM, 2.0 mM, 5.0 mM and 10.0 mM (20 °C). Additional test without Fe(II) were also performed. This is denoted by experiment "no Fe(II)". The corresponding ATR-FTIR can be found in appendix 4B.*

Despite the high ratio of [Fe(II)]$_T$/[Fe(III)]$_T$ in all four tested ratios (1.0, 2.0, 5.0, and 10.0), which were sufficient for the formation of magnetite (Fe$_3$O$_4$) through co-precipitation, this phase was not observed. However, separate experiments conducted with [NaOH]$_T$ of 0.01 and 0.1 M ([Fe(II)]$_T$/[Fe(III)]$_T$ = 10.0 mM : 1.0 mM) resulted in the formation of magnetite (refer to Appendix 4C). In these cases, the orange color transformed into a black suspension, which is characteristic of magnetite. Lower ratios of [Fe(II)]$_T$: [Fe(III)]$_T$ (1.0, 2.0, and 5.0 mM : 1.0 mM, not discussed in this thesis) did not show any transformation of lepidocrocite to magnetite within a 10-hour equilibration period. At a [NaOH]$_T$ of 0.001 M, no transformation

to goethite or magnetite was observed, indicating that lepidocrocite remains stable under moderately alkaline conditions.

4.3.3. Effect of temperature

Fig. 4.5 depicts the recrystallization experiments conducted at 40, 60, and 80 °C with a $[Fe(II)]_T$: $[Fe(III)]_T$ ratio of 10.0 mM : 1.0 mM. The conversion of lepidocrocite to goethite proceeds at a slower rate at higher temperatures when Fe(II) is present. At 40 °C, within 10 hours, only 36% of the lepidocrocite transformed into goethite, while at 60 and 80 °C, the transformation rates were only a few percent per day (Fig. 4.5). The ATR-FTIR spectra can be found in the supporting information (Appendix 4B).
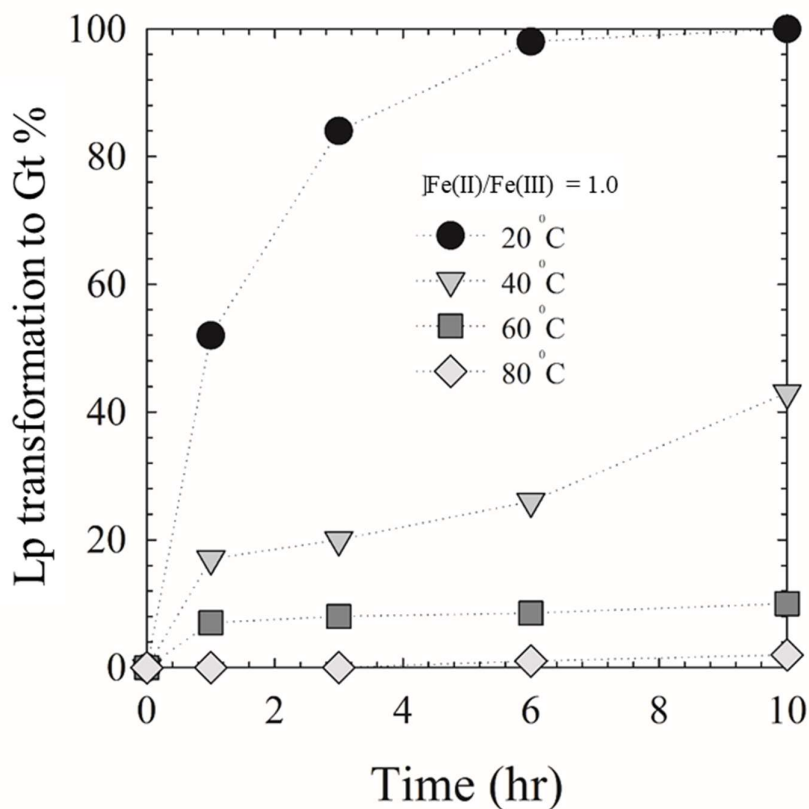

Fig. 4.5. *Effect of the temperature on the transformation of lepidocrocite phases into goethite in 1.0M* $[NaOH]_T$ *as function of time.* $[Fe(II)]_T = [Fe(III)]_T = 1.0$ *mM : 1.0 mM.*

4.4.   Discussion

4.4.1. The role of Fe(II) and temperature

It is evident from the results (Figures 4.1-4.5) obtained at 20 °C and 1.0 M $[NaOH]_T$ that the conversion of lepidocrocite to goethite occurred much faster in the presence of Fe(II), and the rate increased with $[Fe(II)]_T$ ranging from 1.0 to 10 mM (Figure 4.2). Surprisingly, the transformation rate decreased at higher temperatures (Figure 4.5). This finding is somewhat unexpected considering the kinetic factor, as Schwertmann and Taylor (1972) demonstrated that the transformation time for lepidocrocite to goethite decreased from 3200 hours (90% conversion) at 20 °C to 60 hours (80% conversion) at 80 °C (all conducted with 130 mM $[Fe(III)]_T$). In their study, at 80 °C, they observed only 12% conversion after 9 hours, which aligns well with our results showing 8% transformation of lepidocrocite to goethite after 10 hours at 80 °C (Figure 4.5). Since Schwertmann and Taylor (1972) did not introduce any Fe(II) into their system, it can be concluded that Fe(II) acts as a catalyst for the transformation of lepidocrocite at 20 and 40 °C, but not at temperatures higher than 40 °C.

4.4.2. Fe(II) as seed.

Earlier work by Schwertmann and Taylor (1972) demonstrated that the addition of goethite seeds at the beginning of experiments, in 1M NaOH at 20 °C, increased the rate of lepidocrocite to goethite transformation. For example, when goethite seeds were added at 7% of the total Fe(III) solid mass, the transformation period was shortened from approximately 5200 hours (at 90% transformation) to around 870 hours (complete transformation). Heterogeneous nucleation of goethite on the $Fe(OH)_2$ phase was observed during the air oxidation of $Fe(OH)_2$ under hyperalkaline conditions (OH:Fe > 2) (Encina et al., (2015)). This study observed the epitaxial growth of typical long goethite crystals perpendicular to the corners of the hexagonal $Fe(OH)_2$ phase. Given that the solubility product ($K_{SP} = [Fe^{2+}][OH^-]^2$) of $Fe(OH)_2$ is $10^{-15.8}$ M, 94.9% of the Fe(II) ions precipitate as $Fe(OH)_2$ at 1.0M NaOH and 20 °C. Therefore, these $Fe(OH)_2$ phases may have facilitated the heterogeneous growth of goethite crystals. Similar simulations conducted at higher temperatures show that 1 mM of Fe(II) is fully soluble above 60 °C (see Table 4.2). This finding aligns with the work of Mascolo et al. (2019) which showed that the co-precipitation of 10 mM of $[Fe(II)]_T$ and $[Fe(III)]_T$ does not occur beyond T > 40 °C. Hence, the lower transformation rate of lepidocrocite above 40 °C can be attributed to the disappearance of the seeding effect of dissolved $Fe(OH)_2$.

The transformation rate of lepidocrocite to goethite is typically highest at the initial stages and slows down as the transformation progresses, following a concave trend (Schwertmann and Taylor, (1971)), with a rate expression described by ln([Gt]/[Lp] -1) = -

0.0025*t (where t is in hours). Seeds have a significant impact on increasing the transformation rate at the initial stages, but as more goethite phases are formed during the transformation, the impact of the seeds becomes less significant. In the presence of Fe(II), we observe a similar concave transformation trend, but the rate of transformation is much faster and follows a rate expression described by ln([Gt]/[Lp] -1) = -0.5*t.

Comparing the 50-90% transformation period (Gt/Lp = 1-10) in Schwertmann and Taylor with the results obtained using Fe(OH)$_2$ seeds at [Fe(II)]$_T$/[Fe(III)]$_T$ = 1 (Figure 4.2), the 4.5-hour transformation period is still 250 times faster than the lepidocrocite to goethite transformation with 7% goethite seeds. The rate of transformation at [Fe(II)]$_T$/[Fe(III)]$_T$ = 10 is even 400 times faster (see Fig. 4.4). Such an extremely fast transformation rate cannot be solely explained by the seeding effect of Fe(OH)$_2$, suggesting that an additional process promotes the dissolution of lepidocrocite into goethite and leads to the rapid transformation rate in the presence of Fe(II).

4.4.3. Fe(II) as catalyst

The works conducted by Sheng et al. (2022) and Boland et al. (2014) have demonstrated that the interaction between Fe(II) and lepidocrocite leads to a reductive dissolution of lepidocrocite, thereby significantly accelerating the transformation rate to goethite. This electron transfer process is driven by the potential difference between the electrolyte and the lepidocrocite surface. In this scenario, the electrolyte potential is generated by the redox couple of Fe(II) (in equilibrium with Fe(OH)$_2$) and Fe(III) ions (in equilibrium with lepidocrocite).

The key difference in our study lies in the pH conditions. Unlike the aforementioned works, our experiments were conducted under alkaline conditions. In 1M NaOH solution, the active species involved in the redox couple are highly hydrolyzed Fe(OH)$_3^-$ and Fe(OH)$_4^-$ ions (Fe(OH)$_4^{2-}$ and Fe(OH)$_5^{2-}$ ions also exist, but their contributions can be disregarded due to their low concentrations in 1.0M NaOH). To determine whether an electrolytic potential was present in the Fe(II)-lepidocrocite systems under alkaline conditions, we first calculated the $E_{H,elec}$ using the Nernstian equation as follows:

$$Fe(OH)_3^- + OH^- \leftrightarrow Fe(OH)_4^- + e^-$$

$$E_{elec} = E^0(Fe(OH)_3^-/Fe(OH)_4^-) + 0.0592*\log \frac{\alpha(Fe(OH)_3^-)\alpha(OH^-)}{\alpha(Fe(OH)_4^-)} \qquad \text{eq. 4.5}$$

Using the standard E^0 ($Fe(OH)_3^-/Fe(OH)_4^-$) value of -0.24 V (Wehrli et al., (1990)), the estimated prevailing $E_{h,elec}$ was determined based on the equilibrium $\alpha(Fe(OH)_3^-)$ and $\alpha(Fe(OH)_4^-)$ using the solubility of $Fe(OH)_2$ (crystalline form) and lepidocrocite, respectively. As shown in Table 4.2, the calculated $E_{h,elec}$ value of -0.42 V is lower than the reduction potential of lepidocrocite, which is $E_{red,lep}$ = -0.05 V (Thampdrup, 2000). Therefore, this potential difference is more than sufficient to drive the electron transfer between $Fe(OH)_3^-$ and lepidocrocite. The observed rapid transformation of lepidocrocite to goethite can be attributed to the fast reductive dissolution facilitated by electron transfer between $Fe(OH)_3^-$ and lepidocrocite. Based on the initial study by Tronc et al. (1992) under alkaline conditions (between ferrihydrite and Fe(II) at pH 10), and subsequent research on the catalytic transformation of ferrihydrite and lepidocrocite in the presence of Fe(II), the following mechanism is proposed to explain the observed rapid transformation of lepidocrocite to goethite in the presence of Fe(II):

1) $Fe(OH)_3^-$ (the main constituent of the dissolved Fe(II) fraction) adsorbs onto the surface of lepidocrocite.
2) Upon adsorption, the transfer of electrons reduces the $Fe(III)_{Lp}$ compound in its structural form to $Fe(II)_{Lp}$, which then oxidizes the adsorbed $Fe(II)_{ads}$ to $Fe(III)_{ads}$.
3) The $Fe(III)_{ads}$ subsequently desorbs, undergoes hydrolysis to form $Fe(OH)_4^-$, and reprecipitates as goethite.

Although the $[Fe(OH)_4^-]$ is not measured in this study, it is generally expected that the fast electron transfer and rapid release of $Fe(III)_{ads}$ in the form of $Fe(OH)_4^-$ would temporarily increase the $[Fe(OH)_4^-]$, similar to the labile Fe(III) formation observed in the lepidocrocite-Fe(II) system at pH 7.0 and room temperature (Sheng et al. (2022)). The crystallization of $Fe(OH)_4^-$ into goethite in a 1M NaOH solution generally occurs at a much faster rate than the dissolution of lepidocrocite. The concave curves typically observed indicate a dissolution-driven transformation process. Therefore, despite the significant increase in reductive dissolution under Fe(II) conditions, it remains the rate-determining step.

The question now is what happens to the $Fe(II)_{Lp}$ that forms after the electron transfer with the lepidocrocite phase? In the study by Sheng et al. (2019), which investigated the catalytic transformation of Fe(II)-ferrihydrite and Fe(II)-lepidocrocite systems, it was discovered that a significant amount of associated Fe(II) was initially held within the ferrihydrite, but then redissolved during the transformation process. A similar process was

observed for lepidocrocite in the same study. The Fe(II) is highly soluble under neutral pH conditions (approximately 7), allowing for quick redissolution during the transformation process. On the other hand, the lower solubility of Fe(II) under alkaline conditions may largely contribute to the containment of $Fe(II)_{Lp}$ within the lepidocrocite structure. Therefore, it can be suggested that the reductive dissolution of lepidocrocite occurs through a Fe(II)-containing and highly reactive intermediate.

The continuous repetition of steps #1-#3 at the lepidocrocite-electrolyte interface likely drives the dissolution of lepidocrocite, similar to the "conveyor belt mechanism" described earlier in Yanina and Rosso (2008). However, this process seems to stop when $T \geq 40$ °C, while $E_{h,elec}$ remains at strongly reduced redox potentials (see $T = 60$ and 80 °C in Tab. 4.2), and the $\alpha(Fe(OH)_3^-)$ (which has a higher adsorption rate to lepidocrocite) and $\alpha(Fe(OH)_4^-)$ (resulting in the dissolution and recrystallization of lepidocrocite) are much higher at higher temperatures due to the increased solubility of both $Fe(OH)_2$ (thus $[Fe(OH)_3^-]$) and lepidocrocite (Schwertmann and Taylor (1972)). For example, the $\alpha(Fe(OH)_3^-)$ at 80 °C is 10^4 times higher than at 20 °C. Therefore, one could argue that the catalytic transformation of lepidocrocite is not a surface-mediated electron transfer reaction but rather proceeds through an intermediate Fe(II)-bearing reactive phase, which fails to form on the surface of lepidocrocite at 20 °C and to a lesser extent at 40 °C due to increased solubilization of the $Fe(OH)_2$.

Magnetite is a typical phase that often forms in co-precipitation studies under alkaline conditions. The work of Mascolo et al. (2019) (proven by XRD) has shown that magnetite is predominantly formed when $FeCl_2$:$FeCl_3$ (not initially precipitated as ferrihydrite or lepidocrocite) is mixed in a 1:2 ratio in 1M NaOH at 20 °C. However, in our observations, we do not see the formation of magnetite by the reaction of Fe(II) with lepidocrocite. This may be partly explained by the fact that lepidocrocite is synthesized beforehand, and the prevailing $\alpha(Fe(OH)_4^-)$ in equilibrium with lepidocrocite only creates a low supersaturation with respect to magnetite. Nonetheless, considering that magnetite is the most stable phase under alkaline conditions, based on thermodynamic solubility data, it is possible that small and undetectable (by the ATR-FTIR technique) quantities of an intermediate phase form, similar to a "reactive proto-magnetite," which is enough to drive the reductively mediated dissolution of lepidocrocite.

Due to the low solubility of $Fe(OH)_3$-, which restricts the redissolution of structural $Fe(II)_{Lp}$, it is likely that the reactive phase responsible for consuming the lepidocrocite phase proceeds through a solid-state transition pathway. One potential mechanism for this solid-state transformation is the two-step process previously proposed for the transformation of magnetite

to goethite (Train and He, 2007). According to this mechanism, when magnetite is exposed to 1-5M NaOH, it first undergoes a solid-state topotactic transformation to maghemite, followed by the dissolution of maghemite as $Fe(OH)_4^-$. This leads to the evolution of goethite through the recrystallization of the $Fe(OH)_4^-$. While the exact catalytic process is still under debate, it can be hypothesized, based on the arguments presented, that a reactive proto-magnetite-maghemite transition phase forms on the lepidocrocite and promotes its dissolution. As the lepidocrocite dissolves, the $Fe(OH)_2$ phases act as nucleation sites for goethite, with the crystal growth of goethite supported by the catalyzed dissolution of lepidocrocite into $Fe(OH)_4^-$ ions.

Table 4.2. *The speciation and fraction of total Fe(II), Fe(III) calculated for various temperatures at 1M NaOH including the calculated electrolyte potential*

NaOH	T (°C)	$[Fe(OH)_3^-]$ (mM)	$[Fe(OH)_4^-]$ (mM)	E_a ($[Fe(OH)_3^-]$/ $[Fe(OH)_4^-]$) (V)	$Fe(II)_{aq}$ (%)	$Fe(III)_{aq}$ (%)
0.001	20	1.0^E-04	2.5^E-08	-0.42	0.010	0
0.01	20	5.3^E-04	2.5^E-07	-0.42	0.053	0
0.1	20	5.2^E-03	2.5^E-06	-0.42	0.52	0
1.0	20	0.052	1.55^E-05	-0.32	5.2	0.002
	40	0.809	1.45^E-03	-0.45	80.9	0.146
	60	1.0	5.27^E-02	-0.32	100	5.27
	80	1.0	0.161	-0.19	100	27.3

For tests carried out at 0.01 and 0.1 M $[NaOH]_T$ using a similar $[Fe(II)]_T/[Fe(III)]_T$ ratio of 10.0 (see Appendix 4C), we observed that lepidocrocite distinctly transforms into magnetite (Fe_3O_4) instead of goethite. The calculated $E_{h,elec}$ of -0.42 V (for 0.01 and 0.1 M NaOH) was sufficient to drive electron transfer (Table 4.2) from adsorbed $Fe(OH)_3^-$ to lepidocrocite. However, this electron transfer resulted in a net accumulation of Fe(II) within the structure of lepidocrocite, rather than a reductive-mediated dissolution and reprecipitation of lepidocrocite into goethite. The limited occurrence of dissolution-driven recrystallization can largely be attributed to the significantly lower $\alpha(Fe(OH)_4^-)$ in 0.01 and 0.1 M NaOH compared to 1 M NaOH. This reduction not only reduces the nucleation and crystal growth of goethite, but also slows down the dissolution rate of lepidocrocite. As a result, the significant accumulation of structural Fe(II) may have driven a topotactic transformation pathway to magnetite through Fe-atom exchange and restructuring of the former phase, as proposed in earlier works by Gallagher et al. (1968), Cudennec and Lecerf (2006), Gorski et al. (2012).

In 0.001 M $[NaOH]_T$ (see Appendix 4B), both the transformation of lepidocrocite into goethite and magnetite were not observed, at least not within the 10-hour experimental time frame. This aligns with the findings of Tamaura et al. (1982), which stated that longer time scales (e.g., > 2500 h) are required to observe these transformations at the solubility limit of $Fe(OH)_2$ (pH ~10). The low transformation rate indicates that the electron transfer occurs at a very slow rate, likely due to the ~250x lower activities of $\alpha(Fe(OH)_3^-)$ (Table 4.2). The ~10^3x lower $\alpha(Fe(OH)_4^-)$ also leads to lower nucleation and crystal growth rates of goethite and magnetite.

4.5. Implication of the enhanced lepidocrocite transformation for application of iron electro-coagulation systems

In most Fe-EC cells, it is standard design practice to keep a short distance between the anode and the cathode (sometimes < 1 cm apart) in order to reduce overvoltage for the electrochemical reactions at the electrode surfaces (current resistance drop or IR-drop, Chen (2004)). Several electrodes are stacked in the EC cell (e.g., #cells: 10-100) to create a high electrode surface to volume ratio. Fe-EC cells are mostly operated at high current densities to dose much Fe(II) and Fe(III) per minimum amount of electrode surface area. All of these designs are implemented to lower electricity costs, reduce sludge formation (and disposal), and minimize electrode consumption. However, this may have a detrimental effect on the production of lepidocrocite due to the following reasons: At high current densities, the generation of cathodic OH^- ions is faster than the diffusion rate of OH- away from the electrode surface, resulting in localized high pH regions (Honda et al. (1998)). The O_2 supply in these high current cells is insufficient to keep up with the Fe(II) generation rate. As a consequence, not only does the pH of the electrolyte increase, but also the $[Fe(II)]_T$ rises. Due to the more negative cathode potentials (E_{cat} < -0.3 V) compared to the $E^0(Fe(II)/Fe(III))$ redox couple, direct lepidocrocite reduction can co-generate Fe(II). Overall, in compact Fe-EC cell stacks with large amounts of electrode surface area placed in close proximity to each other, the transformation of lepidocrocite to goethite ($\geq$ 1M $[NaOH]_T$) or magnetite (0.01-0.1 M $[NaOH]_T$) can be accelerated by two simultaneous events near the cathode. For most heavy metal removal, the transformation to goethite will decrease the adsorption capacity compared to a lepidocrocite-dominated phase, which in practice means that more Fe(0) will need to be consumed to compensate for the loss in adsorption capacity. This, in turn, leads to higher operational costs. On the other hand, certain contaminants such as As(V) may be effectively removed (below a discharge concentration limit

of < 1 μg/L) with magnetite rather than lepidocrocite (Van Genuchten, (2020)), so enhanced transformation could also have a positive outcome on the removal of contaminants such as As(V) or Se(VI) that are sensitive to reduction. It is therefore crucial to design Fe-EC cells by taking these effects into consideration. However, while explicit measurements of pH near the cathode during EC operations have not been conducted, this study is the first to demonstrate that lepidocrocite can transform extremely rapidly under the alkaline conditions of the cathode surface and the presence of Fe(II). This suggests that the electrochemical operating conditions with Fe-EC can significantly alter the removal of metal contaminants. Thus, further research in this field is necessary to investigate the impact of Fe-EC operation and cell designs, and to find ways to prevent the enhanced transformation of lepidocrocite and even ferrihydrite.

4.6. Conclusions

In highly alkaline conditions, specifically at 1.0 M $[NaOH]_T$ and a temperature of $T = 20$ °C, the mineral lepidocrocite undergoes rapid recrystallization (within 1-10 hours) into goethite. This transformation occurs to a significant extent, with 80-90% of lepidocrocite being converted to goethite. The presence of Fe(II), in the form of ferrous chloride at concentrations of 1.0 to 10.0 mM $[Fe(II)]_T$, facilitates this transformation. However, in the absence of Fe(II), the rate of transformation is much slower at 20 °C, with less than 5% of lepidocrocite being converted to goethite within a 10-hour period.

Interestingly, the uptake of Fe(II) by lepidocrocite and subsequent formation of magnetite (Fe_3O_4) was not observed in 1.0 M $[NaOH]_T$. This observation was consistent across tests conducted in 0.01 and 0.1 M $[NaOH]_T$ as well. However, in these lower $[NaOH]_T$ conditions, there was a noticeable net uptake of Fe(II) by lepidocrocite, leading to the transformation of lepidocrocite into magnetite. At the lowest $[NaOH]_T$ of 0.001 M, neither the transformation of lepidocrocite to goethite nor the formation of magnetite was observed within a 10-hour period. This can be attributed to the low dissolution rate of lepidocrocite and the inefficient electron transfer between $Fe(OH)_3^-$ and lepidocrocite.

In 1.0 M NaOH, the majority of Fe(II) precipitates as the $Fe(OH)_2$ phase. The role of Fe(II) in the crystallization rate of lepidocrocite can be partly explained by seeding, where the surface of $Fe(OH)_2$ facilitates the energetically favorable heterogeneous nucleation and crystal growth of $Fe(OH)_4^-$ in lepidocrocite. However, this explanation does not fully account for the observed high dissolution-driven transformation of lepidocrocite.

Additional arguments suggest that continuous electron transfer between dissolved $Fe(OH)_3^-$ and the surface of lepidocrocite enhances the dissolution rate of lepidocrocite through reductive dissolution. The limited solubility of Fe(II) in 1.0 M NaOH inhibits the redissolution of structural Fe(II) formed during electron transfer. As a result, it is proposed that this reductive dissolution occurs through the continuous formation and dissolution of an intermediate solid phase containing Fe(II), following a "conveyor belt" principle. The transformation rate of lepidocrocite slows down at temperatures between 20 °C and 40 °C and completely ceases at temperatures above 40 °C. These effects can be attributed to the full dissolution of $Fe(OH)_2$ and the increased solubility of the suggested intermediate Fe(II)-bearing solid phase.

References

Antony H., Legrand L.; Marechal L.; Perrin S., Dillmann P, Chausse A., *Electrochim. Acta*, **2005**, 51, 745–753.

Bechine K.; Subrt J.; Hanslik T., Zapetal V., Tlaskal J., Lipka J., Seplak B., Rotter M., Z. Anorg. Allg. Chem. **1982**, 489, 186-196.

Chen G., *Sep. and Purif. Tech.*, **2004**, 38, 11–41

Cornell, R. M.; Schwertmann, U. *The Iron Oxides: Structure, Properties, Reactions, Occurrences, and Uses*, 2nd ed.; Wiley- VCH: Weinheim, **2003**.

Cornell R.M., Schneider W., Giovanoli R., *Clay Minerals* **1989,** 24, (3), 549-553.

Das S., Hendry M.J., Essilfie-Dughan J., *Applied Geochemistry*, **2013**, 28, 185-193

Deslouis C., Frateur I.; Maurin G., Tribollet B., *J. App. Electrochemistry*, **1997**, 27, 482-492.

Deligianni H., Romankiw L.T., *IBM. J. Res. Developt*, **1993**, 37 (2), 85-95

Encina E.R., Distaso M., Klupp Taylor R.N., Peukert W., *Cryst. Growth Des.* **2015**, 15, 1, 194–203

Gorski C.A. Handler R.M., Beard B.L., Pasakarnis T., Johnson C.M., Scherer M.M. *Environ. Sci. Technol*. **2012**, 46, 22, 12399–12407

He T., Traina S.J.. *Clay Minerals,* **2007** 42(1):13-19

Honda T., Murase K., Hirato T., Awakura Y., *J. App. Electrochemistry*, **1998**, 28, 617-622.

Ishikawa T., Takeuchi K. , K. Kandori; Nagayama T., **2005**, 266, *Coll. And Surf. A: Physicochem. Eng. Aspects,* 155-159.

Jolivet J.P.; Tronc E.; Chaneac C., *Comptes Rendus Geoscience* **2006,** 338, (6-7), 488-497.

Mascolo M.C., Pei Y., Ring T.A, *Materials* **2013**, 6, 5549-5567.

Mollah M.Y.A.; Schennah R.; Parga J.R.; Cocke D.L., *Journal of Hazardous Materials B87* **2001,** B84, 29-41.

Mollah M.Y.A.; P. Morkovsky; M. Kesmez; D.L. Cocke, *Journal of Hazardous Materials B114* **2004,** 199-210.

Moreno H.A., Cocke D.L, Gomes J.A.G., Morkovsky P., Parga J.R., Peterson J. and Garcia C.. *ECS Transactions*, **2007,** 6 (9) 1-15.

Oh S.J.; Kwon S.J.; Lee J.Y.; Yoo J.Y.; Choo W.Y., *Corrosion* **2002**, 58, (6), 498-504.

Music M.; Gotic M.; Popovic S., *Journal of Materials Science* **1993,** 28, (9), 5744-5752.

Pedersen H.D.; Postma D.; Jakobsen R.; Larsen O., *Geoch. Et Cosmoch. Acta* **2005,** 69, (16), 3967-3977.

Persson P., Lovgren L., Geoch. Et Cosmochim., 1996, 60, (15), 2789-2799.

Ruan H.D., Frost R.L., Kloprogge J.T., Duong L., Spectrochim. Acta Part a-, Mol. and Biomol. Spec., **2002,** 58, (5), 967-981.

Schwertmann U.; Taylor R.M., *Clay Minerals*, **1979**, 14, 285-293.

Schwertmann U.; Taylor R.M., *Clays and clay minerals*, **1972**, 20, 151-158.

Schwertmann U.; Murad E., *Clays and Clay Minerals*, **1983**, 31, (4), 277-284.

Stratmann M.; Streckel H., Corr. Sci. **1990**, 30, (6/7), 697-714.

Tamaura Y., Buduan P.V., Katsura T., J. *the Chemical Society-Dalton Transactions* **1981**, (9), 1807-1811.

Thamdrup, B., *Adv. Microb. Ecol.*, 2000, 16, 41-84.

Van Oosterhout J., *J. Inorg. Nucl. Chem.*, **1967**, 29, 1235-1238.

Van Genuchten C.M., Behrends T., Stipp S.L.S., Dideriksen K. *Water Reseach*, **2020,** 168, 115170

Weckler B., Lutz H.D., European J. Solid State and Inorg. Chem., **1998**, 35, (8-9), 531-544.

Wehrli, B., Redox reactions of metal ions at mineral surfaces. In: Stumm, W. (Ed.), Aquatic chemical kinetics: reaction rates of processes in natural waters. **1990**, Wiley, New York.

Yanina S.V., Rosso K.M., *Science*, **2008**, 320, 5873, 218-222

Zhang T.C.; Huang Y.H., *Water Research* **2006,** 25, (1), 3075-3082.

Appendix 4A: The ATR-FTIR data of the lepidocrocite transformation period in 1.0 M [NaOH]$_T$, [Fe(II)]$_T$ of 0, 1.0, 2.0, 5.0 and 10.0 mM, and lepidocrocite concentration, i.e. [Fe(III)]$_T$, of 1.0 mM. The experiments were run for 10h.
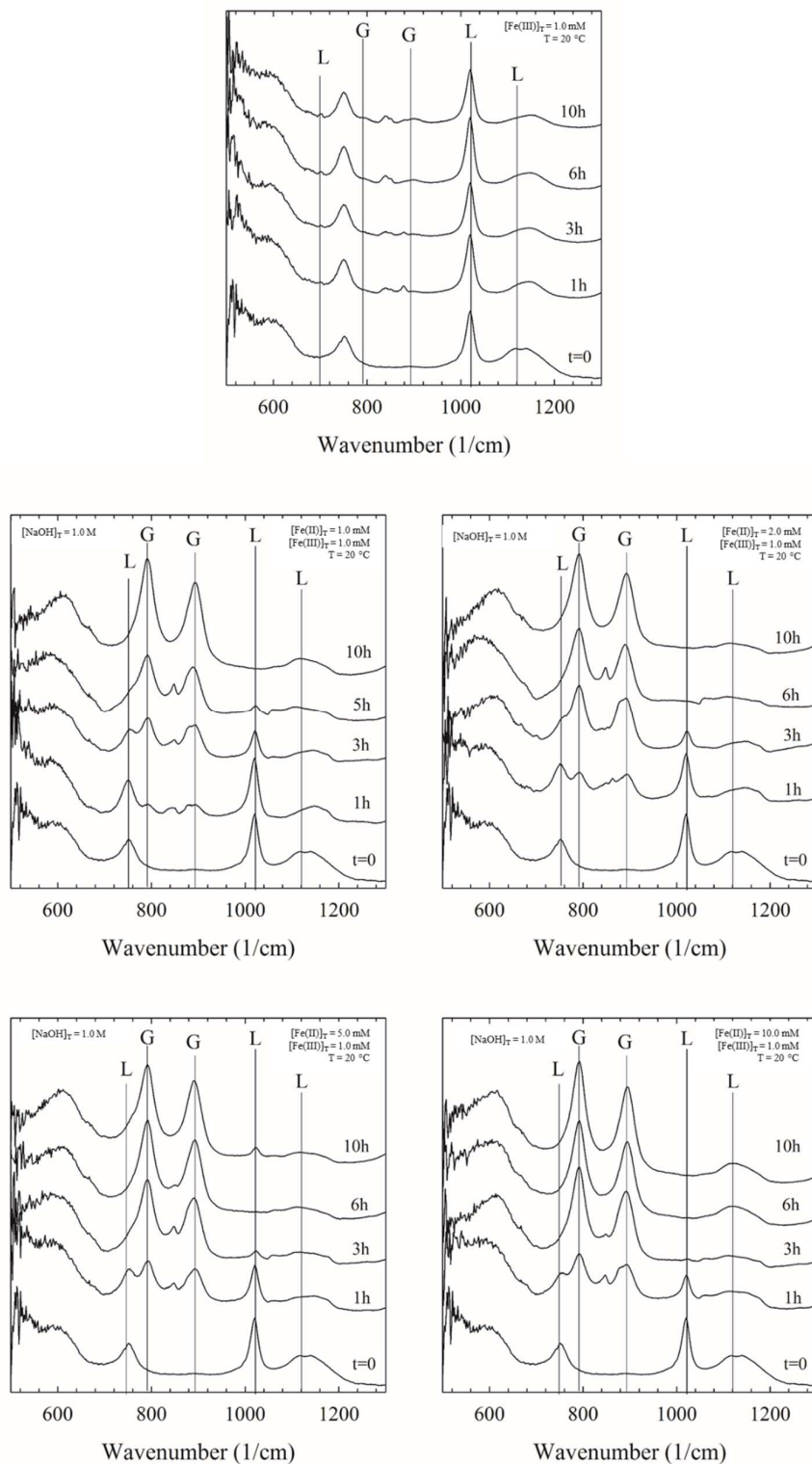
Appendix 4B. ATR-FTIR spectra of lepidocrocite transformation in 1.0M NaOH and $[Fe(II)]_T$: $[Fe(III)]_T$ = 1.0 mM : 1.0 mM at temperatures of i) 20 ^{0}C ii) 40 ^{0}C iii) 60 ^{0}C iv) 80 ^{0}C. The ATR-FTIR data at 20 ^{0}C are also shown in Fig. 4.1.
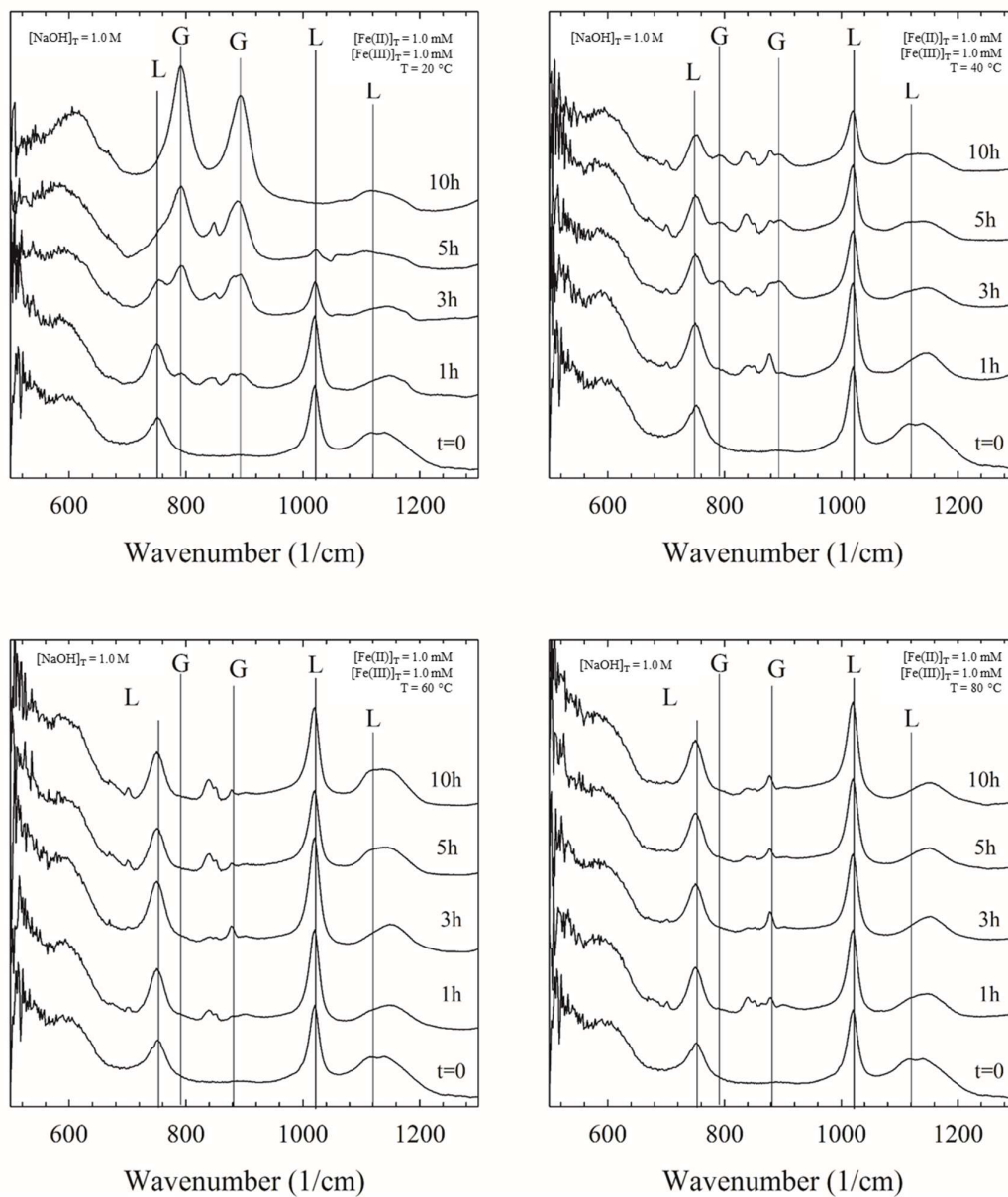
Appendix 4C. ATR-FTIR spectra of the lepidocrocite transformation at different [NaOH]$_T$ of 0.001, 0.01, 0.1 and 1.0M and using a [Fe(II)]$_T$: [Fe(III)]$_T$ = 1.0 mM : 1.0 mM. The test were carried out for a period of 10h.

5
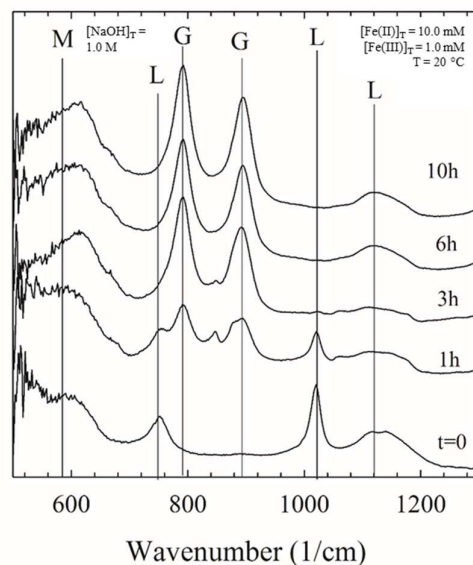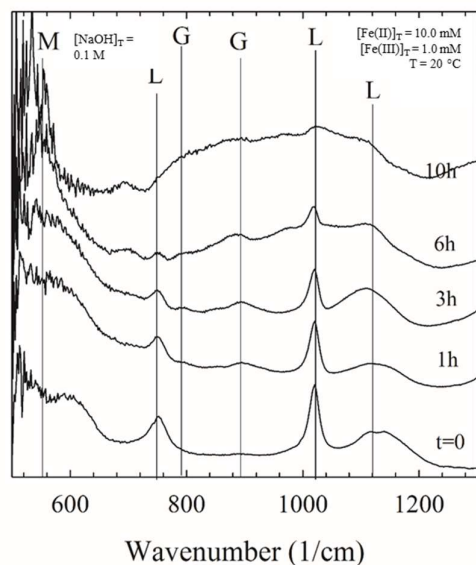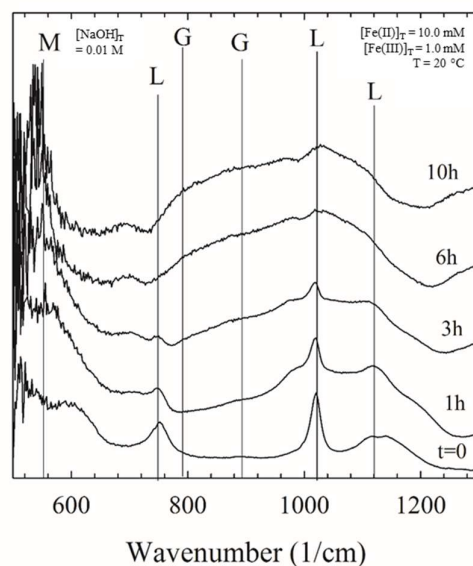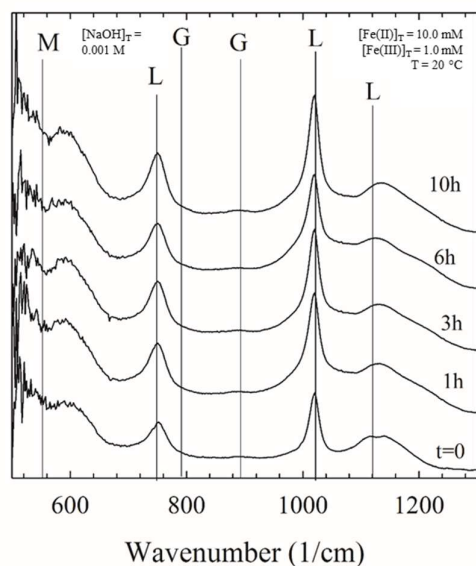
Electrochemical PO$_4$ recovery from nanofiltration concentrates

Abstract. The high total phosphorus content of raw domestic wastewater with its significant eutrophication potential offers an excellent possibility for PO_4 recovery. Continuous recirculation of NF concentrate to an MBR and simultaneous PO_4 recovery from the NF concentrate can be applied to produce reusable water, recovering PO_4, while at the same time decreasing the scaling potential of the recirculated NF concentrate, prolonging the retention times of slowly biodegradable soluble compounds (e.g. micropollutants) and recirculating multivalent cations to promote the bio-flocculation. Here we introduce an electrochemical system to recover PO_4. An electrochemical cell was divided into an anode and a cathode compartment separated by a cation exchange membrane. Precipitation of PO_4 from nanofiltration concentrate was induced by locally increasing the pH at the cathode surface by water electrolysis and thereby creating supersaturated conditions at the cathode. 80 to 95% recovery of total PO_4 was achieved at a pH of 8 to 10 near the cathode. Ion analysis, XRD and ATR-FTIR spectra indicated that the precipitate consisted of amorphous calcium phosphate (ACP) and minor proportions of amorphous calcium carbonate (ACC). The amount of ACC was dependent on the pH. Calcium phosphate scaling at the cathode surface did not occur due to H_2-gas formation preventing nucleation and growth at the cathode.

5.1. Introduction

Recovery of phosphate (PO_4) and production of reusable water present new challenges in domestic wastewater treatment and are important elements in balancing human utilization of planetary resources (Rockstrom, 2009). Due to the large volumes of domestic wastewater produced, the PO_4 load in this water is high, even though the concentrations are relatively low (4-16 mg PO_4^{3-} P/L) (Tchobanoglous 2004). PO_4 has a large eutrophication potential, therefore it needs to be removed before the water can be discharged. Generally this is accomplished by chemical precipitation with metal salts, or by enhanced biological phosphorus removal. In both cases the PO_4 ends up in the excess sludge line and finally will be wasted. Due to the high value of PO_4 as a resource, a much better option would be to recover and reuse PO_4 from domestic wastewater (Roeleveld et al. 2004). PO_4 recovery from the water line is possible, for example by crystallization (Sartorius et al. 2011), but because of the low concentrations this is not very effective. Nowadays, membrane concentrates evolving from wastewater treatment are a potential source for PO_4 recovery as well. A membrane bioreactor (MBR) followed by a nanofiltration membrane (NF) can be applied to produce reusable water. The NF permeate can be used for e.g. households, industrial processes or as irrigation water (Jacob et al. 2010, Noronha et al. (2002). NF concentrate disposal to surface waters or landfills however, has serious environmental impacts and remains the bottleneck of this application (Nederlof et al. 2005). To address this issue, continuous recirculation of NF concentrate to an MBR and simultaneous PO_4 recovery from the NF concentrate can be applied in an integrated process to recover the phosphorus, while at the same time decreasing the scaling potential of the recirculated NF concentrate on the NF membranes (Sperlich et al. 2010), prolonging the retention times of slowly biodegradable soluble compounds (e.g. micropollutants) (Joss et al. (2011), and recirculating multivalent cations to promote the bio-flocculation, which may reduce fouling of the MBR membranes (Van den Broeck et al. 2012). Caustic soda can be added to create supersaturated conditions at high pH to induce crystallization of P as calcium phosphate (Doyle and Parsons (2002). PO_4 precipitation, for instance as amorphous calcium phosphate (ACP), monetite, brushite or hydroxyapatite (HAP), is dependent on the conditions available for supersaturation, i.e. chemical equilibria and thermodynamic solubility products (Table 5.1) (Dorozhkin (2007), Fernandez et al. (1999)) but is also strongly kinetically determined.

Table 5.1 *Overview of most common calcium phosphate with respective molar Ca to PO$_4$ ratios (Dorozhkin (2007), Fernandez et al. (1999)).*

Compound	Reaction	Ca/P ratio
Brushite	$HPO_4^{2-} + Ca^{2+} + 2H_2O \rightarrow CaHPO_4.2H_2O$	1.0
Monetite	$HPO_4^{2-} + Ca^{2+} \rightarrow CaHPO_4$	1.0
Octacalcium phosphate (OCP)	$6HPO_4^{2-} + 8Ca^{2+} + 5H_2O \rightarrow Ca_8H_2(PO_4)_6.5H_2O + 4H^+$	1.3
Amorphous calcium phosphate (ACP)	$2HPO_4^{2-} + 3Ca^{2+} + 3H_2O \rightarrow Ca_3(PO_4)_2.3H_2O + 2H^+$	1.5
Hydroxyapatite	$3HPO_4^{2-} + 3Ca^{2+} + 4OH^- \rightarrow Ca_5(PO_4)_3OH^-$	1.7

Caustic soda addition to create alkaline conditions, as used in technologies like the Crystallactor® process or the Kurita fixed bed crystallization column (Joko (1984)), can be avoided by using water electrolysis. Electrochemical precipitation has been used for water softening (Gabrielli et al. (2006)) to remove carbonate hardness from cooling water systems in order to prevent scaling. Commonly, both electrodes are simultaneously present in the treated solution. More recently, a system to remove PO$_4$ from MBR feed using the aluminium of the electrodes to precipitate solid aluminium PO$_4$ through coagulation has been described (Kim et al. (2010)). However, in that case, the desired reactions with electrode material resulted in undesired replacement costs. Another electrochemical system, where both electrodes were in the same solution to precipitate struvite from artificial electrolytes at neutral pH was described (Wang et al. (2010)). However, the deposition of precipitates at the electrode surface decreased the efficiency. Finally, an electrochemical application for calcium carbonate hardness reduction in cooling waters including an ion exchange membrane to separate the cathode and anode compartment was introduced (Hasson et al. (2010)). This process could also be used for PO$_4$ recovery. Starting from these electrochemical processes, we propose an integrated concept that combines domestic wastewater treatment in an MBR NF system (including continuous NF concentrate recirculation to the MBR) with an electrochemical process to recover PO$_4$. Compared to other techniques to recover PO$_4$, it has the advantage that salts and base are not required and no transportation of chemicals and replacement costs for electrode material are needed. In this research we provide a proof of principle of a batch EPR concept for electrochemical PO$_4$ recovery using real MBR NF nanofiltration concentrate as feed for the EPR. In this first study, the performance of the cathode process is evaluated and compared with the recovery obtainable with e.g. those of the commercially available Crystallactor® process. Based on an average of 5 mg PO$_4^{3-}$ P/L in the wastewater inflow, a NF rejection for PO$_4$ of 85% and an NF water recovery of 80%, the P concentration in the NF concentrate is 22 mg/L. With an assumed PO$_4$ recovery by the EPR of 80%, a PO$_4$ recovery of 70% of the wastewater

inflow is calculated. This would be comparable to the P-recovery obtainable with the commercial Crystallactor®, which is between 65-70% (Woods et al. (1999)). To the best of our knowledge this is the first time such a study on an enhanced PO_4 recovery (EPR) system including a cation exchange membrane has been conducted on MBR/NF concentrates from real domestic wastewater coming from a NF concentrate recirculation loop.

5.2. Principle EPR

Fig. 5.1 shows the principle of the batch EPR process for the recovery of PO_4 from NF concentrate. This batch process is used here to prove that PO_4 recovery from NF concentrates is indeed possible. In this case both anode and cathode compartment are fed separately with the same NF concentrate. In a continuous process however, the NF concentrate could first pass the anode (low pH) to strip the carbonates and then pass the cathode compartment to recover PO_4 (high pH).
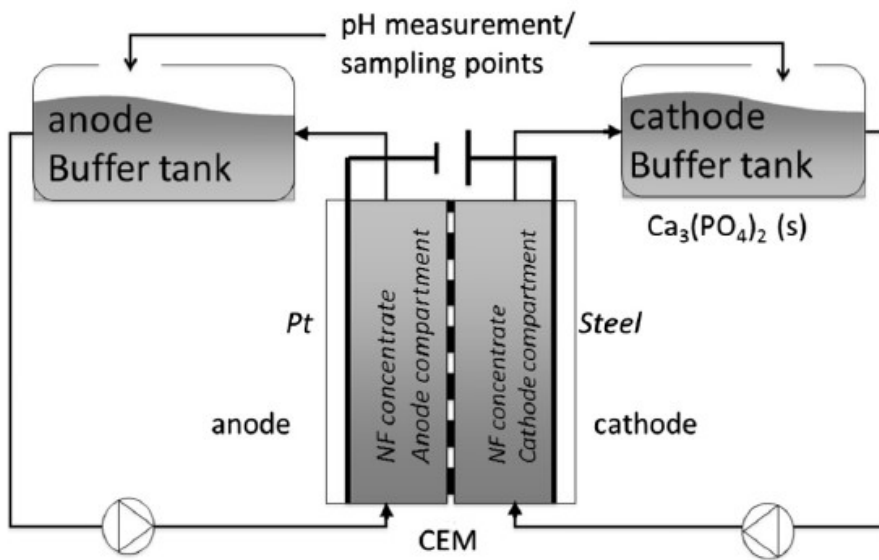
Fig. 5.1. *Schematic view of the non-continuous electrochemical setup for the recovery of PO_4s; including electrochemical cell, electrodes, CEM, buffer tanks, pumps and power supply.*

The anode and cathode are separated by a cation exchange membrane (CEM). This membrane separates the electrolytes with low (anode) and high (cathode) pH, and allows the control of the pH in both chambers without neutralization of the solutions, thus dramatically increasing the process efficiency due to the much higher pH obtainable in the cathode and required for efficient PO_4 recovery. At the anode and the cathode, the following reactions occur:

Anode: $2H_2O \rightarrow 4H^+ + O_2 + 4e^-$ $E^0 = +1.23$ V   eq. 5.1

Cathode: $4H_2O + 4e^- \rightarrow 4OH^- + 2H_2$ $E^0 = 0$ V   eq. 5.2
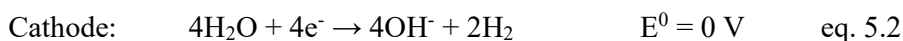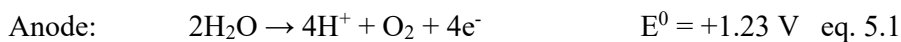
At a pH range of the NF concentrate of 7-7.8, potential crystallization of calcium phosphate is limited; especially in wastewaters that contain humic acids, formation of such crystals can be inhibited (Alvarez et al. (2004)). The production of OH^- -ions in the cathode chamber increases the pH in that compartment, causing the main $H_2PO_4^-$ -ions to convert mainly to HPO_4^{2-} and/or to PO_4^{3-}. The high pH in the cathode compartment causes immediate precipitation of the PO_4 in the liquid and consequently it is hypothesized that precipitation at the electrode surface hardly takes place. After crystallization, a final separation by centrifugation, settling or filtration enhanced by seed crystals or sand allows the final recovery of PO_4 compounds (Eggers et al. (1991)).

5.3.   Material and methods

5.3.1.   Material and experimental setup

Nanofiltration concentrate was produced by filtration of permeate from an aerobic pilot-scale MBR that was fed with domestic wastewater withdrawn from the local sewer system. The MBR employed flat sheet Kubota membranes (nominal pore size: 400 nm) running at a flux of 15 $L/m^2/hr$. The MBR permeate was filtered by cylindrical 400 mL Amicon type dead-end filtration cells containing flat sheet nanofiltration membranes (NF 245 Dow™ Filmtec™) with a total membrane area of 0.0044 m^2 (operating pressure: 5 bar). The remaining concentrate in the cell was used for the experiments. In this manner the MBR effluent was filtered up to a concentration factor of 3-4, a practical limit in the stirred Amicon cells related to fouling of the NF membrane by the MBR permeate. The NF concentrate had a pH of 7.8, no precipitation was observed.

5.3.2.   Electrochemically induced precipitation

The EPR cell consisted of two acrylic glass chambers, a platinum anode in one chamber, a steel cathode plate in the other chamber (electrode area: 0.0022 m^2 each) and a total liquid volume in the cell plus the buffer tanks of 400 mL. 200 mL nanofiltration concentrate was filled in each chamber (incl. compartment and subsequent buffer tank) and circulated through the anode and cathode compartment respectively (Fig. 5.1). Electrical current was applied by a power supply

(ES 015-10, DELTA ELECTRONIKA, The Netherlands). 10 and 50 mA were chosen for the experiments with an applied voltage of 3 V. Mainly the duration of the applied current determined the pH. Both electrodes in the electrochemical cell were separated by the use of a 0.0022 m^2 Fumasep® FKS cation exchange membrane (CEM) (FuMA-Tech GmbH, St. Ingbert, Germany) to prevent the migration of anions (e.g. PO_4^{3-}) from anode to cathode. More importantly, due to the CEM the OH^- produced at the cathode does not migrate to the anode. Although the protons produced at the anode can freely migrate from the anode to the cathode compartment, neutralization of the pH was not expected because even at pH = 8 (the lowest pH used in these measurements) the proton concentration (10^{-8} M) (Table 5.2) was very low compared to the concentration of other cations, like Ca^{2+}, Na^+, K^+, and Mg^{2+} (10^{-3}-10^{-4} M) (Table 5.2). Both buffer tanks were open to the atmosphere for gas release, for pH measurements (SenTix 41, WTW, Germany) and for sampling. The cathode buffer tank was used as a settling tank for calcium phosphate precipitates. As these experiments were non-continuous batch tests to evaluate the potential of the concept for PO_4 recovery, only the NF concentrate in the cathode chamber was addressed. Nevertheless, in a continuous process the full stream could be treated, as in that case, it would first pass the anode followed by the cathode. In the batch system the NF concentrate was introduced not only into the cathode but also the anode compartment. This was done to balance the ion concentrations and the conductivity in both electrode compartments to avoid diffusional transport due to large differences in ion concentrations. The NF concentrate in the two separated electrochemical cell chambers was circulated by a peristaltic pump (Masterflex®) at a recirculation rate of 5 mL min^{-1}, until the target pH was measurable in the cathode buffer tank and precipitation was induced. The batch time for the total volume of 0.200 L (volume per tank divided by the recirculation rate) was 40 minutes. As approximately 0.050 L were in the circulation loop (tubes + electrochemical cell), a pH increase and therefore very high removal rates were already detectable in the buffer tank after 15 minutes. Experiments with a target pH of 8.25, 8.5 and 9 were carried out at a current of 10 mA (3V) (current density of 4.6 A/m^2 or 3.03×10^{-4} A/cm^2 per electrode compartment). The test at pH 9 (10 mA) was repeated as triplicate. A higher current of 50 mA (3V) (current density of 22.7 $A.m^{-2}$ or $1.5.10^{-3}$ A cm^{-3} per electrode compartment) was needed to achieve pH 10 or 11. All experiments were run for a minimum of 2 hours at each target pH level, which was reached after 15-30 minutes depending on the current applied. The current was kept constant until the desired pH was reached. PO_4 recovery efficiency was derived from the observed PO4 depletion in the cathode liquid.

5.3.3. Ion and TIC analysis

For analysis, the NF concentrate from the cathode compartment before and after the EPR experiment was filtered with a 0.45 Dm membrane filter to separate the solids from the solution. Concentrations of anions and cations in the remaining liquid were measured. Anions were measured with ion chromatography (Compact IC 761, Metrohm). Cations were analyzed with inductively coupled plasma (Optima 5300 DV, Perkin Elmer). Total inorganic carbon (TIC) content of the NF concentrate before and after the experiments was determined by TOC-VCSH (Shimadzu). For this all inorganic carbon species were transferred to CO_2 and analyzed. Analytical software (Visual MINTEQ 3.0) was used to indicate potential saturation and ion activities in the NF concentrate at different pH. This calculation includes inorganics but does not account for organics as for instance humic acids. Recovery of PO_4 and removal of all other compounds describes the depletion from the feed solution (Inflow – remaining solution after treatment).

5.3.4. XRD and ATR-FTIR analysis

After each experiment ATR-FTIR was performed to analyze the functional groups on the surface of the precipitate with a Shimadzu 4800-s ATR-FTIR spectrometer. Precipitates were obtained by filtration through a 200 nm filter (IsoporeTM, Merck Millipore). The ATR-FTIR spectra were determined at a spectrum resolution of 2.0 cm^{-1} and 100 scans. Precipitate samples were analyzed with X-ray powder diffraction (XRPD) to clarify the crystal structure. Samples were collected at four different pH levels (pH 8.25, 8.5, 9 and 10). The X-Ray powder diffraction spectra show the 2 of the crystalline phases. The patterns were recorded in a Bragg-Brentano geometry by a Bruker D8 advanced diffractometer equipped with a Vantec position sensitive detector. The data collection was carried out at room temperature using monochromatic Co K radiation (= 0.179026 nm) in the 2 region between 20° and 120°. The step time was 1 second. The sample was placed on a Si {510} times new substrate and rotated during measurement. Data evaluation was performed using the Bruker program EVA.

5.3.5. SEM analysis

SEM-EDX analysis and pictures of the precipitates was made using a Scanning Electron Microscope JEOL-6480LV (JEOL Ltd., Tokyo, Japan) to analyze size and shape of the precipitation. All samples were coated with a thin (10 nm) gold layer (JEOL JFC-1200 fine coater) before observation under high vacuum at 10 kV.

5.4. Results and discussion

5.4.1. Nanofiltration concentrates

Average concentrations of relevant dissolved constituents in the produced nanofiltration concentrates are shown in Table 5.2. With about 5 mg.L^{-1} of PO_4^{3-}-P in the feed for the NF (i.e. MBR permeate), the PO_4 content in the NF concentrate (to be fed to the EPR) was as expected around 23 mg L^{-1}. These NF concentrate solutions were used as feed for the EPR. The average molar ratio of Ca/P of 2.6 shows a desired excess calcium concentration available for precipitation, compared to the needed Ca/P ratios in common precipitates (Table 5.1). An exception was the experiment at pH 10, where the Ca/P ratio was 1.8. Nevertheless, this is still sufficiently high to obtain all of the mentioned phosphorous precipitates (Table 5.1). These variations in concentration of the NF concentrate occurred because the concentrates were individually prepared in batch tests (in Amicon filtration cells) from real domestic wastewater.

Table 5.2 *Average constituent concentrations in the NF concentrates used in the EPR process and average NF rejections (%) of each of the compounds during NF concentrate production.*

Component	Average constituents in NF concentrates	Average rejections by NF (%)	Unit	NF-concentrate used in this work
pH	7.8 ± 0.1	-	-	7.85
[Na$^+$]	130 ± 46	25	mg/L	120
[K$^+$]	22 ± 14	7	mg/L	24
[Inorg. Carbon]	55 ± 8	83	mg/L	52
[Mg^{2+}]	22 ± 4	34	mg/L	20
[Ca^{2+}]	83 ± 10	29	mg/L	81
[PO$_4^{3-}$ -P]	23 ± 10	85	mg/L	25

5.4.2. PO$_4$ recovery from NF concentrate

Fig. 5.2 shows the PO$_4$ recovery at pH 8.25, 8.5, 9.0, 10.0 and 11.0. The operation with a cathode pH of 8.25 yielded approximately 70% PO$_4$ recovery, pH 8.5 yielded 74% recovery, pH 9.0 about 90% and pH 10.0 and 11.0 both gave recoveries of 96%. This increase in recovery efficiency with pH is caused by increasing supersaturation for PO$_4$ precipitates at higher pH (Kim et al. (2004)). Fig. 5.2 shows that operation at low current (10 mA) was already sufficient to recover considerable amounts of PO$_4$ at a pH of 9 or higher.
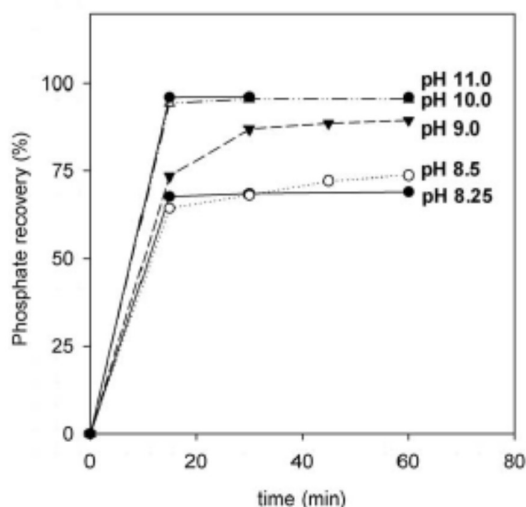
Fig. 5.2. *PO$_4$ recoveries from the NF concentrate measured over time at different target pH values. Standard deviation for experiments performed at pH 9 was 1.6%, which is considered to be a representative value for all experiments.*

On average, 0.4 - 0.6 mM (38 - 57 mg/L) of PO$_4$ was recovered from the solution, except at pH 10 where 1.23 mM (117 mg/L) was recovered due to the mentioned higher initial PO$_4$ concentration. Overall, the current efficiency for the recovery of PO$_4$ decreased with increasing pH (pH 9, 10 mA: 53%; pH 11, 50 mA: 19%). Neutralization of the electrolytes due to H$^+$-migration was not found.

5.4.3. Precipitate composition

Fig. 5.3 shows the molar Ca/PO$_4$ ratio of the precipitate that was recovered from the cathode compartment. This ratio increased with increasing pH from 0.95 at pH 8.25 up to 2.63 at a pH of 11. This increase with pH can be explained by an increasing (as calcium) carbonate ion removal (0, 1.5, 2.2, 17.9 and 25 mg/L, respectively) from the solution at increased pH values (Fig. 5.4).
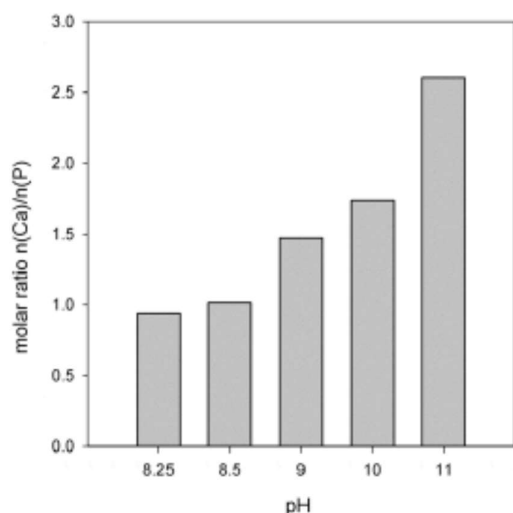
Fig. 5.3. *Molar ratios of Ca(II) to PO₄ of the precipitate recovered from the EPR and calculated from concentration changes in the cathode liquid after experiments with different pH. Standard deviation of the experiments performed at pH 9 was ±0.5, and this value is considered to be representative for the other experiments as well.*

Fig. 5.4 shows that carbonate removal indeed increased with pH from zero at pH 8.25 up to a maximum carbonate removal of 44.6% observed at pH 11 (Fig. 5.4). This also shows that the calcium removal from the solution does not exceed 30% up to pH 9, which is desired to be able to still improve the bio-flocculation by the recirculation of this NF concentrate to the MBR. The formation of calcium carbonate is supported by the ATR-FTIR results shown in Fig. 5.6.
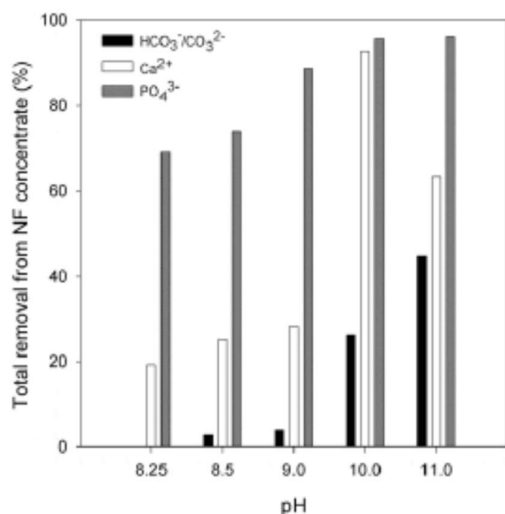

Fig. 5.4. *PO₄, CO₃ and Ca(II) removed (%) from NF concentrate at different pH adapted by the membrane electrolysis cell. Standard deviations for removal experiments at pH 9 were 19% removal for Ca(II), 28% recovery for PO₄ and 5.9% removal for CO₃.*

These values are considered to be representative for all experiments. An additional experiment at pH 9 demonstrated that an increase in current to a value of 50 mA (current density 22.7 A/m^2 per electrode compartment) instead of 10 mA (current density of 4.6 A/m^2 per electrode compartment) induced a 3.4x higher CO_3- removal but did not impact PO_4 recovery. This remained equally high at a value of 91% at pH 9 for both currents. Conclusively, the operation at a higher current does not enhance the PO_4-recovery. Besides that, operation at higher currents the pH control was more difficult to control as the pH tended to overshoot the target pH, leading to higher amounts of undesired calcium carbonate incorporation in the product. Another risk of the higher current (50 mA) is the possible formation of undesired amounts of chlorine gas at the anode due to the oxidation of HCl. The average chloride content in the NF concentrate in both compartments was 135 ± 28 mg/L. However, it was found that the [Cl$^-$] in the cathode solution did not change significantly over the entire pH range, while the chloride concentration in the anode solution only started to decrease at pH 10 (3% decrease) and 11 (7% decrease) (both at 50 mA). Conclusively, $Cl_{2(g)}$ formation was not significant at pH values up to 9 and at the lower currents. At the same time, PO_4-recovery under these conditions was high. The $[PO_4]_T$ in the anode compartment stayed constant, whereas $[Ca(II)]_T$ in the anode decreased significantly. This shows that the presence of the cation exchange membrane prevents the migration of PO_4-ions from cathode to anode, while Ca(II) was able to migrate through the CEM. This proof of principle therefore demonstrates that the EPR system has a natural balancing effect and can potentially be used in a continuous mode in an integrated MBR NF/EPR system for simultaneous wastewater treatment and PO_4 recovery.

5.4.4. XRD and ATR-FTIR analysis of precipitate

XRD (Fig. 5.5) and ATR-FTIR (Fig. 5.6) spectra were analysed to obtain more details about the formed precipitates from the EPR and available for PO_4-recovery. Since a molar Ca/P ratio in the precipitate of approximately 1 was reached at lower pH (8.25 and 8.5), especially at these pH values crystalline PO_4-containing minerals with a similar ratio like brushite or monetite were expected to form (Table 5.1, Fig. 5.3).
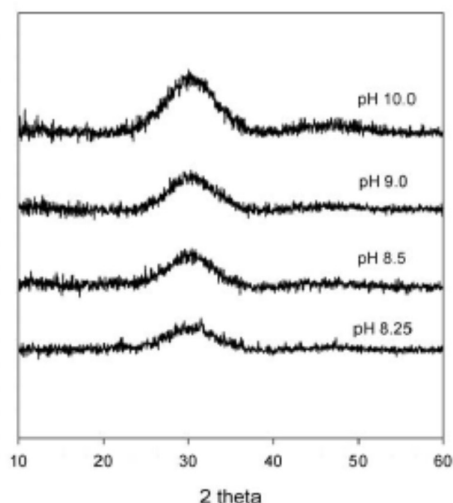
Fig. 5.5. *XRD patterns of the calcium phosphate precipitates obtained from the EPR with real NF concentrate at different pH.*

In the XRD spectra, crystalline phases would show a distinct, sharp peak. In this case such peaks were not observed, suggesting the absence of crystalline calcium phosphate phases like monetite, OH-apatite or brushite (Kim et al. (2004), Zyman et al. (2010)). Instead, a single broad peak with a maximum at angle of 30° was found at all pH levels. A similar XRD peak was found before when using chemical precipitation resulting in ACP formation, occurring at a higher pH of 10.5 (Lu et al. (2010)). This indicated that the precipitates consisted of an amorphous phase. Regarding the composition (Fig. 5.4), the precipitates contain mainly calcium, phosphates and carbonates, therefore ACP ($Ca_3(PO_4)_2 \cdot 3H_2O$) or amorphous calcium carbonate (ACC) formation is most likely. The calculated saturation indices at pH 8, 9 and 10 (HAP: 13.8, 17.2, 19.2; ACP: 3.2, 4.8, 5.5) show that HAP was much more likely to form solids material than ACP. However, formation of ACP is kinetically faster than that of the strongly bound crystalline HAP. These findings were confirmed by ATR-FTIR. Also here no distinct peaks for crystalline phases like brushite were found (Fig. 5.6).
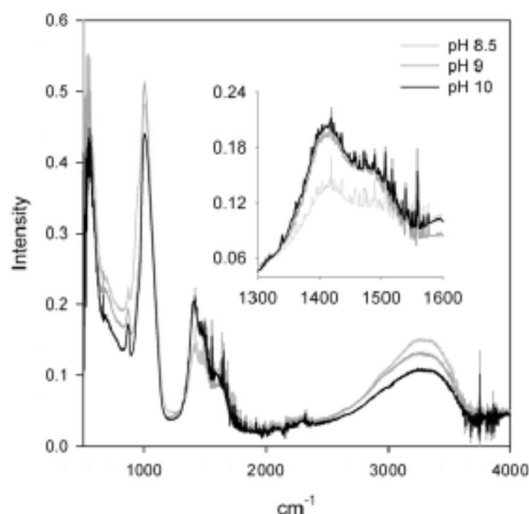
Fig. 5.6. *ATR-FTIR spectra of the precipitates from the EPR formed at pH 8.5, 9 and 10, obtained from real NF concentrate.*

The spectra presented for pH 8.5, 9 and 10 (Fig. 5.6) contained vibration modes of P-O-H groups of the octahedral PO_4^{3-} and Ca-O units at 1020 and 555 cm^{-1}, respectively. The peaks in the regions between 3000-4000 cm^{-1} and 500-600 cm^{-1} represent the H_2O/OH and Ca-O vibrations, respectively. In accordance with the XRD results, ACP shows a typical asymmetric vibration mode of P-O at 950 cm^{-1} in the ATR-FTIR spectra, which is partly overlapped by the peak at 1020 cm^{-1} belonging to the bending vibrations. The vibration bands of water at 1650 cm^{-1} show the inter-structural water phases in ACP, i.e. as in $Ca_3(PO_4)_2.2H_2O$. Both, FTIR and XRD confirm the formation of the commonly metastable phase ACP. ACP usually transforms over time to crystalline minerals like apatite or brushite, depending on the applied pH and concentrations. However, as mentioned, the typical band in the ATR-FTIR for brushite at 959 cm^{-1} was not detected (Kumar et al. (1999)). Regarding calcium carbonates, vibration bands of 1420 and 1467 cm^{-1} in the ATR-FTIR spectra can be attributed to vibration modes of CO_3-ions and also the small peak at 874 cm^{-1} represents Ca-OH vibration, which is typical for ACC. Nevertheless, the XRD spectra showed no evidence of amorphous calcium carbonate (Lafon et al. (2008)), where a small peak residing at 45° 2 angle would have been expected (Fig. 5.5). The carbonate ions were therefore either incorporated into the ACP or precipitated as a separate amorphous calcium carbonate phase (Mayor et al. (1998)). The different intensities in the ATR-FTIR spectra of the carbonate peaks at 1420 and 1467 cm^{-1} indicate qualitative differences, which could be related to the obtained varying CO_3 to PO_4 ratios (Fig. 5.4). Since ATR-FTIR methods measure rather at the surface of the precipitates, it might be possible that vibration

bands of CO_3-ions represent surface precipitated calcium carbonate or CO_3-ions adsorbed to the ACP, which also may have additionally occurred during the drying period of the filtered samples. Sharp peaks of the more crystalline carbonate phases like calcite and aragonite in the ATR-FTIR at 714 cm^{-1} and 750 cm^{-1} were not observed. The absence of these peaks further confirms that the dominant carbonate precipitate was ACC. The calculated supersaturations for pH 8-11 showed also for carbonates that the amorphous phase was slightly less saturated than the crystalline phases. Considerable amounts of CO_3 and Ca(II) were available in the solution to form ACC but the content in the precipitate remained relatively low. Fig. 5.4 shows that the ACC content in the precipitate was always lower than the ACP content. Even at high pH (11) ACC was 2 times lower and at low pH (8.25) it was even 20 times lower. Conclusively, up to pH 9 the precipitate consisted almost exclusively of ACP. Another explanation for the low ACC content is that PO_4 may have acted as an anti-scalant for calcium carbonate. PO_4 is known to prevent calcium carbonate scaling on numerous surfaces e.g. on pipes in sewage systems by replacing the carbonate ions in the precipitate (Plant and House (2002)), which can be explained by a competition between PO_4- and CO_3-ions for calcium. However, the activities of the dominant carbonate species at pH 8-10 are still estimated to be at least 2 times higher than those of the HPO_4^{2-} -ions. Moreover, the kinetic preference of ACP in this research consumes large part of the Ca(II) and in this way lowers the supersaturation for ACC precipitation. Reason for the hindered crystallization of the amorphous phase into the crystalline phase is the presence of species such as magnesium, carbonates and humic acids in the NF concentrate. Those could have promoted the stabilization of ACP (Alvarez et al. (2004), Cao et al. (2007), Ferguson and McCarthy (1971), Suchanek et al. (2004)). Chemical analysis confirmed the presence and removal of total organic carbon, CO_3- and Mg^{2+}-ions from the solution. Molar ratios of magnesium to calcium between 0.37 and 0.76 were found in the NF concentrate. This ratio is sufficient to cause this inhibition and could explain the stabilization of the amorphous phase (Boskey et al. (1974)). Although only limited information on the inhibition mechanism itself is available, the mentioned compounds might have reduced the rate of dissolution and transformation into more crystalline phases. This shows that NF concentrates from a domestic MBR NF process could be a good basis for PO_4 recovery in the amorphous phase instead of a crystalline phase, which may have advantages that will be discussed later on.

5.4.5. SEM analysis

SEM-EDX analysis showed that the main elements found in the precipitate were calcium, phosphorous but also magnesium, oxygen and silica. Also carbon, sodium, chloride and

potassium were detected. Heavy metals were neither detected in this particular concentrate (by ICP) nor in the precipitates by SEM-EDX analysis. Particles smaller than 1 μm were found (Fig. 5.7).
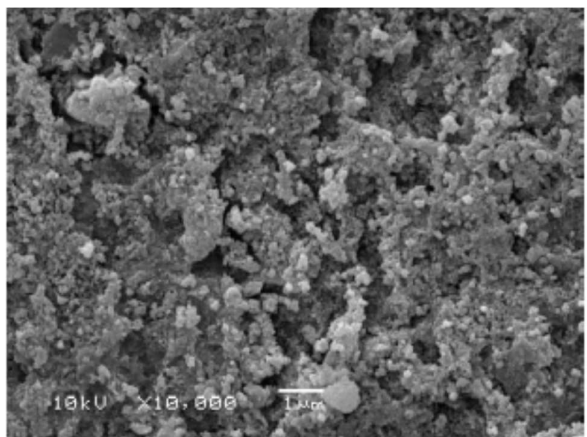
Fig. 5.7. *SEM image of the dried precipitate gained at pH 10 (50 mA) at 10 kV; magnification: 10.000x.*

The small size of the particles could indicate poor settling and consequently poorer separation of the solids from the solution, however settling behaviour still needs to be evaluated.

5.4.6. Future application and economical evaluation

The experiments presented in this research have been performed in a batch mode. Results show the potential of applying EPR in a continuous mode in an integrated MBR NF/EPR system as presented in Fig. 5.8. The nanofiltration concentrate would first pass the anode chamber to strip CO_2 at acidic pH, followed by an alkaline pH cathode chamber where precipitation is induced.

Fig. 5.8. *Schematic overview of a continuous electrochemical PO_4 recovery (EPR) process.*

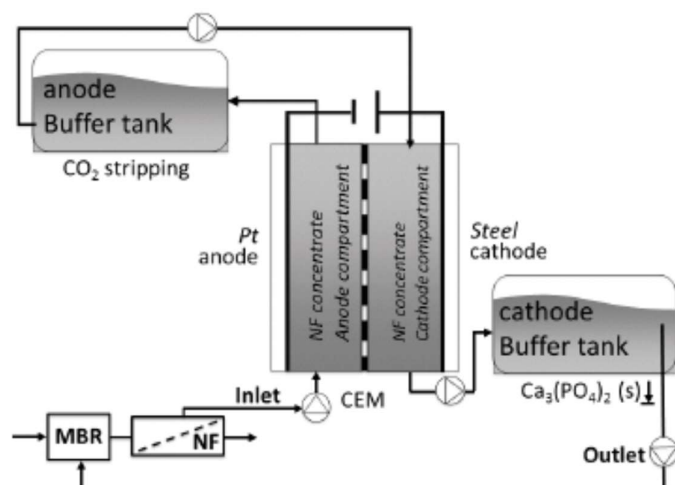A great advantage of the approach proposed here is the continuous formation of hydrogen gas bubbles along the cathode surface due to the electrolysis reaction. In the past, similar devices built for water softening (Gabrielli et al. (2006), Hasson et al. (2010)) had the major concern of formation of calcium phosphate, carbonate or hydroxide precipitation at the cathode surface. Also in our case the high concentrations of carbonates especially at higher pH could theoretically cause scaling. Nevertheless, no deposition on the electrode surface was visually observed. H_2-formation was visually observed during the experiments and suggested to prevent scaling at the cathode surface. Consequently, this will not decrease the membrane or electrode performance. The calculated H_2-gas production (Sleutels et al. (2009)) assuming a maximum coulombic efficiency of 100% was only 4.2 mL per hour during the experiments, which is relatively low compared to e.g. 80 mL per hour in microbial electrolysis cells for hydrogen gas production (Huang et al. (2010)) and safety issues are not expected. At a larger scale, the use of H_2 for energy applications could be considered.

Regarding the settleability of the precipitates, the use of for instance HAP seed crystals may significantly enhance the particle size and therefore the settleability (Angel (1999)). The recovered amorphous ACP could be used as a fast dissolving fertilizer (Jeremiasse et al. (2010)). PO_4 minerals can be found in fast dissolving forms but also in slower dissolving forms (e.g. struvite) (Bolan et al. (1993)). The more crystalline the calcium phosphate phase, the slower the dissolution rate and the slower the release of PO_4^{3-}-ions to the soil, with hydroxyapatite being the most stable and slowest dissolving phase. Solubilities have not been determined in this research but it may be interesting to allocate the dissolution rates of the precipitates in neutral media. A decrease in carbonate precipitation is expected when this system is operated in a continuous mode with simultaneous CO_2 stripping in the anode compartment. The lower pH of the anode can be used to shift the carbonate speciation towards H_2CO_3 (carbonate precipitation) that can be removed from the water. This avoids contamination of the end product with (co-precipitated) carbonates. Finally, depending on the wastewater composition, also heavy metals (e.g. transition metals), magnesium, potassium or humic substances can be present in the nanofiltration concentrate and might also be present in the precipitate to a certain extent. Statements from the Crystallactor® technology that only very low amounts of heavy metals were found still have to be carefully evaluated for this process. Depending on the needed purity of the precipitate, other treatment steps, like adsorption, ion exchange, electrolysis or coagulation and flocculation (Fu and Wang (2011)) might be needed before reuse. Further research in this regard is required. As carbonates are likely to co-

precipitate at high currents and pH values, it depends on the application whether carbonates in the precipitates are acceptable or not and to which extent. In general, PO_4 recovery in the form of ACP from produced NF concentrates (Table 5.2) by using water membrane electrolysis (EPR) is possible, and can be introduced in a continuous MBR/NF process, instead of removing calcium phosphates via the waste sludge (Joss et al. (2011)). Compared to a recovery of 65-70% reached by the Crystallactor® technology (Woods et al. (1999)) this process seems to be more efficient and a high recovery is promoted by the presence of the membrane. Also no transportation, storage and use of chemicals are needed but a fair comparison of a continuously operating system with e.g. the commercially available Crystallactor® technology still has to be done. An energy-cost estimation (Appendix A) for electrolysis was performed assuming the following operational settings for recovery of one ton of phosphorous: a target pH of 8.5, an applied voltage of 3.0 V and a current of 0.01 A. The applied voltage of 3 V was needed to run the electrolysis and was higher than the theoretical value of 1.23 V and also higher than the practical minimum of 1.48 V necessary to overcome the activation energy for water electrolysis. Reason for this high applied voltage was the lower conductivity of the NF concentrate compared to e.g. reverse osmosis concentrates. This also implies that with 3.0 V applied voltage, parts of the energy were lost as heat. An estimation of this heat loss by 1.52 V showed a negligible temperature increase of 0.07 K/m^3 during the electrolysis. With an industrial energy price of 0.10 €/kWh, the costs related to electrolysis would be 303 €/t of recovered P (assuming 100% galvanic efficiency). This is well below the costs for phosphorous of 685 €/t of P (excluding transportation costs) in PO_4-rock, assuming a maximum P-content of 17.5% in the rock (Commodity markets, 2013, Schippers et al. (2001)), and therefore PO_4 recovered by this electrochemical technology may provide an attractive possibility to replace part of the scarce PO_4-rock. Also from a wastewater treatment perspective the operational costs related to energy consumption are relatively low, i.e. only 0.004 €/m^3 of treated wastewater, while significant costs can be saved on biological or chemical phosphorus removal. Table 9.3 shows the energy estimations based on the experimentally gained data for the electrochemical process.

Table 5.3 *Calculated energy (kWh) per kg phosphorous and per cubic meter of concentrate treated based on the experimental P-recoveries at different pH and applied currents.*

pH	8.25	8.5	9	10	11
mA	10	10	10	50	50

| kWh.kg/P | 3.0 | 2.4 | 2.4 | 5.0 | 12.6 |
| kWh/m³ | 0.054 | 0.049 | 0.041 | 0.195 | 0.195 |

These results show that the energy consumption is directly related to the electricity used for the electrolysis. Increased current led to increased energy which also increased the P-recovery. Additionally, at higher currents more energy is needed per kg P as at the same time energy was withdrawn for carbonate co-precipitation. An additional advantage of this system is that no storage of chemicals is needed. However, the platinum electrode used in this system is expensive, so a cheaper option e.g. nickel electrodes could decrease these costs but will also decrease the robustness and efficiency of the process. In the continuous system also costs for CO_2 stripping and transportation costs of products should be taken into account.

5.5. Conclusions

Amorphous calcium phosphate (ACP) can be recovered to a very high degree (up to 90%) from real domestic nanofiltration concentrates with an integrated MBR NF/EPR concept. - The NF concentrate can be re-introduced into the MBR at much lower [PO_4] and [Ca(II)], reducing scaling problems in the MBR system. Nevertheless, sufficient calcium should be available to aid the desired bio-flocculation in the MBR. High PO_4-recovery can be obtained at pH = 9, as precipitation of calcium phosphates or carbonates on electrodes or membrane surface is not observed. EPR is shown here as an attractive technology as no usage, storage and transportation of chemicals is needed.

Appendix A: Energy and cost calculation The energy calculation in this manuscript is based on the actual moles of P needed for the calcium phosphate formation. Assuming 1,000,000 g of P: 32 g mol^{-1} gives 31,250 mol P. The PO_4-speciation can be assumed according to the following: The sum (Total PO_4) of the two main present species at pH 7.8 ($H_2PO_4^-$ and HPO_4^{2-}) is given as:

Total PO_4 = TOTPO4 = [HPO_4^{2-}] + [$H_2PO_4^-$]

These two species have an equilibrium at a pK$_a$ of 7.21, which gives their relationship as:

$[HPO_4^{2-}][H^+]/[H_2PO_4^-] = 10^{-7.21}$.

After rearrangement and substitution of the two equations, the moles of $[H_2PO_4^-]$ and $[HPO_4^{2-}]$ at pH 7.8 can be calculated according to:

$[HPO_4^{2-}] = ([TOTPO_4] * [10^{-7.21}]) / ([10^{-pH}] + [10^{-7.21}])$

$[H_2PO_4^-] = TOTPO_4 - [HPO_4^{2-}]$

$[HPO_4^{2-}] = (31,250 \text{ mol} * 10^{-7.21}) / (10^{-7.8}+10^{-7.21}) = 24,860 \text{ mol}$

$[H_2PO_4^-] = 31,250 - 24,860 = 6,390 \text{ mol}$

Regarding the following reactions that will generate amorphous calcium PO4:

$3Ca^{2+} + 2[H_2PO_4^-] + nH_2O$

$Ca_3(PO_4)_2 * nH_2O + 4H+ \; 3Ca^{2+} + 2[HPO_4^{2-}] + nH_2O \; Ca_3(PO_4)_2 * nH_2O + 2H+$

From these and the moles of the two species above, the amount of OH⁻ needed to produce amorphous calcium phosphate precipitation can be calculated: In total 37,638 M (24,860 M + 2 * 6,390 M) of H^+ -ions are released when 1 ton P is precipitated assuming that all P is precipitated. To keep the pH at the cathode equal, a corresponding amount of OH⁻ is needed to titrate this amount of H^+ -ions. One has to produce 37,640 M of OH⁻. Electric charge necessary to produce OH⁻ needed: 37,640 mol * 96,485 C mol^{-1} = 3.63 x 109 C Energy per ton of P:

3.63 x 109 C * 3V (applied voltage) = 1.0895x 1010 J ton P^{-1} Power per ton of P in 15 minutes: 1.0895x 1010 J ton P^{-1}:

900s = 1.21 x 107 W : 1000 = 12105 kW * 0.25 h = 3026.3 kWh

Costs per ton of P:

3026.3 kWh * 0.10 € kWh^{-1} = 303 € ton P^{-1}

References

Alvarez R., Evans L.A., Milham P.J., Wilson M.A., Geoderma, 118 (2004) 245-260.

Angel R., Environmental Technology, 20 (1999) 709-720.

Bolan N.S., Hedley M.J., Loganathan P., Fertilizer Research, 35 (1993) 13-24.

Boskey A.L., Posner A.S., Materials Research Bulletin, Magnesium Stabilization of Amorphous Calcium PO4: A Kinetic Study, 9 (1974) 907-916.

Cao X., Harris W., Environmental Science & Technology, 42 (2007) 436-442.

Commodity Markets, in: TheWorldBankGroup (Ed.), Washington, DC, 2013.

Dorozhkin S., Calcium orthoPO4s, J Mater Sci, 42 (2007) 1061-1095.

Doyle J.D., Parsons S.A., Water Research, 36 (2002) 3925-3940.

Eggers E., A.H. Dirkzwager A.H., Van den Honing H., Water Science and Technology, 23 (1991) 819-824.

Ferguson J.F., McCarty P.L., Environmental Science and Technology, 5 (1971) 534-540.

Fernandez E., Gil F.J., Ginebra M.P., Driessens F.C.M., Planell J.A., Best S.M., J.Materials Sci.: Materials in Medicine, 10 (1999) 177- 183.

Fu F., Wang Q., Removal of heavy metal ions from wastewaters: A review, Journal of Environmental Management, 92 (2011) 407-418.

Gabrielli C, Maurin G., Francy-Chausson H., Thery P., Tran T.T.M., Tlili M., Desalination, 201 (2006) 150-163.

Hasson D., Sidorenko G., Semiat R., Desalination, 263 (2010) 285-289.

Huang H, Xiao X., Yang L., Yan B., Water Science and Technology, 61 (2010) 2741-2748.

Jacob M., Guigui C., Cabassud C., Darras H., Lavison G., Moulin L., Desalination, 250 (2010) 833-839.

Jeremiasse A.W., Hamelers H.V.M., Saakes M., Buisman C.J.N., Int. J. Hydrogen En., 35 (2010) 12716-12723.

Joko I., Water Science and Technology, 17 (1984) 121–132.

Joss A., Baenninger C., Foa P., Koepke S., Krauss M., McArdell C.S., Rottermann K., Wei Y., Zapata A.,. Siegrist H., Water Research, 45 (2011) 6141-6151.

Kim H.-G., H.-N. Jang, H.-M. Kim, D.-S. Lee, T.-H. Chung, Desalination, 250 (2010) 629-633.

Kim S., Ryu H.-S., Shin H., Jung H.S., Hong K.S., Chemistry Letters, 33 (2004) 1292-1293.

Kumar M., Xie J., Chittur K., Riley C., Biomaterials, 20 (1999) 1389-1399.

Lafon J.P., Champion E., Bernache-Assollant D., J. European Ceramic Society, 28 (2008) 139-147.

Lu N.C., Liu J.C., *Separation and Purification Technology*, **2010**, 74, 329- 335.

Mayor B., J. Arias, S. Chiussi, F. Garcia, J. Pou, B. León Fong, M. Pérez-Amor, Calcium PO4 coatings grown at different substrate temperatures by pulsed ArF-laser deposition, *Thin Solid Films*, 1998, 317, 363-366.

Nederlof M.M., Van Paassen M.A.M., Jong R., *Desalination*, **2005**, 178, 303-312.

Noronha M., Britz T., Mavrov V., Janke H.D., Chmiel H., *Desalination*, **2002**, 143, 183-196.

Plant L.J., House W.A., *Colloids and Surfaces A: Physicochem. and Eng. Aspects*, **2002**, 203, 143-153.

Rockstrom J., Steffen W., Noone K., Persson A., Chapin F.S., Lambin E.F., Lenton T.M., M. Scheffer, Folke C., Schellnhuber H.J., Nykvist B., de Wit C.A., Hughes T., Van der Leeuw S., Rodhe H., Sorlin S., Snyder P.K., Costanza R., Svedin U., Falkenmark M., Karlberg L., Corell R.W., Fabry V.J., Hansen J., Walker B., D. Liverman D., Richardson K., Crutzen P., Foley J.A., *Nature*, **2009**, 461, 472-475.

Roeleveld P., Loeffen P., Temmink H., Klapwijk P., *Water Science and Technology*, **2004**, 49, 191-199.

Sartorius C., van Horn J, Tettenborn F, Phosphorous Recovery from Wastewater – State-ofthe-Art and Future Potential, in: *Nutrient recovery and management 2011 Inside and Outside the Fence, International Water Association (IWA), Water Environment Federation (WEF)*, **2011**, Miami, Floria, USA, 19.

Schipper W.J., Klapwijk A., Potjer B., Rulkens W.H., Temmink B.G., Kiestra F.D.G, Lijmbach A.C.M., *Environmental Technology*, **2001**, 22, 1337-1345.

Sleutels T.H.J.A., Hamelers H.V.M., Rozendal R.A., Buisman C.J.N., Int. J. Hydrogen En., 34 (2009) 3612-3620.

Sperlich A., Warschke D., Wegmann C., Ernst M., Jekel M., Water Sci. and Tech., 61 (2010) 301-306.

Suchanek W.L., Byrappa K., Shuk P., Riman R.E., Janas V.F., Ten Huisen K.S., J. Sol. State Chem., 177 (2004) 793-799.

Tchobanoglous G., Wastewater Engineering, Treatment and Reuse, 4th ed., McGraw-Hill, New York, 2004.

Tung M.S., F.C. Eichmiller F.C., Compendium of Continuing Education in Dentistry, 25 (2004) 9-13.

Van den Broeck R., Van Dierdonck J., Nijskens P., Dotremont C., Krzeminski J., van der Graaf J.H.J.M., Van Lier J.B., Van Impe J.F.M, Smets I.Y., J. of Membrane Sci., 401–402 (2012) 48-55.

Wang C.C., X.D. Hao X.D., Guo G.S., Van Loosdrecht M.C.M., Chemical Eng. J., 159 (2010) 280- 283.

Woods N.C., Sock S.M., Daigger G.T., Phosphorus Recovery Technology Modeling and Feasibility Evaluation for Municipal Wastewater Treatment Plants, Environmental Technology, 20 (1999) 663-679. Chapter 5 125 Chapter 5

Zyman Z.Z., Rokhmistrov D.V., Glushko V.I., Structural and compositional features of amorphous calcium PO4 at the early stage of precipitation, Journal of Materials Science: Materials in Medicine, 21 (2010) 123-130.

Summary.

In this thesis, the formation of ferrihydrite by the *iron* electrocoagulation (Fe-EC) technology was investigated, focusing on the impact of process conditions such as pH and oxygenation (Chapter 2), as well as the composition of the electrolyte (Chapter 3). The objective was to enhance the removal of contaminants by generating a rust phase (ferrihydrite) with maximum adsorption capacity. Moreover, the influence of local high pH regions on the cathode surface, due to the evolution of H_2 and OH^- ions, was further examined through recrystallization studies under highly alkaline conditions and in the presence of Fe(II) (Chapter 4).

Additionally, a membrane electrolysis cell was utilized for the *electrochemical recovery* of PO_4 from the concentrated effluent stream obtained from a combination of a membrane bioreactor and nanofiltration process (Chapter 5). The purpose of this treatment was to reclaim the valuable PO_4 as calcium phosphate product, while simultaneously facilitating the reuse of the concentrated stream in the preceding membrane bioreactor process.

Chapter 2 demonstrates, for the first time, that ferrihydrite with high sorption capacity is formed during the oxygenated Fe-EC process at low current density (6.25-25 A/m^2). However, ferrihydrite is only stable for a short period of time (30-60 min.) and quickly transforms into crystalline forms of lepidocrocite and goethite during ongoing Fe-EC operations (120 min.). This transformation leads to a lower sorption capacity, so attempts were made to study the reason for this transformation and find ways to minimize it.

The transformation of ferrihydrite occurs particularly when the concentration of Fe(II) is elevated, and when the oxygenation of the electrolyte (controlled by stirring) is too low to oxidize all the electrochemically generated Fe(II) (by electrolytic oxidation of Fe(0)). The unoxidized fraction of Fe(II) ions acts as a catalyst, facilitating the transformation of ferrihydrite through electron transfer between Fe(II) and ferrihydrite, and driving reductively catalyzed dissolution of ferrihydrite.

The transformation to lepidocrocite and/or goethite occurs at much faster rates compared to the usual aging period of ferrihydrite in the absence of Fe(II) (>1 year). This has significant implications for Fe-EC systems when considering the removal of contaminants such as heavy metals, which require reaction times of a few hours (1-10h).

Efforts to maintain a low concentration of total Fe(II) ($[Fe(II)]_T$) were made by increasing the supply of O_2 to the Fe-EC cell through fast stirring of the electrolyte or by adding highly oxidative H_2O_2 to the electrolyte. These methods successfully increased the productivity of ferrihydrite, resulting in the formation of ferrihydrite exclusively under H_2O_2 conditions and to a lesser extent under saturated oxygen conditions (established by vigorous mixing of the electrolyte). The impact of increased ferrihydrite production was evident in a 40% higher removal of PO4 with respect to the rust phase dominated by lepidocrocite and goethite.

It is common for both industrial and domestic wastewaters to contain anions such as Cl-, SO_4-, CO_3-, and PO_4-. While these anions contribute to the electrical conductivity of the electrolyte and help reduce energy losses in Fe-EC cells (including mass, ohmic, and activation losses), they are also known to impact the rate of ferrous oxidation and the speciation of iron oxyhydroxides formed during Fe-EC operations. **In Chapter 3** of the study, the goal was to investigate the formation of ferrihydrite in relation to the electrolytes containing $[CO_3]+[SO_4]$ and $[PO_4]+[Cl-]$. Based on existing knowledge, Cl- and SO_4- ions are strongly linked to the formation of lepidocrocite and goethite, while PO_4- and, to a lesser extent, CO_3- ions are associated with ferrihydrite formation. Both anions have been found to inhibit Fe(III) polymerization by forming aqueous complexes with Fe(III), which generally favors the production of ferrihydrite over lepidocrocite/goethite. Through Fe-EC tests conducted in the presence of these anions, we demonstrated that increasing the $[CO_3]/[SO_4]$ ratio resulted in greater ferrihydrite formation. This effect was attributed to the adsorption of CO_3- and PO_4- ions onto the formed ferrihydrite, rather than aqueous complexation. Additionally, the adsorption of these anions onto the surface of ferrihydrite competitively inhibited the adsorption of Fe(II) ions, thus reducing the reductively catalyzed transformation of ferrihydrite through electron transfer between Fe(II) and ferrihydrite. PO_4- ions were found to be particularly effective in causing this competition due to their high affinity for adsorption onto ferrihydrite surfaces. Notably, the production of ferrihydrite was only observed during the 240-minute Fe-EC run at high $[CO_3]_T$ levels of 150 and 250 mM. Understanding the impact of these common anions on iron oxyhydroxides allows for the development of a more controlled Fe-EC process that favors the production of ferrihydrite.

Lepidocrocite, which has an intermediate adsorption capacity between ferrihydrite and goethite, is prone to transforming into goethite. This transformation is often accompanied by a decrease in its adsorption capacity to remove contaminants from wastewater. Lepidocrocite is less susceptible to catalytic transformation by Fe(II) due to its higher thermodynamic stability compared to ferrihydrite. However, in the design of Fe-EC with multiple stacked anodes and

cathodes perpendicular to each other, the local pH during Fe-EC operation can become very high (pOH = 0-1) due to the formation of OH- ions locally. Previous studies have shown that lepidocrocite transformation under such alkaline conditions (1.0 M NaOH) takes a few days. However, the presence of Fe(II) near the electrode surfaces resulting from incomplete oxidation of Fe(II) during the Fe-EC process has not been previously studied. In **Chapter 4**, recrystallization tests conducted under alkaline conditions (1M) and in the presence of Fe(II) revealed that the transformation to goethite ($[Fe(II)]_T$:$[Fe(III)]_T$ = 1.0:1.0-10) was accelerated by a factor of 52-250x. This effect can have significant implications in the vicinity of the cathode surface, where the local presence of Fe(II) may cause lepidocrocite to convert rapidly into goethite.

Electrochemical phosphate (PO₄) recovery. In **Chapter 5**, we applied electrochemical treatment to remove PO_4 from the concentrated solution of a combined MBR and NF treatment of domestic wastewater. This was done without using expensive and potentially contaminating the MBR/NF concentrate. This chapter demonstrates the application of a membrane electrolysis cell for the recovery of calcium phosphate from this concentrated stream. The major advantage is that no chemicals are used, and therefore no salts are added to induce precipitation. This opens up the opportunity to recirculate the concentrated stream into the preceding MBR, effectively eliminating it. The recovery of calcium PO_4 was achieved by raising the pH in the cathode compartment through water electrolysis. From the precipitation tests, it was observed that amorphous calcium PO_4 was precipitated. This is a fertilizer with high dissolution rates and is highly preferred for soil fertilization. However, the co-precipitation of amorphous calcium carbonate at higher pH levels (25% at pH 10 and 41% at pH 11) is undesirable. This is because it decreases the ACP content and potentially reduces the dissolution properties of ACP. Therefore, the optimum conditions to minimize ACC co-precipitation were limited to pH = 9. Even at this pH, a satisfactory recovery of 91% was still achieved.

Samenvatting

Deze dissertatie omvat de studie naar de vorming van ferrihydriet met de ijzer elektro-coagulatie (Fe-EC) technologie, met de focus op de rol van procescondities zoals pH en zuurstoftoevoer naar de Fe-EC (Hoofdstuk 2) alsmede de compositie van het elektrolyt (Hoofdstuk 3). Het doel was om de verwijdering van contaminanten te verbeteren door de productie van ferrihydriet met een hoge adsorptie capaciteit te bevorderen met het Fe-EC proces. De invloed van lokale hoge pH aan het kathodeoppervlak, dat veroorzaakt wordt door evolutie van H_2 en OH^- ionen, was verder bestudeerd door de rekristallisatie te bestuderen onder hoog basische condities en in het bijzijn van Fe(II) (Hoofdstuk 4).

Verder werd er een membraanelektrolyse cel toegepast voor het elektrochemisch terugwinnen van fosfaat uit geconcentreerde afvalstroom afkomstig uit een gecombineerde behandeling met een membraanbioreactor en nanofiltratie (Hoofdstuk 5). Het doel van deze behandeling is om waardevolle PO_4 terug te claimen in de vorm van een calcium fosfaat product en tegelijkertijd het faciliteren van het hergebruik van het geconcentreerde waterstoom in de voorgaande membraanbioreactor proces.

Hoofdstuk 2 demonstreert voor het eerst dat ferrihydriet met een hoge sorptie capaciteit vormt tijdens de zuurstof verrijkte Fe-EC proces onder lage stroomdichtheid (6.25-25 A/m^2). Echter, ferrihydriet is maar stabiel voor een korte tijdsduur (30-60 min.) en zet snel om naar kristallijne lepidocrociet en goethiet vormen tijdens de Fe-EC operatieduur (120 min.). Dit soort snelle omzettingen leiden tot het verminderen van de sorptiecapaciteit, en daardoor zijn verdere studies verricht om de reden voor de omzetting te achterhalen en manieren te vinden om de omzetting te verminderen of zelfs volledig tegen te gaan.

De omzetting van ferrihydriet vindt vooral plaats wanneer de Fe(II) concentratie omhoog gaat, en wanneer de oxygenatie van het elektrolyt (d.m.v elektrolyt roeren) te laag is om alle elektrochemische gevormde Fe(II) (via elektrolytische oxidatie van Fe(0)) te oxideren. De niet-geoxideerde fractie van de Fe(II) gedraagt zich as een katalyst, dat de omzetting faciliteert door elektronenoverdracht tussen Fe(II) en ferrihydriet en het reductief oplossen van de ferrihydriet.

Deze omzetting vindt veel sneller plaats in het bijzijn van Fe(II) dan de algemene langzame veroudering van ferrihydriet (>1 jaar). Dit heeft grote gevolgen voor de toepassing

van Fe-EC systemen gezien de verwijdering van contaminanten zoals zware metalen reactietijd hebben van een paar uren (1-10u).

Inspanningen om een lage Fe(II) concentraties te waarborgen door het zuurstoftoevoer naar de Fe-EC cel met snel roeren of door sterk oxiderend H_2O_2 aan het elektrolyt toe te voegen heeft geleid tot een verhoogde productiviteit van ferrihydriet, met als resultaat ferrihydriet exclusief geproduceerd werd in elektrolyt H_2O_2 en in mindere mate onder volledig verzadigde zuurstofcondities (bereikt door elektrolyt sterk te roeren). De positieve uitkomst van de verhoogde productie van ferrihydriet op contaminantverwijdering was bewezen met een 40% hogere verwijdering van PO_4 met ferrihydriet-rijke roest in vergelijking tot de roest fase gedomineerd door lepidocrociet en goethiet.

Het is algemeen bekend dat industrieel en huishoudelijk afvalwaterstromen veel voorkomende anionen bevatten zoals Cl-, SO_4-, CO_3-en PO_4-ionen. Deze anionen zorgen voor de geleidbaarheid van het afvalstromen, en daarbij de energieverliezen van de Fe-EC cellen verminderen (massa-, ohmse- en activatieverliezen). Deze anionen hebben daarentegen een grote invloed op de oxidatiesnelheid van Fe(II) en op de speciatie van de gevormde ijzer oxyhydroxiden tijdens Fe-EC procesvoering. **Hoofdstuk 3** van deze dissertatie heeft als doel om de vorming van ferrihydriet te bestuderen in relatie tot de elektrolyt compositie met $[CO_3]+[SO_4]$ en $[PO_4]+[Cl-]$. Gebaseerd op huidige kennis zijn Cl^- - en SO_4- ionen sterk gelinkt aan de vorming van lepidocrociet en goethiet, terwijl PO_4- en in mindere mate CO_3- ionen geassocieerd zijn met de vorming van ferrihydriet. De huidige mechanisme beschrijft dat PO_4- en in mindere mate CO_3-ionen de polymerisatie van Fe(III) afremmen door vorming van aquatische complexatie met Fe(III)-ionen, wat in het algemeen de vorming van ferrihydriet begunstigd ten opzicht van de lepidocrociet/goethiet. Met Fe-EC testen uitgevoerd in elektrolyt met deze anionen is aangetoond dat het verhogen van de $[CO_3]/[SO_4]$ ratio in het elektrolyt resulteert in hogere productie van ferrihydriet. Anders dat de eerder mechanisme waar aquatische complexatie een belangrijk rol speelt in de vorming van ferrihydrite is dit effect toegeschreven aan de adsorptie van CO_3- en PO_4- ionen aan de gevormde ferrihydriet en het daarbij verlagen van de concurrerende adsorptie van Fe(II)-ionen, waardoor de reductief gekatalyseerde omzetting van ferrihydriet door elektronenoverdracht tussen Fe(II) en ferrihydriet sterk wordt tegengegaan. PO_4- ionen zijn zelfs nog effectiever in het tegengaan van Fe(II) adsorptie, wat vooral te wijten is aan de hoge affiniteit van PO_4-ion adsorptie aan ferrihydriet oppervlak. Opmerkelijk is dat de productie van ferrihydriet voor de 240-minuut durende Fe-EC proces alleen mogelijk is in een elektrolyt met een hoge $[CO_3]_T$ van 150 en 250 mM. Het begrijpen van de invloed van deze veelvoorkomende anionen op de ijzer

oxyhydroxide vorming helpt hierbij met de ontwikkelen van een beter controleerbare Fe-EC proces dat de productie van ferrihydriet bevordert.

Lepidocrociet, dat een adsorptiecapaciteit heeft dat ligt tussen ferrihydriet en goethiet, is vatbaar voor omzetting naar goethiet. Deze omzetting gaat gepaard met een verlaagde adsorptiecapaciteit voor de verwijdering van contaminanten uit afvalwaterstromen. Ten opzicht van ferrihydrite is lepidocrociet minder vatbaar voor een Fe(II)-gedreven omzetting omdat het thermodynamische stabieler is dan ferrihydriet. Echter, in veel toegepast designs van Fe-EC cellen waar meerdere anode en kathode loodrecht naast elkaar worden geplaats, komt het voor dat de pH dicht tegen de kathode tijdens het bedrijfsvoering van de Fe-EC proces heel hoog kan zijn (pOH = 0-1) door de lokaal vorming van OH- ionen aan de kathodeoppervlak. Eerdere studies hebben aangetoond dat de omzetting van lepidocrociet onder basische condities (1.0 M NaOH) een paar dagen kan duurt. Echter is het niet eerder bestudeerd of het bijzijn van Fe(II) in deze hoog basische regio van het kathodeoppervlak, bijv. als resultaat van incompleet oxidatie van Fe(II) tijdens de Fe-EC procesvoering, de omkristallisatie van lepidocrociet versnelt. In **Hoofdstuk 4,** waar rekristallisatie testen zijn gedaan in basische condities (1M) en in het bijzijn van Fe(II), is aangetoond dat omzetting van lepidocrociet naar goethiet ($[Fe(II)]_T$:$[Fe(III)]_T$ = 1.0:1.0-10) versneld wordt met een factor 52-250x. Dit effect heeft grote implicaties voor de productie van lepidocrociet met het Fe-EC proces, gezien de bijzijn van Fe(II) in de lokale basische omgeving van kathode de omzetting van lepidocrociet naar goethiet flink kan versnellen en daardoor een sterke invloed heeft op de verwijdering van contaminanten met de Fe-EC technologie.

Elektrochemische terugwinning van fosfaat. In **hoofdstuk 5** is een elektrochemische behandeling toegepast voor het terugwinnen van fosfaat uit een geconcentreerde effluent afkomstig uit een gecombineerde behandeling van huishoudelijk afvalwater met membraan bioreactor (MBR) en nano-filtratie (NF). De belangrijkste voordeel van deze toepassing is dat er geen chemicaliën gebruikt wordt en daardoor geen zouten opgelost om de neerslag van fosfaat te forceren. Dit opent weer nieuwe mogelijkheden om de geconcentreerde stroom te elimineren door deze stroom te recirculeren in het voorgaande MBR. Het terugwinnen van fosfaat als calciumfosfaat was bereikt door de pH in de kathodecompartiment te verhogen door middel van waterelektrolyse. Uit de gevormde neerslag is gebleken de de amorfe calcium fosfaat (ACP) voornamelijk vormt. Deze vorm van calcium fosfaat staat bekends als een snel oplosbare kunstmest en is daardoor een gewilde kunstmesttype voor bodembevruchting. Echter, de co-precipitatie van de amorfe calcium carbonaat (ACC) bij hoge basische condities

(25% bij pH 10 en 41% bij pH 11) is niet gewenst gezien het de ACP gehalte verlaagd en de oploseigenschappen potentieel kan verminderen. De meest optimum condities voor het verminderen van de ACC co-precipitatie is bereikt bij een pH van 9, waar het nog steeds mogelijk was om een voldoende hoeveelheid aan fosfaat, nl. 91%, terug te winnen uit de geconcentreerde afvalstroom.

Curriculum vitae

Kamuran Yaşadı was born on 30th October 1978 in Eindhoven. After MAVO (St. Aloysius MAVO), he finished his education in Middelbaar Laboratorium Onderwijs (at Technisch Lycem Eindhoven) and graduated as a laboratory assistant. He then studied Chemistry at Fontys Hogescholen, where he received his B.Sc in Organic Chemistry with two internships at Philips NV and at the Technical University of Eindhoven. He got his M.Sc in (bio)geochemistry at Utrecht University, graduating on the topic of "the effect of aluminium on the biogeochemical cycling of biogenic silica". At the Technical University of Delft, he was accepted as a PhD-graduate on the topic of the "electrochemically induced precipitation for contaminant removal from wastewater streams". This was a project in collaboration with Wetsus (Leeuwarden). After this period, he worked as a Researcher and a part-time teacher for 2.5 years at Wageningen University and Research (Physical Chemistry and Soft Matter), followed by 5 years occupation as an Innovation Scientist at Energy research Centre of the Netherlands (now part of TNO) in Petten. There, he worked in various research and development projects related to energy transition, conducting work on environmental assessment of waste materials and electrochemical water treatment technology of wastewater streams. Later, in the Sustainable Process Technology group, he was responsible in conducting research in energy storage solutions such as large scale application of redox flow batteries and electrolysers. Its great interest in redox flow batteries brought him to Elestor BV (in Arnhem), where he is currently working as a Senior Scientist in the research development team. His major activities and responsibilities are to provide scientific knowledge on the application of hydrogen-X (X – metal) flow batteries in long duration (electric) energy storage.

Acknowledgement

After years of having doubts of finishing this thesis, the last opportunity came to me thanks to my promotors and Graduation school to find last motivation to finish this PhD journey. An important driver to finish this thesis is just the beauty of the iron oxyhydroxide chemistry, in all its complexities. The iron chemistry is one of the most studied materials, and despite the years of research in iron chemistry, and +10000 publication on this matter, there are still new knowledge revealedon the unique properties iron oxyhydroxides. It is just an amazing that this type of material plays such an ubiquitous role in Worlds soil processes and in water treatments. And, I'm very glad that I could contribute in understanding of iron oxyhydroxide chemistry.

I would like to thank Prof. dr. Ekkes Brück to be my promotor. Although we've collaborated only for a very short moment, I really appreciate your kindness, experience, guidance and willingness to be my promotor and help me in finishing this thesis. I wish we had contacted and collaborated much earlier, and had more time to collaborate on the work on iron oxyhydroxide formation mechanism, especially when considering your experienced scientific knowledge being a great contributor to iron oxyhydroxide formation mechanism.

I would like to thank Prof. dr. Geert-Jan Witkamp, who despite his illness, supported me in finishing this thesis from the start of this PhD journey. You are a great scientist, and really liked the time we were discussing various ideas for water treatment. It was a very inspiring time for me. And, I'm really thankful that every time we'd pick up to finish this thesis, there was always the enthusiasm from your side to support me in finishing this thesis. This was always a great boost for me to catch up the PhD trajectory. I am very thankful for helping me in reaching this goal.

All the past years, I've been working at different place with colleagues and friends aware of my journey to finish this thesis. Starting in 2007-2011, I had a great time then at Wetsus when I was part of the Wetsus institute growing towards a renowned research institution in the field of water technology. In those periods, I've met many lovely people who liked to work with and I want to thank Tom, Luciaan, Martijn, Lucia, David, Ingo, Urania, Petra, Philipp, Adriaan, Taina, Alcina, Bruno and Luewton. Christina, it was a nice journey that we both from different disciplines could combine our knowledge to publish the paper on phosphate recovery. At the start of this project, I was guided by two supervisors, who had put a lot of effort helping me starting this PhD journey. Thank you Daniela (Trambitas) and Sybrand (Metz) for this support. Initially, my co-promotor was Dr. Albert Janssen (Shell/WUR), who supported me in this PhD trajectory. I also want to thank Albert for his excellent eye for scientific discussions. Of course my two paranymphs and my friends, Marco de Graaff and Elsemiek Croese, who without any doubt said immediately yes when I'd asked them to be my paranymphs. I am very thankful for that. I love you guys!

I've worked two years in the Wageningen University of Research in the group of Physical Chemistry and Colloid Science (now Physical Chemistry and Soft matter) as a researcher in collaboration with Prof. Emeritus Herman van Leeuwen. It was great and pleasant time to work in this very dynamic group. And Herman, I am very amazed of your dedication to scientific research, and an excellent approach to execute scientific research. I'm very honored to have work with you Herman! Thanks for the very educative and inspiring time.

After my journey at WUR, I've worked at ECN (which later became part of TNO), where I've spend my time for about 5 years in the beautiful place called Petten, where I could go to work

by walking on the beach. There were many inspiring people that I've worked with, and learned a lot in those 5 years. I want to thank Frans, Sjaak, Ilona, Danielle, Lorenzo, Tatjana, Andre, Joris for the very nice years.

Currently I'm working in a very international team of Elestor (Arnhem), where we develop redox flow batteries for energy storage solution. I like to thank all the Elestorians, who provided me the warm environment and supported me through the past years. All the best for all Elestorians.

Last, this thesis would have never been finished without the support and help of my beloved Małgorzata. You're just a fantastic person, and I just can't describe how happy I'm that you're in my life. And of course, my precious daughter Mira is the best gift of my life and brought me more joy and happiness than I've ever had imagined. At last, I want to thank my precious parents (Mürselin and Ilyas) and my brother Yasin for the tremendous support, who noticed the big struggles I'd had over the years. They never doubted in me, and I'm very grateful that they are in my life.